



Mechanical Behavior of Absorbable Iron Foams with Hollow Struts for Bone Scaffolding Applications

Thèse

Seyed Mohammad Reza Rafieipour Alavi

Doctorat en génie des matériaux et de la métallurgie
Philosophiæ doctor (Ph. D.)

Québec, Canada

**Mechanical Behavior of Absorbable Iron Foams
with Hollow Struts for Bone Scaffolding
Applications**

Thèse

Philosophiæ Doctor (Ph. D.)

Sous la direction de :

Hendra Hermawan, directeur de recherche
Hamid Akbarzadeh, codirecteur de recherche

Reza Alavi 2021

Résumé

Jusqu'à il y a quelques années, chaque année, aux États-Unis, plus de 500 000 personnes devaient réparer leurs défauts osseux [1]. Il a été prédit que le besoin de telles réparations doublerait aux États-Unis et dans le monde d'ici 2020 [1]. Les techniques de greffe osseuse sont couramment utilisées pour guérir de gros défauts osseux. Cependant, la greffe osseuse présente certains inconvénients tels que l'infection, la douleur, la morbidité et le manque de site donneur. L'échafaudage osseux est considéré comme une approche alternative pour guérir les défauts osseux sans complications liées à la greffe. Les échafaudages osseux sont considérés comme des implants temporaires, car après la formation de nouveaux tissus, leur présence n'est plus nécessaire.

Des métaux poreux biodégradables (résorbables) ont été développés et étudiés en tant qu'échafaudages osseux temporaires. Ces structures poreuses fournissent un support mécanique et un espace biologique pour la régénération tissulaire. Ces implants se corrodent pendant le processus de régénération tissulaire et, idéalement, ils devraient disparaître une fois le processus de guérison terminé. Ainsi, aucune chirurgie secondaire pour les retirer ne serait nécessaire.

Une tâche cruciale des échafaudages osseux résorbables est de fournir un support mécanique pour la formation de nouveaux tissus. Les échafaudages doivent conserver leur intégrité mécanique sans défaillance en raison des charges mécaniques appliquées à partir du milieu environnant. En revanche, en tant qu'implants orthopédiques, leur rigidité ne doit pas être supérieure à celle du tissu osseux environnant en raison du risque de *stress shielding*. Ainsi, la compréhension des facteurs influençant la réponse mécanique de l'échafaudage osseux lors de la dégradation et la prédiction de leurs propriétés mécaniques sont cruciales. La conception et la fabrication d'échafaudages résorbables sont un sujet d'intérêt pour les chercheurs.

Des analyses détaillées qui expliquent les propriétés mécaniques post-corrosion des échafaudages métalliques résorbables en fonction de leurs caractéristiques architecturales post-corrosion font défaut dans la littérature. Ce projet de doctorat porte sur le comportement mécanique de la mousse de fer galvanisée à cellules ouvertes avec des entretoises creuses

pour les applications d'échafaudage osseux. En particulier, les relations entre les propriétés structurales et mécaniques, les propriétés mécaniques après corrosion et les paramètres micro-architecturaux induits par la corrosion des mousses de fer ont été explorées. En outre, des modèles d'éléments finis idéalisés (mousse Kelvin) d'un témoin ainsi qu'un échantillon de mousse de fer corrodé ont été développés sur la base de mesures de tomographie micro-calculée et de modes de corrosion pour prédire la réponse mécanique post-corrosion de la mousse de fer (*test in silico*).

La thèse comprend une introduction, trois chapitres contenant une revue approfondie de la littérature et les études menées pour le projet de doctorat, et une section Conclusion. Des données supplémentaires sur les études réalisées se trouvent en annexe.

Dans l'introduction, un bref historique sur les échafaudages osseux, l'application de métaux poreux biodégradables (résorbables) dans les échafaudages, l'énoncé du problème, les objectifs de recherche, la stratégie de recherche et la nouveauté de cette recherche sont présentés.

Le chapitre 1 contient une revue approfondie de la littérature sur les sujets pertinents au sujet de la thèse tels que l'application de métaux biodégradables comme implants temporaires, la fabrication et l'application de mousses métalliques résorbables comme échafaudages osseux ainsi que leurs propriétés mécaniques et de corrosion, temps de corrosion propriétés mécaniques dépendantes des échafaudages métalliques résorbables, approches de modélisation analytique et informatique pour prédire le comportement mécanique des mousses métalliques et modélisation informatique de la dégradation dans les métaux résorbables.

Le chapitre 2 traite de la première étape du projet de doctorat qui était une étude sur les propriétés mécaniques des mousses de fer électrolytiques à cellules ouvertes avec entretoises creuses. Dans cette étude, des échantillons de mousses de fer aux propriétés architecturales différentes, c'est-à-dire la taille des alvéoles, l'épaisseur des branches et la taille des pores, ont subi des essais de compression mécanique et le rôle de leurs paramètres architecturaux ainsi que leur densité relative dans leurs différentes réponses à la compression (quasi-gradient élastique, élasticité et résistance à la compression) a été discuté. De plus, une modélisation par éléments finis des mousses Kelvin a été développée pour fournir une

meilleure compréhension des effets de creux des entretoises sur les propriétés mécaniques de la mousse. Le chapitre couvre une introduction, la méthodologie, les résultats, la discussion et une section de conclusion.

Le chapitre 3 traite des propriétés mécaniques post-corrosion et des configurations architecturales des mousses de fer à entretoises creuses. Les échantillons de mousse de fer ont subi des tests d'immersion dans une solution de Hanks jusqu'à 14 jours, suivis de tests de nettoyage et de compression mécanique. Les facteurs influençant les propriétés mécaniques de la mousse corrodée ont été explorés, c'est-à-dire la dégradation structurelle, les produits de corrosion adhérents et les changements micro-architecturaux au niveau des entretoises. une tomographie micro-calculée a été utilisée pour mesurer les paramètres architecturaux du contrôle et des mousses corrodées pendant 14 jours. Sur la base des mesures architecturales, des modèles d'éléments finis de mousse Kelvin ont été développés pour prédire la réponse mécanique des mousses corrodées. De plus, un nouveau modèle de mousse Kelvin a été développé pour prédire la réponse mécanique des mousses de fer corrodées sous corrosion homogène, le mécanisme de corrosion qui n'avait pas été observé dans les expériences.

Enfin, les faits saillants les plus importants des études sont présentés dans la section Conclusion. Aussi, les limites et les bénéfices potentiels des résultats de ce projet pour les futurs travaux de recherche sont expliqués, et de nouvelles idées pour les futurs projets concernant le comportement mécanique des mousses métalliques résorbables sont proposées.

Summary

Up to a few years ago, every year, in the United States, more than 500,000 people needed to repair their bone defects [1]. It was predicted that the need for such repairs would double in US and worldwide by 2020 [1]. Bone grafting techniques are commonly used to heal large bone defects. However, there are certain drawbacks with bone grafting such as infection, pain, morbidity and shortage of donor site. Bone scaffolding is considered as an alternative approach to heal bone defects without complications raised from grafting. Bone scaffolds are considered as temporary implants, since after the formation of new tissue, their presence is not needed anymore.

Porous biodegradable (absorbable) metals have been developed and studied as temporary bone scaffolds. These porous structures provide mechanical support and biological space for tissue regeneration. These implants corrode during tissue regeneration process, and, ideally, they should disappear once the healing process ends. Thus, no secondary surgery to remove them would be needed.

One crucial task for absorbable bone scaffolds is to provide mechanical support for new tissue formation. The scaffolds must keep their mechanical integrity without failing due to mechanical loads applied from the surrounding environment. On the other hand, as orthopedic implants, their stiffness should not be higher than the surrounding bone tissue due to the risk of stress shielding. Thus, understanding the influencing factors on the mechanical response of the bone scaffold during degradation and predicting their mechanical properties are crucial. Design and fabrication of absorbable scaffolds is a topic of interest for researchers.

Detailed analyses that explain the post-corrosion mechanical properties of absorbable metal scaffolds based on their post-corrosion architectural features are lacking in the literature. This PhD project addresses the mechanical behavior of electroplated open cell iron foam with hollow struts for bone scaffolding applications. In particular, the structural-mechanical properties relationships, post-corrosion mechanical properties and the corrosion-induced micro-architectural parameters of the iron foams have been explored. In addition, idealized finite element models (Kelvin foam) of a control as well as a corroded iron foam specimen

were developed based on micro-computed tomography measurements and corrosion modes to predict the post-corrosion mechanical response of the iron foam (*in silico* test).

The thesis comprises an Introduction, three chapters containing a thorough literature review and the studies conducted for the PhD project, and a Conclusion section. Additional data about the performed studies are found in the Appendix.

In the Introduction, a brief background on bone scaffolds, the application of porous biodegradable (absorbable) metals in scaffolding, problem statement, research objectives, research strategy, and the novelty of the research are presented.

Chapter 1 contains a thorough literature review on the subjects relevant to the topic of the thesis such as the application of biodegradable metals as temporary implants, fabrication and application of absorbable metal foams as bone scaffolds as well as their mechanical and corrosion properties, corrosion-time dependent mechanical properties of absorbable metallic scaffolds, analytical and computational modelling approaches to predict the mechanical behavior of metal foams and computational modeling of degradation in absorbable metals.

Chapter 2 discusses the first step of the PhD project which was a study on the mechanical properties of the electroplated open-cell iron foams with hollow struts. In this study, samples of iron foams with different architectural properties, i.e. cell size, branch-strut thickness and pore size, underwent mechanical compression tests and the role of their architectural parameters as well as their relative density in their different compressive response (quasi-elastic gradient, yield and compressive strength) was discussed. In addition, finite element modeling of Kelvin foams was developed to provide a better understanding of the strut hollowness effects on the foam mechanical properties. The chapter covers an introduction, the methodology, results, discussion, and a concluding section.

Chapter 3 discusses the post-corrosion mechanical properties and architectural configurations of the iron foams with hollow struts. The iron foam samples underwent immersion tests in a Hanks' solution up to 14 days which were followed by cleaning and mechanical compression tests. The factors influencing the corroded foam mechanical properties were explored, i.e. structural degradation, adherent corrosion products and micro-architectural changes on the strut level. micro-computed tomography was employed to

measure architectural parameters of the control and the 14-day corroded foams. Based on the architectural measurements, Kelvin foam finite element models were developed to predict the mechanical response of the corroded foams. Also, a new Kelvin foam model was developed to predict the mechanical response of the corroded iron foams under homogeneous corrosion, the corrosion mechanism which had not been observed in the experiments.

Finally, the most important highlights of the studies are presented in the Conclusion section. Also, the limitations and the potential benefits of the results of this project for the future research works is explained, and new ideas for the future projects concerning the mechanical behavior of absorbable metal foams is proposed.

Table of Contents

Résumé.....	iii
Summary	vi
Table of Contents	ix
List of Figures	xii
List of Tables.....	xv
List of Important Symbols and Abbreviations	xvi
Acknowledgments.....	xvii
Foreword	xviii
<i>Introduction</i>	1
Bone scaffolds.....	1
Biodegradable porous metals as bone scaffolds.....	3
Research problem.....	4
Research objectives	5
Strategy	5
The novelty of the research	7
1. <i>Literature Review</i>	8
1.1. Biodegradable metals	8
1.2. Iron-based biodegradable metals.....	10
1.3. Metal foams.....	16
1.4. Basic fabrication techniques of metal foams.....	16
1.5. Fabrication of biodegradable porous metals	19
1.6. Mechanical and corrosion properties of biodegradable porous metals	23
1.7. Corrosion-time dependent mechanical properties of biodegradable porous metals.....	26
1.8. Effect of graded structures on corrosion and corrosion time-dependent mechanical properties of biodegradable metal scaffolds.....	33
1.9. Modeling approaches to study the mechanical behavior of metal foams.....	38
1.9.1. Analytical modeling	38
1.9.2. Finite element modeling.....	40
1.10. Computational modeling of degradation in metals	49
2. <i>Mechanical Properties of Open-Cell Iron Foams with Hollow Struts</i>	53

2.1. Introduction	53
2.2. Methodology	53
2.2.1. Iron foam samples	53
2.2.2. Mechanical testing.....	54
2.2.3. Compressive properties	55
2.2.4. Kelvin foam finite element model.....	55
2.2.5. Statistical analysis	57
2.3. Results.....	57
2.3.1. Architectural properties of the iron foams	57
2.3.2. Compressive behavior of the iron foams.....	58
2.3.3. Statistical analysis	59
2.3.4. Computational modeling.....	60
2.3.5. Deformation of the iron foam struts under compression.....	62
2.4. Discussion	64
2.4.1. Mechanical properties of the iron foams, the influence of architectural properties	64
2.4.2. Deformation of struts under compression	70
2.5. Concluding remarks	71
3. <i>Post-corrosion Mechanical Properties of Absorbable Open Cell Iron Foams with Hollow</i> <i>Struts</i>	72
Résumé.....	72
Abstract	72
3.1. Introduction	73
3.2. Materials and methods	75
3.2.1. Sample preparation.....	75
3.2.2. Immersion tests	76
3.2.3. Material characterization.....	77
3.2.4. Mechanical tests	77
3.2.5. Ashby-Gibson models for elastic modulus and plastic collapse stress of open cell foams	77
3.2.6. Measurement of architectural parameters	78
3.2.7. Computational modelling.....	81
3.3. Results and discussion.....	87
3.3.1. Immersion tests	87
3.3.2. Effect of corrosion on physical and mechanical properties of iron foams	89
3.3.3. Effect of corrosion on architectural parameters of the foams	94

3.4. Conclusions	100
<i>Conclusion</i>	102
Appendix.....	105
A. Architectural features of the iron foam samples in the study presented in Chapter 2.....	105
A.1. Definition of architectural parameters.....	105
A.2. Measurements of the architectural parameters on SEM images of the iron foams	106
B. Supplementary material of Chapter 3, post-corrosion mechanical properties of absorbable open cell iron foams with hollow struts.....	108
B.1. Geometrical and dimensional configurations of iron foams.....	108
B.2. Design steps of the Kelvin struts in SolidWorks using μ CT measurements	109
B.3. Strut thickness estimation.....	110
B.4. Kelvin foam model	113
B.5. Cross-section of corroded specimens	114
B.6. Compression stress-strain curves.....	117
Bibliography.....	118

List of Figures

Figure 0.1- Bone tissue microstructure and SEM micrographs of a cancellous and a cortical bone tissue (adapted from references [6, 11, 12]).....	2
Figure 1.1- Basic fabrication techniques of cellular metals (adapted from [97]).....	17
Figure 1.2- Schematic representation of a) space holder b) replication techniques to fabricate porous metals (adapted from [102] and [17])	18
Figure 1.3- a) Alantum open-cell iron foam structure, b) Hollow strut	19
Figure 1.4- Fabrication of an Mg-Zn scaffold with space holder technique (adapted from [105])..	20
Figure 1.5- Fabrication of a porous metal scaffold with air-pressure infiltration combined with space holder methods (adapted from [107]).....	21
Figure 1.6- Fabrication of Fe scaffolds using 3D-printed sacrificial structure and pressureless microwave sintering (adapted from [112]).....	22
Figure 1.7- Corrosion-time dependent mechanical properties of AM porous a) Fe, b) Mg alloy, c) Zn, AP: as-built porosity from μ CT measurements (adapted from [23, 29, 33]).....	30
Figure 1.8- Corroded porous Mg samples (before and after cleaning) after different immersion times (adapted from [31])	31
Figure 1.9- Variation of mechanical properties of porous Mg with dynamic immersion time (adapted from [31])	32
Figure 1.10- a) Topology of additively manufactured (AM) biodegradable porous iron with uniform and functionally graded structures, b) 3D reconstruction (μ CT) of 28-day corroded AM biodegradable porous zinc specimens (gray) and their corrosion products (red). (adapted from [15, 24])	37
Figure 1.11- Corrosion-time dependent mechanical properties of biodegradable porous zinc with uniform and functionally graded structures. D: dynamic immersion, S: static immersion, AB: as-built. (adapted from [15])	38
Figure 1.12- The cubic open cell model used by Ashby and Gibson (adapted from [99])	39
Figure 1.13- Generation of a porous structure with the aid of Voronoi polyhedral cells (adapted from [129]).....	42
Figure 1.14- Voronoi foam models with a a) low, and b) high degree of irregularity (adapted from [126]).....	43
Figure 1.15- a) Micro-CT image of a PU foam and a single strut with varied cross-sectional areas (red region), b) An anisotropic Kelvin foam structure and a junction design (red region) (adapted from [131, 132]).....	45
Figure 1.16- A Kelvin unit cell (left) and a Kelvin foam (right) made of repeating the unit cell (adapted from [134])	46
Figure 1.17- a) Micro-CT of a cell with hollow struts, b) Compressive loading-unloading responses of the Ni-Cr open-cell foam, c) Cluster of Kelvin cells and strut architectural configuration (adapted from [130]).....	48
Figure 1.18- 2D μ CT slices (left), a 3D reconstructed image (middle) and a discretized model with tetrahedral elements (right) of a closed-cell foam (adapted from [136])	49
Figure 1.19- The results of the uniform (left) and pitting (right) corrosion models on the structure of a stent model (adapted from [51])	51
Figure 1.20- a) A corroded porous Mg specimen and b) its μ CT model, c) FE model of a corroded porous Mg under loading (adapted from [54]).....	52

Figure 2.1- Scanning electron microscope (SEM) images of iron foam structures: (a) IF45; (b) IF58; and (c) IF80	57
Figure 2.2- The stress-strain curves of the compression tests for different cell sizes: (a) IF45, (b) IF58, and (c) IF80	58
Figure 2.3- Box charts for iron foam specimens of different cell sizes: (a) QEG; (b) Yield strength; (c) Compressive strength.....	60
Figure 2.4- Architectural parameters of the Kelvin foams, a) Solid-strut cross-section, b) Hollow-strut cross-section, c) Kelvin unit cell, d) Kelvin foam side view	60
Figure 2.5- Mechanical response of the Kelvin foams with a) solid and b) hollow struts	62
Figure 2.6- Deformed structure of four IF45 specimens at compression strain of: (a) 10.8%; (b) 12.8%; (c) 29.8%; and (d) 49.5%	63
Figure 2.7- Different shapes formed on plastically deformed struts: (a) S-shape; (b) C-shape; and (c) Deformation bands	64
Figure 2.8 - A typical stress-strain response of a metal foam under compression (adapted from [141]).....	65
Figure 2.9- A simple model of an open cell foam experiencing: (a) Linear elastic deformation; and (b) Formation of plastic hinges during plastic collapse (adapted from [99])	70
Figure 3.1- (a) (sub)layer division for μ CT analysis, (b) 3D reconstructed model of an iron foam (control specimen).....	79
Figure 3.2- (a) 3D reconstruction of a single strut with the key locations where the cross-sectional measurements are conducted, and (b) Strut cross-sectional parameters	80
Figure 3.3- (a) Kelvin strut cross-section, (b) Half-strut with a varying cross-section, (c) Single porous Kelvin cell with hollow struts and (d) the Kelvin cell suitable for tessellation.....	83
Figure 3.4- Surface of (a) control, (b) 3d, (c) 7d and (d) 14d corroded specimen before cleaning, and the SEM image of (e) control, (f) 3d, (g) 5d, (h) 7d, and (i) 14d corroded specimens after cleaning	88
Figure 3.5- Effect of corrosion on the mass and the density of iron foams: (a) Mass-gain after immersion, (b) Mass-loss after cleaning, (c) Total mass-change after cleaning and (d) Foam density of the cleaned samples.....	90
Figure 3.6- Presence of pits on a strut of (a) 7d and (b) 14d specimens.	91
Figure 3.7- Variation of mechanical properties with immersion time: (a) Quasi-elastic gradient, (b) Compressive strength, (c) Yield strength, and (d) Energy absorbability.	92
Figure 3.8- Variation of (a) strut thickness in the Control and 14d foam layers (b) cross-sectional solid area along the strut length in layers of the control and the 14d specimens.	95
Figure 3.9- Distribution of pore-size on the surface of the control and the 14d foam samples.	97
Figure 3.10- Control-Kelvin foam in undeformed and deformed states simulated by FEM.....	97
Figure 3.11- (a) Mechanical response (stress-strain curve) of Kelvin (FEM) and Experiment foams, and comparison of the b) elastic parameters and c) strength parameters obtained from the FE models and the experiments.	98
Figure A.1- Definition of cell size and pore size for the iron foams presented in Chapter 2.....	105
Figure A.2- Definition of different strut thickness parameters as well as the strut length for the iron foams presented in Chapter 2	106
Figure B.1- SEM image of the iron foam microstructure with definition of the geometrical features.	108
Figure B.2- (a) Structure containing 4 half-struts meeting at the node in a Kelvin cell, (b) A triangular cross-section of a Kelvin strut.	112
Figure B.3- Examples of micropores on the surface of two struts of iron foams used in this study	113

Figure B.4- Kelvin foam model, compression plate and the boundary conditions of the model. ... 114
Figure B.5- Cross-sectional observation of an uncleaned (a) 1d, (b) 3d, (c) 5d, (d) 7d, and (e) 10d specimens. 115
Figure B.6- Examples of adherent corrosion products and their EDS analyses, (a) 3d, (b) 5d, and (c) 14d..... 116
Figure B.7- Compressive response of (a) control and (b, c, d) corroded samples 117

List of Tables

Table 1.1- The porosity and mechanical properties of the samples in reference [24].....	35
Table 2.1- Relative density, cell size, pore size, end-strut and branch-strut thickness values of the iron foams.....	58
Table 2.2- Compressive properties of iron foam samples.....	59
Table 2.3- Dimensions and relative density of the Kelvin foams	61
Table 2.4- Mechanical properties of the Kelvin foams	61
Table 2.5- Variation of f_1 and f_2 as a function of r values.....	69
Table 3.1- Summary of the parameters and the methods by which their values are obtained	86
Table 3.2- Density and mechanical properties of the control, 7-day and 14-day corroded iron foams determined from experimentation	91
Table 3.3- Mechanical properties of Kelvin foams and the corresponding experimental results	99
Table A.1- Measurements of architectural parameters of the iron foams presented in Chapter 2 ..	106
Table B.1- Dimension and strut thickness in the sublayers (whole-body analysis) of the iron foams analyzed with BoneJ	108
Table B.2- Strut dimensions and relative densities of the developed Kelvin foams.	112

List of Important Symbols and Abbreviations

FE: Finite element

μCT: Micro-computed tomography

SEM: Scanning electron microscopy

QEG: Quasi-elastic gradient

σ_c : Compressive strength of the iron foams

σ_y : Yield strength of the iron foam

W: Energy absorbability up to 50% strain

M_{bi} : Mass of an iron foam specimen before immersion

M_{ai-bc} : Mass of an iron foam specimen after immersion and before cleaning

M_{ai-ac} : Mass of an iron foam specimen after immersion and after cleaning

$\frac{\bar{\rho}}{\rho_s}$: Relative density of a foam, $\bar{\rho}$: Density of the foam, ρ_s : Density of the parent material of the foam

\bar{E} : Elastic modulus of a foam

E_s : Elastic modulus of the parent material of a foam

$\bar{\sigma}_{pl}$: Plastic collapse stress of a foam

σ_{ys} : Yield stress of the parent material of a foam

r: Hollowness ratio of a strut

f_1 : Enhancement function of elastic modulus in open cell foams with hollow struts

f_2 : Enhancement function of plastic collapse stress in open cell foams with hollow struts

E_{ef} : Effective elastic parameter of material

σ_{yef} : Effective yield parameter of material

Acknowledgments

I would like to express my gratitude to my supervisor, Prof. Hermawan, for giving me the opportunity to work on this PhD project and providing financial and academic support along this journey. I learned from him the basic principles of scientific research. The academic freedom he provided for me during this PhD program has helped me to become an independent researcher. I highly appreciate his availability whenever I needed advice regarding my project.

I am also deeply thankful to my co-supervisor Prof. Akbarzadeh for all the academic support and extremely helpful guidance through out my PhD program. His presence as my co-supervisor helped me to overcome various hurdles I was facing as a PhD student. I learned from him how to prepare a high-quality research work. I also learned from him the value of professionalism and respect toward people in the workplace.

Beside my supervisor and co-supervisor, I am highly thankful to other esteemed jury members, Dr. Carl Blais, Dr. Mehdi Razavi and Dr. Hadi Nur, for the time and energy they put to evaluate my thesis and for their insightful comments.

I am thankful to Prof. Diego Mantovani of Laval University for giving access to the Instron testing systems in his lab to perform the uniaxial compression tests and for providing me with many insightful ideas about high-quality scientific research during my program.

I would like to thank the research associates and technicians of the Laboratoire de Biomatériaux et de Bioingénierie (LBB) and the Metallurgical and Materials Engineering department at Laval University, particularly Mr. Bernard Drouin for training me to use the compression test device and Mr. Daniel Marcotte for his significantly helpful technical supports for the experiments. I am also grateful to my friend Dr. Malgorzata Sikora-Jasinska for providing training to conduct immersion tests and for helpful discussions regarding the corrosion-related aspects of my project.

I am grateful for my family and friends for supporting me during my PhD program.

Finally, I am thankful to Laval University for providing an enriching environment for my professional and personal growth during the past five years.

Foreword

This PhD project was completed under the supervision of Dr. Hendra Hermawan of Laval University and the co-supervision of Dr. Hamid Akbarzadeh of McGill University. I first-authored two peer-reviewed journal article during the PhD program, yet the presented document is a hybrid thesis with the insertion of one article (the second published article).

Chapter 2 is based on the first article:

R. Alavi, A. Trenggono, S. Champagne, H. Hermawan, *Investigation on Mechanical Behavior of Biodegradable Iron Foams under Different Compression Test Conditions*, *Metals* 7(6) (2017) 202.

The results of the article were selectively presented in the thesis, and new finite element modeling results were added later, and the discussion was improved. The main part of the experimental work presented in Chapter 2, i.e. preparing iron foam samples of different cell size and the associated compression tests and data collection had been carried out by Adhitya Trenggono and Sébastien Champagne, and the main part of the architectural measurements of the foams had been conducted by Adhitya Trenggono. The experimental work regarding strut deformation mechanisms, all the works concerning the computational modeling as well as all the data analysis were carried out by myself. All the aforementioned tasks were conducted under the supervision of Hendra Hermawan.

Chapter 3, is the second published article, available online on 23 February 2021, with a few corrections in the references, and a minor typo correction in Eq. 2.2 _equivalent to Eq. 6 of the published document:

Alavi, R., A. H. Akbarzadeh, and H. Hermawan. *Post-corrosion mechanical properties of absorbable open cell iron foams with hollow struts*. *Journal of the Mechanical Behavior of Biomedical Materials* (2021): 104413.

The contributions of the authors are as follows:

Reza Alavi: Conceptualization, Methodology, Formal analysis, Writing- Original draft preparation. Hamid Akbarzadeh: Methodology, Validation, Formal analysis, Writing-

Reviewing and Editing. Hendra Hermawan: Conceptualization, Methodology, Validation, Formal analysis, Writing- Reviewing and Editing, Supervision, Funding acquisition.

Introduction

Bone scaffolds

Up to a few years ago, every year in the United States, more than 500,000 people needed to repair their bone defects costing more than \$2.5 billion [1]. Considering the aging population and other factors such as lack of sufficient physical activity, it was predicted that the need for such repairs would double in US and worldwide by 2020 [1]. A common approach to heal large bone defects, i.e. great loss of bone in an anatomic region, is bone grafting [2, 3]. Two common grafting techniques are autologous and allogenic grafting [3] wherein a tissue is removed from an anatomic site of either the same person (autologous grafting) or another person (allogenic grafting) and then planted in the bone defect area [3]. However, there exist drawbacks with each of the bone grafting techniques such as infection, pain, morbidity and shortage of donor site and transmission of infectious diseases [4, 5]. Bone scaffolds are considered as substitute to bone grafts without their inherent complications [4, 6]. They provide mechanical support and space for regeneration of bone tissues [7]. Bone tissue scaffolds can be considered as temporary implants since they are not needed after the complete formation of new tissues. Absorbability (biodegradability) is one of the inherent characteristics of temporary tissue scaffolds [8]. An ideal temporary scaffold degrades gradually while providing mechanical and biological support for tissue formation. Porosity is another key feature of bone scaffolds since it allows cell migration and proliferation as well as transferring oxygen, nutrients and waste metabolic products [9]. The pores must be extensively interconnected (open-cell) to facilitate tissue regeneration, vascularization and nutrient transfers [10]. The highly porous microstructure of a cancellous bone tissues is demonstrated in Figure 0.1 (adapted from [6, 11, 12]). Design and fabrication of biodegradable tissue scaffolds are topics of interest for the researchers due to the growing need for such implants [9].

Biodegradable/absorbable tissue scaffolds need to maintain their mechanical integrity during the degradation process. This is to prevent implant failure under mechanical loads [6, 13]. However, using orthopedic implants with high stiffness can cause stress shielding which

results in bone thickness reduction and mass loss [14]. This explains the need for absorbable scaffolds with *bone-mimicking* [15] mechanical properties [7].

Biocompatibility of the scaffolds and their degradation products is another crucial design factor [9, 16]. Also, the microenvironmental changes made by generation of the degradation products (corrosion products) should not risk the scaffold biocompatibility [7].

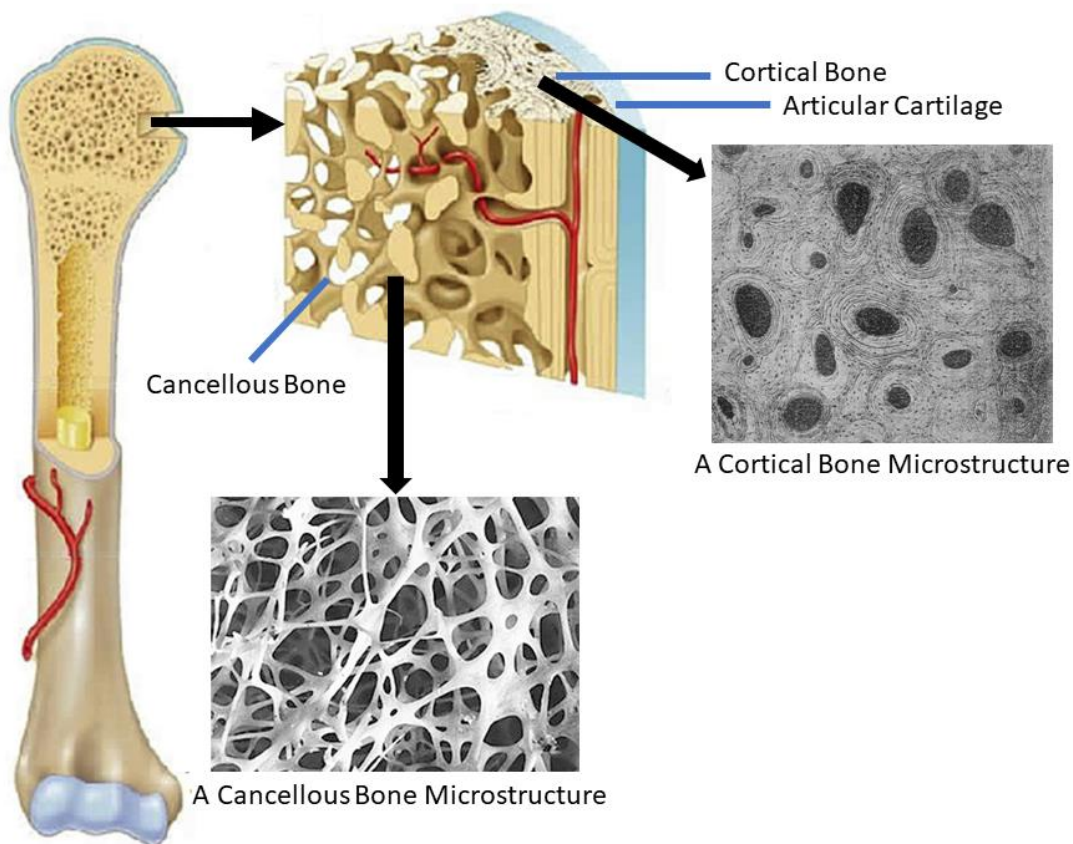


Figure 0.1- Bone tissue microstructure and SEM micrographs of a cancellous and a cortical bone tissue (adapted from references [6, 11, 12])

Biodegradable porous metals as bone scaffolds

Biodegradable (absorbable) scaffolds could be based on ceramics, polymers and metals [17]. Brittleness of ceramics and low stiffness and strength of polymers make it challenging to use them for load-bearing application [17, 18]. Metals on the other hand possess superior mechanical properties needed for load bearing applications such as strength and resistance against fatigue and fracture [17, 18]. This has led to an extensive research on biodegradable metallic scaffolds, i.e. porous Fe-based [19-25], Mg-based [26-32], and Zn-based [15, 33-37] metals.

Although the term “absorbable” is deemed more appropriate than “biodegradable” for biomedical implants [38], both terms are interchangeably used in this document, due to the common use of “biodegradable” in association with temporary metallic scaffolds in the literature.

An ideal biodegradable metallic implant corrodes gradually (and safely) during tissue formation and leave no residue after the healing process [39]. This means that the biodegradable metal should be metabolized in the body, and it needs to have a suitable corrosion rate [39]. Magnesium is generally known for its high corrosion rate [40]. One of the challenges facing Mg-based implants is the generation of hydrogen gas during corrosion of Mg [29]. An intense evolution of hydrogen can cause problems such as disturbing the tissue healing, thus a great deal of research has been conducted to slow down the corrosion of Mg-based implants [29, 30, 41]. Iron, however, has the lowest corrosion rate and the highest tensile strength and hardness among the three biodegradable metal elements [40].

In this study, highly porous open-cell iron foams (above 90 % porosity) with hollow struts (manufactured by electroplating process [42]) were investigated as a potential absorbable cancellous bone scaffold. The elastic modulus and compressive strength for certain types of human cancellous bone (with open or closed cells) is approximately 10~190 MPa and 0.25~35 MPa, respectively [43]. The values of the stiffness (i.e. quasi-elastic gradient) and the compressive strength of the iron foams used in this study were within the order of the corresponding properties of the human cancellous bones [43]. Biodegradable iron implants

have shown promising results in terms of biocompatibility [44, 45] , however, more research is needed to evaluate the long term effects of such implants [44].

Research problem

Corrosion of absorbable metallic implants introduces a potential risk for mechanical failure [46]. Therefore, understanding the variation of mechanical properties as well as the factors influencing the post-corrosion mechanical response of the scaffold is crucial. The architectural features highly influence the mechanical properties of porous materials [47, 48]. Corrosion alters the microarchitecture of metallic foams, leading to a variation in their mechanical properties [19]. This highlights the necessity to study the corrosion-induced architectural features (e.g. pore size and strut shape/dimension) of the biodegradable porous scaffolds.

A few studies have investigated the variations of the mechanical properties of absorbable porous metals in the course of corrosion [15, 23, 28, 31, 33, 49, 50]. However, there is a lack of detailed analysis to explain such variations based on the corrosion-induced architectural features. According to the author's rigorous literature review, no study has assessed the variation of the micro-architecture of iron foams with hollow struts after corrosion.

Predicting the post-corrosion mechanical response of the load-bearing biodegradable implants in the design stage can minimize the implant failure; it helps to design scaffolds with sufficient post-corrosion mechanical properties to support the newly formed tissues. Finite element (FE) modeling has been performed to explore and predict the corrosion-induced mechanical behavior of absorbable metallic stents [51, 52]. There are a limited number of research works that address the post-corrosion mechanical response of the biodegradable scaffolds using FE models [53, 54]. Predictive FE models (based on measurements of post-corrosion micro-architectural configurations and the expected corrosion modes, e.g. homogeneous or inhomogeneous) that estimate the mechanical behavior of absorbable open cell metallic scaffolds with hollow struts are still lacking in the literature.

The main focus of this study is to explore the corrosion-induced mechanical behavior and architectural parameters of open-cell iron foams with hollow struts (Chapter 3). Also, it is intended to develop a finite element model based on the post-corrosion micro-architectural data to predict the mechanical behavior of the corroded scaffold (Chapter 3). Prior to that, the structural-mechanical properties relationship of the open cell iron foams with hollow struts (manufactured by electroplating) is investigated to deepen the understanding on the influence of architectural factors on the mechanical properties of this particular type of foam (Chapter 2).

Research objectives

Three objectives are determined in this study:

- 1- To study the effects of architectural features (e.g. cell/pore size, strut thickness, relative density) on the mechanical properties of the electroplated open cell iron foams with hollow struts (e.g. stiffness, yield and compressive strength).
- 2- To understand the corrosion-time dependent mechanical properties and architectural features of open-cell iron foams with hollow struts. The studied mechanical properties are quasi-elastic gradient (stiffness), yield strength, compressive strength and energy absorbability, and the architectural features include cross-sectional area and thickness of struts and pore sizes.
- 3- To develop a finite element computational model to estimate the corrosion-induced mechanical properties of the absorbable iron scaffolds based on their corrosion-induced microstructure.

Strategy

To address the first objective, samples of open cell iron foams with hollow struts and with different architectural features (i.e. cell/pore size, strut thickness, relative density) underwent uniaxial compression tests. The foams were manufactured by Alantum [42], and they had nominal cell sizes of 400 μm (IF40), 580 μm (IF58) and 800 μm (IF80). Following the compression tests, mechanical properties of the samples (i.e. quasi-elastic gradient, yield and compressive strength) were compared against each other in light of their architectural

differences. In addition, *in silico* compression tests on idealized Kelvin cell structures [55, 56] were carried out in finite element (FE) framework to explore the effects of architectural feature (strut cross-sectional size/cell size, strut hollowness) on the mechanical properties of the foams.

To meet the second objective, iron foams with nominal cell size of 800 μm underwent *in vitro* static immersion tests in a simulated biological environment up to 14 days; this was followed by cleaning the samples, diligent mass measurements and uniaxial compression tests on the corroded samples. The microarchitecture of non-immersed (control) and 14-day-immersed (14d) specimens was elicited using micro-computed tomography (μCT) and scanning electron microscopy (SEM) imaging.

Although *in vitro* immersion tests do not perfectly represent the *in vivo* condition and they have shown corrosion-rate results incompatible with those of the *in vivo* tests [38], they have been widely used to monitor the variation of mechanical properties of absorbable metals [16, 23, 28, 57-60].

The third objective was addressed by conducting *in silico* compression tests on idealized Kelvin cellular structures [55, 56] that represented the control (Kelvin-Control) and the 14d (Kelvin-14d) specimens. The *in silico* tests were conducted in the FE framework by assuming an elastic-perfectly plastic constitutive material model. The predicted mechanical properties after 14 days of immersion were compared against the experimental results. Eventually, in order to understand the effect of corrosion mode (homogenous or inhomogeneous) on the mechanical properties, a new Kelvin foam (Kelvin-14d-HC) was developed and underwent the same *in silico* compression tests as the other Kelvin foams. The new foam had a similar relative density as that of Kelvin-14d foam, but, unlike Kelvin-14d, it represented a homogeneously corroded structure. The experimental results only demonstrated inhomogeneous corrosion after 14 days of immersion.

In vitro immersion tests in conjunction with elastic-plastic FE modeling have been performed to predict the variation of mechanical properties in biodegradable metals (Mg-based and Zn-based specimens [49, 61]).

The novelty of the research

To the best of the author's knowledge, the conducted experiments and analyses in this PhD project are the first of their kind among research works concerning either absorbable metallic scaffolds in general or electroplated open-cell iron foams with hollow struts in particular.

The experiments/analyses are as follows:

Investigating the influence of architecture on mechanical properties of the electroplated open cell iron foams with hollow struts. This was realized by performing compression tests on samples of different architectural configurations (Chapter 2), carrying out static immersion tests of different durations on this type of foam in conjunction with meticulous analysis of the influence of corrosion products on the mechanical properties of the degrading iron scaffolds (Chapter 3), detailed post-corrosion micro-architectural measurements of the foams on the strut level (Chapter 3), and developing idealized predictive finite element model (Kelvin foam) based on the post-corrosion micro-architectural measurements and the expected corrosion modes (Chapter 3).

1. Literature Review

1.1. Biodegradable metals

Based on their type of application, biomedical implants are expected to serve in the body either permanently or temporarily. Temporary applications target those problems which could be fixed using an implant in a limited time, e.g. bone tissue regeneration [5], cardiovascular [62] or ureteral stent [63]. An ideal permanent implant is corrosion resistant [64, 65] and lasts for a long period [66]. However, when the application is temporary, it is desired that the implant disappears when the healing period is over to prevent a second surgery for implant removal [67] and to avoid potential complications caused by permanent implants [68]. Also, the degradation rate of the biodegradable implant should not be so high to compromise the mechanical integrity during service time [69].

Biodegradable metals are suitable materials for fabrication of temporary implants. A biodegradable metal used as a temporary implant must show acceptable biocompatibility and mechanical properties. Thus far, Fe, Mg and Zn and their alloys have been investigated as potential biodegradable metals which meet these two requirements; in a review [70], the three metals and their alloys were investigated in terms of their mechanical properties, biocompatibility, and degradation behavior for their potential use as biodegradable sutures. The authors highlighted that degradation rate of Mg and its alloys, without applying surface engineering techniques, is too fast for some suturing applications. Also, among the three investigated metals, iron alloys had the best mechanical properties for suturing application. However, their challenge is to overcome their slow degradation while keeping the amount of released iron compounds below the recommended daily intake of iron, i.e. 6 mg/day to 20 mg/day for adults. Finally, the authors pointed out that the degradation rate of Zn is between that of Mg and Fe.

In reference [40], mechanical properties and corrosion behavior of the three metals and their alloys were investigated. To study the corrosion behavior, *in vitro* immersion tests in a simulated physiological solution (SPS, 9 g/L NaCl, initial pH of 6.2) for 168 h (7 days) at

37 °C were carried out. It was observed that the pure Mg and pure Zn (as cast) had the lowest hardness and tensile strength (lower than those of pure Fe) not going beyond 50 HV 5 and 130 MPa, respectively. Pure Fe (as cast) had an approximate hardness and tensile strength of 56 HV 5 and 163 MPa, respectively. Hot forging increased the hardness and tensile strength of pure iron to ~100 HV 5 and ~300 MPa, respectively. On the other hand, Fe-30Mn (as hot forged) showed the highest of the both factors, i.e. ~175 HV 5 and ~515 MPa. As cast Fe also showed a significantly higher elongation than as-cast Mg and Zn, and the as-hot forged Fe had the highest elongation among all the investigated pure metals and alloys. Pure Mg demonstrated the highest corrosion rate while pure Fe and Fe-30Mn demonstrated the lowest of that. The authors attributed the low corrosion rate of Fe-based metals to two factors: 1- the low concentration of dissolved oxygen whose presence is needed for dissolution of Fe, 2- formation of the relatively protective corrosion product layer.

Chen et al. [71] also compared the corrosion behavior of pure Zn with that of pure Fe and pure Mg using electrochemical tests on samples that had been immersed for different periods of time (3, 5, 7, 14 and 21 days) in phosphate buffered saline (PBS). Also, PBS was used as electrolyte at the temperature of 37 ± 0.5 °C for the electrochemical tests. The results of transient electrochemical techniques showed that the corrosion rate of Zn was between that of Fe and Mg. However, the electrochemical tests on the immersed samples suggested that in the long run (up to 21 days of immersion) the corrosion rate of Zn highly surpassed that of Fe and Mg. Zn initially (after 3 days of immersion) demonstrated a somewhat uniform corrosion, but, in longer immersion periods, more localized corrosion with non-adherent degradation products appeared. Therefore, the authors questioned the suitability of Zn implants for long term applications considering the localized corrosion and increase of the degradation rate, endangering the mechanical integrity during service time.

Each of the pure biodegradable metals is recognized by some challenges and advantages: Mg is well-known for rapid degradation which not only raise the risk of premature failure, but also it can disturb the tissue healing process due to hydrogen evolution [30]. Thus, many researchers have investigated various biodegradable Mg-based alloys and studied their corrosion behavior. A few of the studied Mg alloy systems are: Mg-Zn [72], Mg-Sr [73], Mg-Zn-Mn [74], Mg-RE(rare earth elements) [75] and Mg-Zn-RE-Ca [76]. On the other hand,

Mg has an elastic modulus (41-45 GPa) closer to that of the cortical bone (7-30 GPa) [9, 30], making it a suitable candidate for certain orthopedic applications. Fe, on the other hand, has demonstrated a slow corrosion which has become the research objective in many publications wherein different Fe alloy systems, e.g. Fe-Mn [77], Fe-Mn-C-Pd [78], Fe-Ga-X (X=B and TaC) [79], were investigated. Also, the superior mechanical properties of Fe (elastic modulus of ~200 GPa [80], annealed tensile strength of ~ 205 MPa [81]) has made it a good candidate for load-bearing implants, e.g. porous bone scaffolds [82, 83] and structural-strength-demanding implants e.g. coronary stents [38].

The research on Zn-based biodegradable metals is more recent. Zinc is generally known to corrode moderately without problems associated with degradation of Mg, i.e. fast corrosion, and hydrogen evolution, and Fe, i.e. slow corrosion and high volumes of corrosion products which slowly get cleared away [84, 85]. The mechanical properties of Zn-based metals are comparable with those of Fe and Mg-based metals [84]. However, there exist uncertainties about performance of Zn-based biodegradable implants due to the confirmed natural aging and creep of Zn-based alloys at room temperature (as the result of low melting point of Zn, i.e. $T = 419.5\text{ }^{\circ}\text{C}$). This could potentially lead to unfavorable deformation or failure because of structural and mechanical instability of the Zn-based implants [84, 86].

1.2. Iron-based biodegradable metals

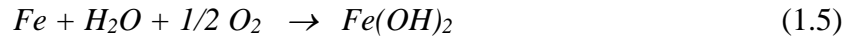
Corrosion of pure iron in an aqueous medium can be described by Eq. 1.1 to 1.6 [87]:



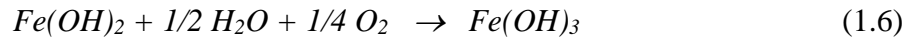
Eq. 1.1 is the anodic reaction and Eq. 1.2 represents a cathodic reaction in a deaerated solution. The reduction of H^{+} in neutral or alkaline aqueous media is slow. Dissolved oxygen in an aqueous medium accelerates the cathodic reaction as follows (depolarization):



Considering Eq. 1.4, by adding Eq. 1.1 and 1.3, it can be seen how ferrous hydroxide is formed (Eq. 1.5):



Ferrous hydroxide is white in the pure form, however it turns to green/green-black as the result of oxidation by air [87]. As the outside surface of ferrous hydroxide is exposed to dissolved oxygen, ferric hydroxide would be formed according to the following equation:



Ferric hydroxide is “orange to reddish brown” [87], and it makes the major part of the rust.

Degradation behavior of pure iron was first assessed by Peuster et al. in an *in vivo* study on biodegradable stents [70, 88]: the iron stents were implanted in the descending aorta of New Zealand rabbits, and follow-up angiographies were conducted up to 18 months. Although a mild inflammatory vessel response was observed, the authors deemed the biodegradable iron stent safe [88]. They realized that the *in vivo* degradation rates of the iron stents were lower than the expected *in-vitro* results, and recommended alloying and surface/structural modifications to obtain faster degradation [88].

Biodegradable iron is well-known for having low degradation rate. Schinhammer et al. [89]. tried to address this issue by applying a design strategy wherein the microstructure of pure iron was modified through different alloying and heat treatment (aging) parameters. The authors were also looking to improve the mechanical strength and ductility of iron. Solution-heat-treated Fe-10Mn and Fe-10Mn-1Pd systems with or without additional heat treatment (aging) procedures were investigated. Solution-heat-treated Fe-10Mn and Fe-10Mn-1Pd without aging treatments were highly brittle. After one of the aging treatments, the uniform

elongation of Fe-10Mn-1Pd increased from 2% to 8% while its tensile strength decreased from 1500 MPa to 1450 MPa. The tensile strength of Fe-10Mn and Fe-10Mn-1Pd samples which underwent additional aging treatments were higher than that of pure iron and carbon steel. Depending on the heat treatment method, the yield strength of Fe-10Mn-Pd was higher than that of Fe-10Mn by 100 or 200 MPa. The higher strength of Fe-10Mn-Pd was attributed to Pd intermetallic phase particles. The effect of aging heat treatment on the mechanical properties was emphasized (e.g. significant enhancement of ductility). That said, all the alloy samples showed a significantly lower elongation than that of pure iron. The low ductility of the alloys was attributed to martensite-rich microstructure and the supersaturated carbon (C) concentration. In both immersion and electrochemical impedance spectroscopy (EIS) tests, Fe-10Mn-Pd alloys generally demonstrated the highest degradation rate followed by Fe-10Mn and Fe (carbon steel) samples. Both alloys tended to have higher degradation rates than those of carbon steel samples after 24h and 48h of immersion in a SBF at $T = 37 \pm 1$ °C. For the case of Fe-Mn system, the increase of degradation rate was attributed to decreasing the standard electron potential by introducing Mn. Additionally, the authors argued that adding Pd increased the degradation of Fe-Mn system by creating nobler Pd-containing intermetallic phase acting as cathodic sites, thus promoting microgalvanic corrosion [89].

In another study [90], Heiden et al. investigated the degradation behavior of Fe-20% Mn (as-cast and cold-rolled) *in vitro* in an osteogenic medium over 90 days at a temperature of 37 ± 0.5 °C and pH of 7.4 ± 0.1 (inside an incubator). The effect of processing method of samples on degradation rate was also studied. The degradation behavior of the alloy was assessed via potentiostatic polarization and static immersion tests. Potentiostatic polarization tests showed that the pure iron degrades significantly slower than Fe-20Mn alloys and the cold rolling slowed down the degradation process. The average calculated degradation rate for pure iron, cold-rolled and as-cast alloys were 0.05, 0.54 and 0.94 mm/year, respectively. It was shown that after immersion of Fe-20Mn, an Fe-rich oxide layer started to form. Cracks started showing up on the oxide layer after around 5 days of immersion. The oxide layer protected the alloy against corrosion. However, after more than 50 days of immersion, the medium could slowly penetrate the oxide layer and attack the beneath layers which created localized corrosion. The electrochemical tests resulted in extremely higher corrosion rates as

compared to those of immersion tests. The maximum corrosion rate calculated via mass-loss method was $\sim 7 \times 10^{-9}$ mm/year (after 60 days of immersion). Eventually, they concluded that alloy composition and manufacturing techniques as well as the microstructure influence the structure of the Fe-rich oxide layer, influencing the degradation process of the alloy.

In the study of Cheng et al. [91], the effects of Au disc micro-pattern film coatings on corrosion of pure iron was studied. Electrochemical and static immersion tests (3, 10 and 30 days) were carried out at 37 ± 0.5 °C and within Hanks' solution. It was observed that the Au pattern coating increased the corrosion rate as well as the corrosion depth (which was increased by a factor of 3), and as the iron substrate was fully coated, even higher degradation rate was achieved. The higher corrosion rate of the coated samples as compared to the non-coated ones was explained by galvanic corrosion resulted from the difference between the standard potential of gold and iron ($1.52 - (-0.44) = 1.96$) with gold being a nobler element (cathode). Based on the electrochemical results, the authors speculated that the Au coating increased the degradation rate of the iron matrix more significantly than W, Pd and Pt which was attributed to the difference between the standard potentials and to the fashion they were introduced to the iron matrix, i.e. Au was present on the surface while the other three made a solid solution with the matrix. In addition, it was observed that the Au coating made the degradation of the pure iron more uniform due to the presence of extensively dispersed micro-galvanic corrosion sites.

In a comprehensive study [92], Liu and Zheng investigated the influence of various alloying elements, i.e. Co, Al, Mn, W, C, B, S, and Sn on degradation and mechanical behavior of pure iron within Fe-X alloy system. The measured amount of alloying elements were 3.31 at.% Mn, 3.48 at.% Co, 3.07 at.% Al, 3.28 at.% W, 3.05 at.% Sn, and 3.34 at.% B. To explore the influence of C and S, high carbon steel 1070 (~ 3 at.% C) and free cutting steel 1119 (0.5 at.% S) were selected. Except for Fe-C and Fe-S which were in as-rolled form, the other alloys were studied under both as-rolled and as-cast forms. Electrochemical tests, static immersion test (Hanks' solution, $T=37$ °C) and dynamic immersion tests (Hanks' solution, $T=36.9-37.1$ °C, $\text{pH}= 7.35-7.45$, dissolved oxygen= $2.8-3.2$ mg l^{-1}) were conducted to study the degradation behavior. The immersion time for the static tests was 3, 10, 30, 90 and 180 days and for dynamic tests was 30 days. As for the mechanical properties of the alloys, it was

observed that Fe-Sn showed a very low yield stress, tensile strength and elongation as compared to those of pure iron and other alloys. The authors attributed the low ductility to the “segregation” of Sn at grain boundaries. Yield and tensile strength of (as-rolled) pure iron were increased by adding W, B, C, Mn, Co, Al. The rolling process increased yield stress and tensile strength and reduced the elongation. It also slightly decreased the corrosion rate of the pure iron and Fe-X alloys (except for Fe-Co). Electrochemical data showed that as-rolled Fe-C had the highest corrosion rate. The static immersion test revealed that the long-term difference between the corrosion rate of pure Fe and Fe-X alloys were not significant, except for Fe-Mn whose corrosion rate was significantly lower than that of pure iron. However, dynamic immersion tests showed lower degradation rate of binary alloys than that of pure iron, again with Fe-Mn having the lowest one. Fe-C also had a higher dynamic degradation rate than that of as-rolled pure iron. The immersion test results showed that the degradation rates obtained by dynamic tests were higher than those obtained by static tests, and this was partially attributed to the solution flow washing some of the degradation products away. The authors suggested that using higher concentration of alloying elements may result in more significant effects on degradation rates of iron-based alloys. They referred to the work of Hermawan et al [93], wherein the degradation of Fe(20-35 Wt.%)Mn alloys were on average faster than that of pure iron approximately by a factor 2. Also, they suggested that having more than one alloying element, e.g. Fe-Mn-Pd system, may increase the corrosion rates by introducing more intermetallic phases, leading to microgalvanic corrosion. According to all of the corrosion tests, localized corrosion was the dominant mode of corrosion in both pure Fe and Fe-X alloys. Considering the mechanical and corrosion properties as well as the biocompatibility, Co, W, C and S elements were highlighted as good candidates to fabricate Fe-based biomaterials.

More recently, Capek et al. [94] investigated the degradation and mechanical behavior of binary Fe-2 wt% (Pd, Ag, C) prepared by powder metallurgy. Immersion test (pH=7.4, T=37 °C, 92 days, SBF) and potentiodynamic tests (T=37 °C, SBF) were employed. Immersion tests demonstrated that addition of Ag reduced the degradation rate while addition of C and Pd increased it. The authors suggested that the slower degradation of Fe-2%Ag alloy was due to the formation of silver chloride creating a barrier between silver, iron matrix and the

corrosive environment. Consequently, the microgalvanic corrosion would be inhibited. However, for Fe-2%Pd, they suggested that palladium chloride was not formed, but the iron chloride was formed. For, Fe-2%C the X-ray elemental maps did not show any connectivity between Cl and location of C particles. The effects of the elements in potentiodynamic tests were similar to those in immersion tests in terms of increasing or decreasing the degradation rate of pure iron. However, the differences between the potentiodynamic results were not as significant as those for immersion test. Also, unlike immersion tests, potentiodynamic tests suggested that Fe-2%C had a higher corrosion rate than Fe-2%Pd. The authors suggested that the results of the immersion tests are more valid as the test condition was closer to the real *in vivo* condition. The alloys demonstrated a lower elastic modulus, compressive yield stress and hardness than those of the pure irons. Higher porosity in the alloys was pointed out as a reason for this. The lower compressive yield stresses and elastic modulus values were also attributed to the “soft” alloying element particles and their low elastic modulus, respectively. Finally, under the sintering condition, Pd and C did not significantly diffuse with Fe, and no intermetallic phase was detected by X-ray elemental maps apart from thin diffusion layers containing Fe and Ag.

Apart from the alloying elements, manufacturing techniques can influence the corrosion behavior of iron-based metals differently. This is partially due to the different microstructures developed by different fabrication techniques. In reference [95], Moravej et al, compared the corrosion behavior of electroformed (E-Fe) and casted-and-thermomechanical-treated (CTT-Fe) irons via static and dynamic degradation tests in modified Hanks' solution (Ph=7.4, T= $37\pm 1^\circ\text{C}$, 336 hours). It was observed that E-Fes had significantly finer grains. Static immersion tests revealed that the degradation rate of E-Fe samples (0.4 mm/year) were around three times of that for CTT samples (0.14 mm/year). This was speculated to be caused by the finer grains and electrodeposition-induced structural defects of E-Fe samples. However, annealing of E-Fe samples reduced the degradation rate to 0.25 mm/year, and this was attributed to the reduction of defects densities as well as partial grain growth and release of stresses. Dynamic degradation tests showed higher iron ion release of E-Fe sample than that for CTT-Fe sample which was consistent with higher corrosion rates of E-Fe samples shown by static immersion tests. Also, annealing decreased the Fe-ion release of E-Fe

samples in the dynamic tests. The electroformed iron demonstrated a uniform corrosion mechanism.

1.3. Metal foams

Metal foams, which are a class of materials with cellular structure, are used in applications where altered material properties of the parent metal are beneficial [19]. They are used in various industries such as automotive, aeronautic, building, biomedical [96], and they have unique properties such as light weight, large surface area and energy absorbability [96]. As mentioned earlier, absorbable metal foams can be used for biodegradable orthopedic implants such as bone scaffolds. Certain properties of cellular materials depend on the relative density, i.e. ratio of the density of the cellular structure to that of the parent material, (and therefore porosity) and on the microstructure, e.g. the stiffness, strength, electrical and thermal conductivity and acoustic properties [97]. One should note that the stiffness (elastic modulus) of a cellular structure, e.g., iron foam, depends on the architecture of the structure to a great extent [97]. Therefore, it should not be confused with the elastic modulus of the cell wall material, e.g., iron. The mechanical properties of metal foams “most directly” [98] depend on the relative density and the mechanical properties of the parent metal. However, structural properties such as pore sizes, cell types, strut shapes etc. also influence the mechanical properties of the foams [98].

1.4. Basic fabrication techniques of metal foams

A cellular structure has a relative density of less than ~ 0.3 [99]; structures with higher relative densities are considered as solids that contain “isolated pores” [99]. Basic fabrication methods of cellular metals are shown in Figure 1.1 (Adapted from [97]). The manufacturing methods of the cellular metals determines their structure, and each method is suitable for certain parent metals. The important differences between these methods are: the metal state during developing the pores (liquid, solution, solid, etc.), metal forming technique (casting, deposition, foaming, sintering, etc.) and the pore formation technique (whether it uses a hollow or removable substrate or a gas) [97].

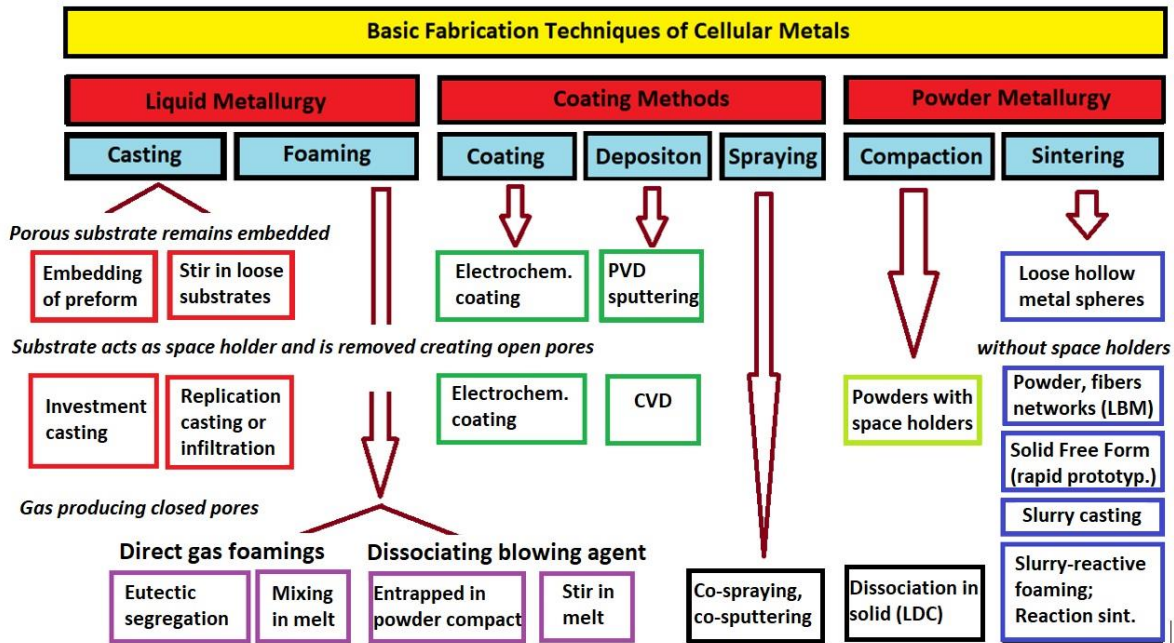


Figure 1.1- Basic fabrication techniques of cellular metals (adapted from [97])

Powder metallurgy techniques are among the common techniques to produce metal foams [30, 100]. Two popular powder metallurgy methods for fabrication of open cell metal foams are space holder and replication techniques. In the space holder technique, powders of the metal get mixed with the particles of a space holder material, and the mixture undergoes uniaxial, isostatic or injection molding compaction [101]. Some of the space holder materials that have been used are: “carbamide ($\text{CO}(\text{NH}_2)_2$), ammonium hydrogen carbonate (NH_4HCO_3), sodium chloride (NaCl), starch, saccharose, polymethyl-methacrylate (PMMA)” [101]. To create the pores, the space holder particles would be removed by either a heat treatment process (decomposition and evaporation) or leaching (dissolution in a liquid) [101]. This is followed by high-temperature sintering to form an open pore metal foam with suitable integrity. Removing a large quantity of the space holder material is an existing challenge for this method. Porosities of 60-80% could be produced with this method [17]. Many researchers have used this method to fabricate metallic scaffolds [83, 101]. Figure 1.2a (adapted from [102]) shows a schematic representation of a space holder process. Capek et al. [83] studied the effect of initial powder size and the compacting pressure on the microstructure and mechanical properties of the iron foam samples. They realized that using finer initial iron powders and higher compacting pressure led to higher compressive elastic

modulus and yield stress. Also, higher compact pressure, unlike using finer initial powders, decreased the “microporosity”. However, using finer initial powders resulted in smaller “micropores” and more spherical “macropores”.

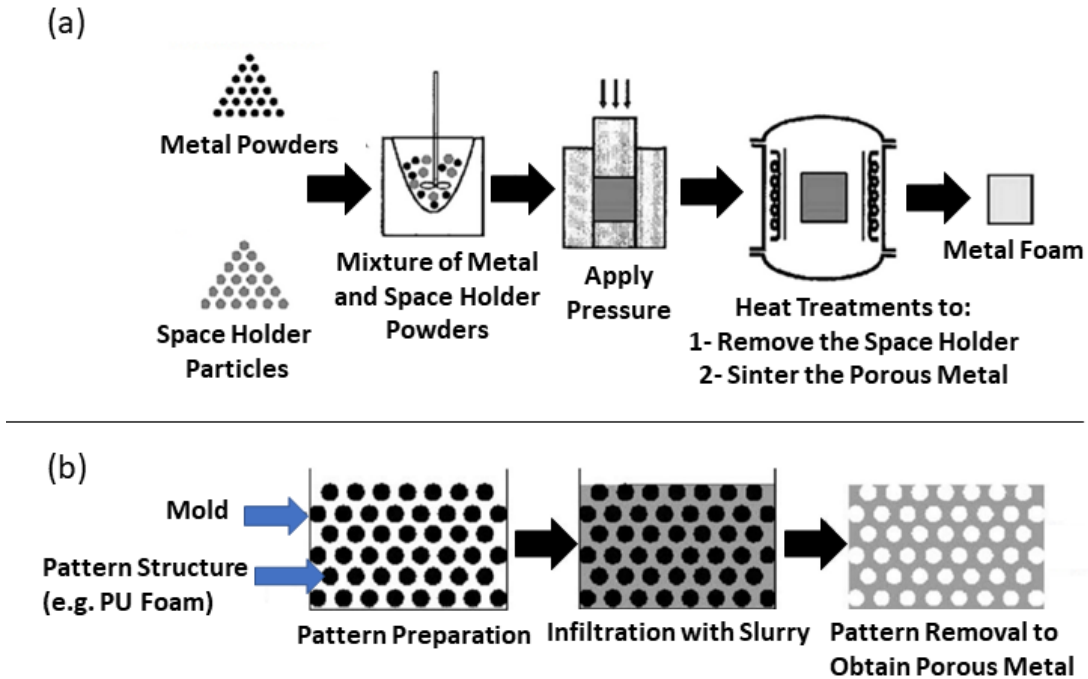


Figure 1.2- Schematic representation of a) space holder b) replication techniques to fabricate porous metals (adapted from [102] and [17])

In replication method, a pattern structure is impregnated with a slurry that contains the metal powders and binders. The pattern structure, e.g. PU foam, along with the binders are then thermally removed, and, after sintering the remained metal structure with hollow struts (the green foam), a metal foam is obtained [17]. In the initial steps, care must be taken so that all the struts of the pattern foam, e.g. PU foam, are fully coated with the slurry, yet the slurry should not close the pores (windows) of the open cells in the pattern foam [103, 104]. Figure 1.2b (adapted from [17]) displays the main three steps of the replication approach to fabricate the metal foams.

Replication of a pattern foam can also be conducted by electroplating. The open-cell iron foams used in the present research (manufactured by Alantum [42]) are fabricated by this technique. Polyurethane (PU) foams are used as the precursor (the pattern structure). Pure

iron is then electroplated from an acidic bath that contains Fe(II) salts on the pattern foam which has become conductive by a thin layer of sputtered nickel. In the following steps, the PU foam is removed (pyrolyzed) at ~ 560 °C and the remaining structure is annealed at ~ 950 °C, producing iron foams with hollow struts (Figure 1.3) [42].

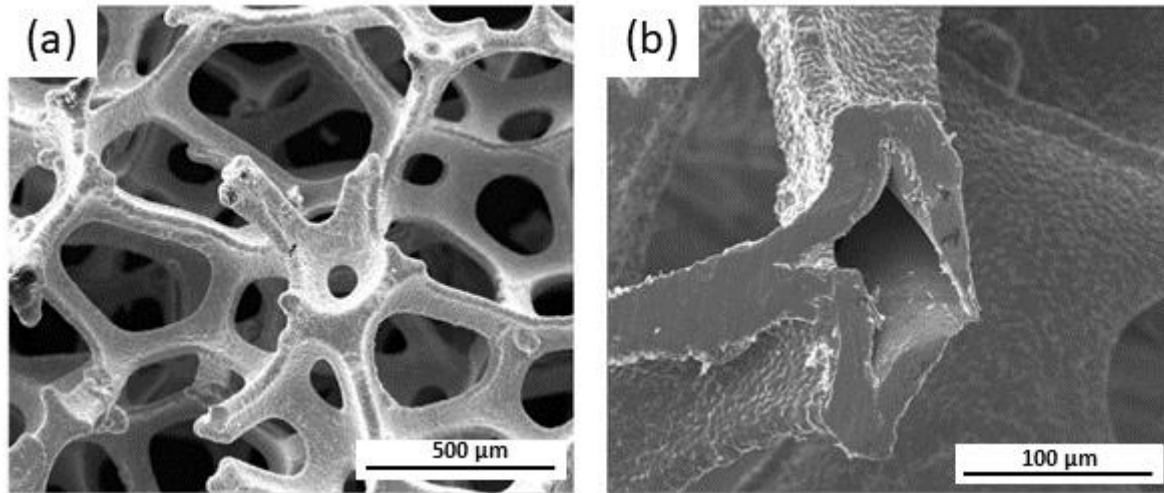


Figure 1.3- a) Alantum open-cell iron foam structure, b) Hollow strut

1.5. Fabrication of biodegradable porous metals

Biodegradable metallic scaffolds have been manufactured through various techniques. Space holder, replication and additive manufacturing are among the extensively used techniques.

Mg-Zn scaffolds were fabricated by Mg-6wt.%Zn powders and $\text{CO}(\text{NH}_2)_2$ particles as space holder [105]. Before mixing the space holder particles with Mg-Zn composite powders, the pure Mg and Zn powders were mixed, dried and remixed in a planter ball-mill (argon atmosphere). The fabrication steps of the scaffolds are shown in Figure 1.4 (adapted from [105]). The Mg-Zn scaffolds were also loaded with an antibiotic (Tetracycline) solution in different concentrations to study their drug-delivery and antibacterial characteristics [105].

Some researchers have combined space holder and infiltration approaches to fabricate biodegradable porous metals. Mg alloy (AZ31) foams [106] were fabricated by infiltrating

liquid AZ31 (under vacuum) into NaCl space holder particles. The space holders were removed in ultrasonic bath of deionized water (dissolution approach). The surface of the foams was treated by micro-arc oxidation (MAO) coating. Air-pressure infiltration was used to fabricate Zn [107] and Zn-1wt.%Al [37] scaffolds with NaCl particles as space holder. In this method, the pressured air is applied quickly after the molten metal is cast into the space-holder-containing mold [107]. Figure 1.5 (adapted from [107]) shows an schematic of the air-pressure infiltration apparatus along with a Zn scaffold structure after space holder removal.

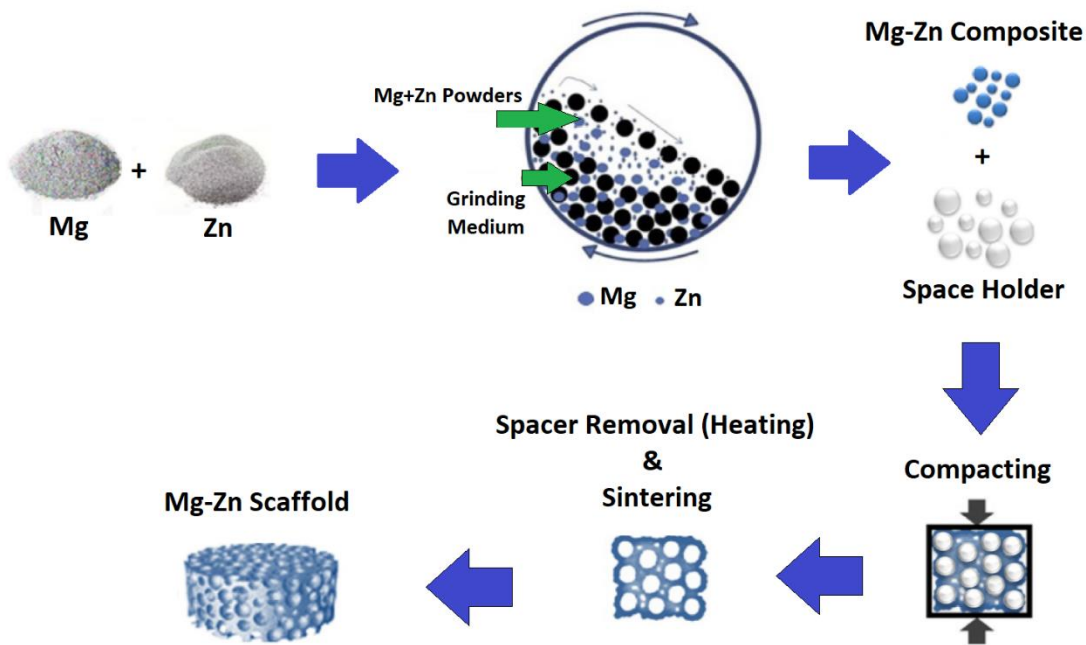


Figure 1.4- Fabrication of an Mg-Zn scaffold with space holder technique (adapted from [105])

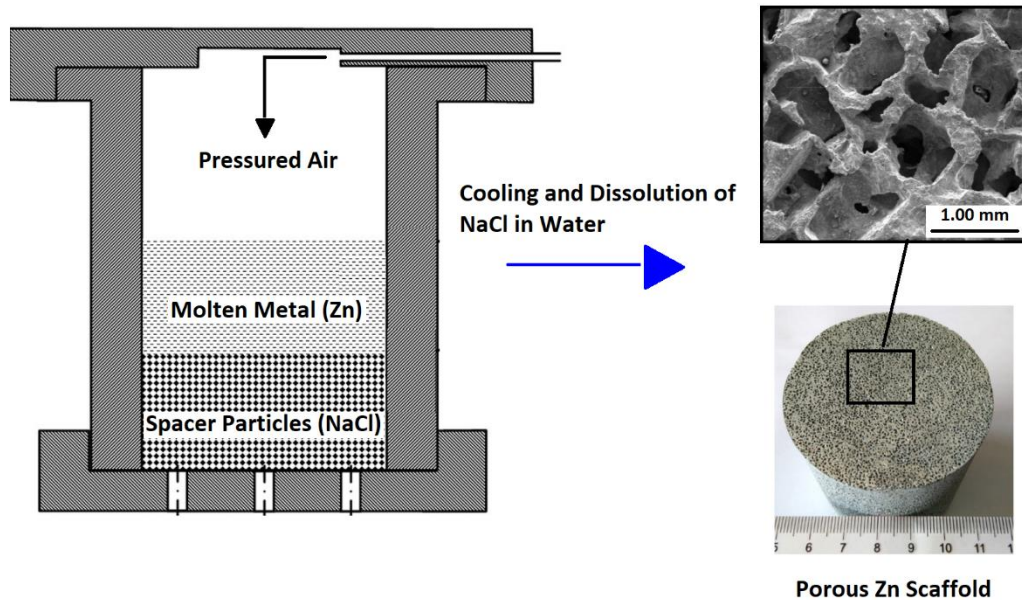


Figure 1.5- Fabrication of a porous metal scaffold with air-pressure infiltration combined with space holder methods (adapted from [107])

Researchers have also manufactured biodegradable metal foams by replication of PU foams through impregnation. Fe foams [108, 109] were fabricated by impregnation of polyurethane (PU) foams with Fe-powder-containing slurries. To produce Fe foams, the impregnated PU foams underwent heat treatment (for PU foam removal), and then the Fe structures were sintered. Fe-Mn alloys [110] were fabricated by impregnating PU foams with $\text{Fe}_{47}\text{Mn}_{53}$ -powder-containing slurry. The impregnation was followed by different heat treatment procedures (to dry the impregnated foam and then to remove the PU/additives) and sintering at different temperatures which led to obtain alloys with different levels of Mn content. Alternatively, another replication technique was used to fabricate Mg-based scaffolds with MgF_2 coatings [26]: the technique incorporated the infiltration of melted Mg-based ingots into a porous Ti template followed by leaching out the template by immersing the green body in 40% hydrofluoric (HF) acid.

In another approach, cavity moulds are first produced by eliminating a 3D-printed sacrificial pattern structure embedded in the mould material, then they are filled with metal powder (followed by sintering) or molten metal to create the metal scaffold. Topologically ordered porous Fe was fabricated by this technique [111]: first, a sacrificial polymer pattern was 3D

printed and incorporated into a mould (mixture of a phosphate-based investment powder and hardener); then, the sacrificial pattern burnt out to create cavities which were filled with carbonyl iron powders. The powders then underwent pressureless microwave sintering to produce the scaffolds. The process is explained in Figure 1.6 (Adapted from [112]). Similarly, Zn scaffolds [35] were fabricated by casting the molten Zn into the mould (NaCl) produced by burning out a 3D printed polymeric pattern embedded in the salt mould; the salt mould was dissolved in a water bath after casting.

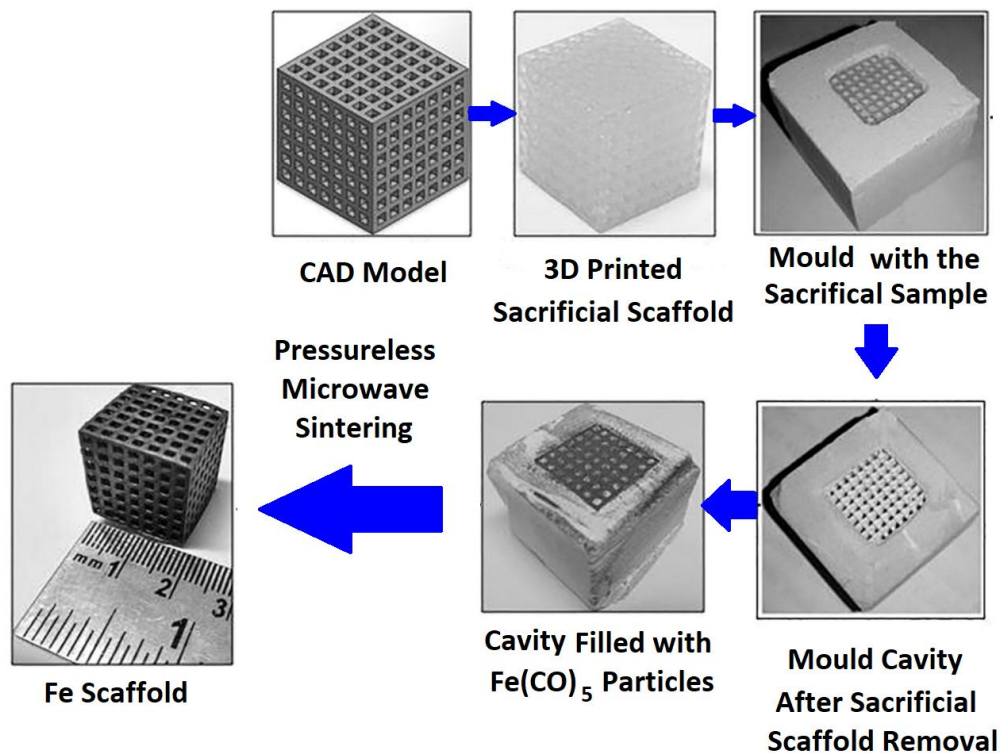


Figure 1.6- Fabrication of Fe scaffolds using 3D-printed sacrificial structure and pressureless microwave sintering (adapted from [112])

Researchers have also employed additive manufacturing (AM) techniques to produce biodegradable metal scaffold. The input material in AM of metal could be either in powder or wire form, and the energy source could be either laser or electron beam/arc [113]. One of the main classes of metal additive manufacturing techniques is powder bed fusion (PBF) in which metal powders are “selectively” [113] and layer by layer fused (e.g. sintered or melted by laser beam, melted by electron beam) in a powder bed [113]. As far as biodegradable

metal scaffolds are concerned, PBF has been employed to fabricate porous Fe [23, 24, 82], Zn [15, 33, 114] and Mg-based [29, 115] scaffolds.

Some AM techniques such as solvent-cast 3D printing (SC-3DP) and Inkjet 3D printing incorporate the use of binders which would be finally removed, and the remained metal structure (green) get sintered to bond the metal powders. Solvent-cast 3D printing (SC-3DP) and Inkjet 3D printing have been used to manufacture Mg [116] and Fe-30Mn (wt.%) [117] scaffolds, respectively.

1.6. Mechanical and corrosion properties of biodegradable porous metals

Biodegradable porous metals have been studied as potential tissue scaffolds. Researchers have studied Mg, Fe, and Zn- based porous metals [20, 21, 32, 34]. Cheng et al. [32] investigated the corrosion and mechanical behavior of MgF₂ coated open-porous magnesium (two different nominal pore diameters of 250 μm and 400 μm but similar porosity of ~55%) as cancellous bone scaffolds. The scaffolds were fabricated using entangled Ti wires as space holder. They observed that samples with larger pore size demonstrated slightly higher mechanical properties (average Young's modulus of 2.37 GPa VS. 2.18 GPa and average compressive strength of 46.3 MPa VS. 41.2 MPa) which was attributed to the larger strut thicknesses in the 400 μm pore-size scaffold, (i.e. 0.36 mm VS. 0.28 mm). However, the difference between the values of the mechanical properties did not seem to be significant. As for the corrosion behavior, both samples showed a similar amount of Mg ion concentration until the 7th day of immersion (in Dulbecco's modified Eagle's medium that contained 10% fetal bovine serum at 37 °C, 14 days of immersion, corrosion products were removed after immersion at different removal intervals for mass-loss measurements), however, the ion concentration for the 400 μm pore-size scaffold between 7 and 14 days of immersion was higher than that of the other sample, indicating its faster degradation. The corrosion rate of the sample with larger pore size after two weeks of immersion was 1.53±0.15 mm/year while that of the sample with the smaller pore size was 1.31±0.11 mm/year. The MgF₂ coating slowed down the degradation initially and limited the release of hydrogen gas which takes

place in corrosion of Mg. They also observed that the 400 μm pore-size scaffold better promoted the formation of new bone which was partially attributed to the higher vascularization induced by larger pores.

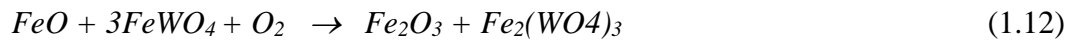
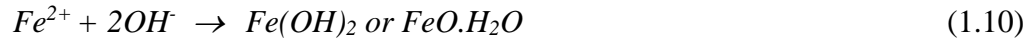
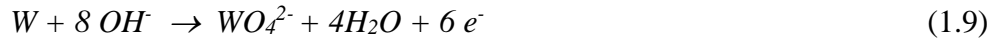
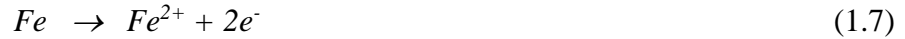
In a another study [20], degradation and mechanical behavior of Fe and Fe-P foams were investigated. The Fe-P alloys were fabricated (coated) either by phosphated carbonyl iron powder (Fe-P(I)) or by a mix of carbonyl iron and Fe_3P (Fe-P(II)), and the foams were fabricated by the replication of polyurethane (PU) foams. The total porosity of the Fe, Fe-P(I) and Fe-P(II) samples were 89%, 88%, and 89%, respectively. The closed porosity of Fe, Fe-P(I) and Fe-P(II) samples were 5%, 7%, and 5%, respectively. Potentiodynamic polarization was employed to understand the degradation behavior of the samples ($T= 37\pm 1$ °C). Hanks' solution with pH of 7.4 as well as physiological saline solution (0.9% NaCl) with a pH of 5.9 were used. It was observed that porous pure iron and Fe-P(I) samples had the highest (0.44 mm/year) and the lowest (0.27 mm/year) corrosion rate in Hanks' solution, respectively. The order of the degradation rates in saline solution was the same as that in Hanks' solution, although all the samples showed a higher degradation rate in the saline solution (almost 2 times as high). The authors attributed the slower degradation in Hanks' solution to the presence Ca and P precipitates, resisting against the degradation process. It was realized that the phosphorous iron foams were more corrosion resistant than pure iron ones. It was also observed that the addition of phosphorous increased the hardness of the foams. Fe-P(II) samples showed the highest average compressive yield stress (2.1 MPa), elastic modulus (22.4 MPa) and hardness values (278 HV 0.01). Fe-P(I) foams demonstrated the highest steep plateau; the authors speculated that it was due to the highest ratio of "closed-to-total porosity" in Fe-P(I) foams.

He et al. [21] studied the mechanical and corrosion properties of double-layer porous Fe/Fe-W alloy scaffolds fabricated by electroplating of pure iron on a PU foam followed by deposition of Fe-W on the pure iron. There were four types of samples with different molar ratios of Fe and W in Fe-W alloy, in addition to the pure Fe control sample. Immersion tests (Hanks' solution, $T=37$ °C) was conducted for 3, 15 and 30 days. After removal, samples were rinsed with distilled water and dried under vacuum for 10 hours at 60°C. After SEM, EDS and XRD characterizations, corrosion products were removed for corrosion rate

calculations (mass-loss technique). It was observed that all samples had the highest corrosion rate after 3 days of immersion which significantly decreased after 15 and 30 days of immersion. However, the double layer samples generally tended to have lower corrosion rates than that of pure irons after 3 and 15 days of immersion. After 30 days of immersion, 1.5FeW had the highest average corrosion rate (0.264 g/m².d) followed by pure Fe (0.230 g/m².d); Fe1.5W however had the lowest average corrosion rate (0.149 g/m².d) after 30 days. The proposed degradation mechanism of the alloy in static immersion was as follows:

- 1- Oxidation and reduction reactions (Eq. 1.7-1.9).
- 2- Degradation products formation (Eq. 1.10-1.12).
- 3- Accumulation of the corrosion products, making corrosion product layers.

Presence of the layers slows down the degradation rate. However, a crack would appear later, exposing the underneath intact surface to corrosion.



The tensile tests results showed that the strength of the pure Fe and the alloy scaffolds, depending on the electrodeposition time of the substrate (pure iron), was either close or within the range of the cancellous bone strength. Average tensile strength of the pure Fe scaffold sample (electrodeposition time: 2 hours) was 3.32 MPa, and that of the Fe/Fe-w alloy scaffolds with 1 hour and 2 hours electrodeposition times was 1.18 MPa and 4.01 MPa, respectively. The alloy scaffold with the higher tensile strength had a higher average apparent density (0.881 g/cm³) than the other one (0.466 g/cm³). This highlights the importance of electrodeposition parameters on the final mechanical properties.

1.7. Corrosion-time dependent mechanical properties of biodegradable porous metals

As mentioned in the previous sections, biodegradable scaffolds must retain their mechanical integrity during corrosion to avoid premature failure. Therefore, some researchers have studied the various factors influencing the mechanical behavior in the course of corrosion. However, the number of such research works are limited. The researchers have mostly evaluated the corrosion-time dependent compressive elastic modulus (quasi-elastic gradient) as well as compressive yield stress of the open-cell metal foams or lattices as bone scaffolds.

In recent years, several studies have been conducted on corrosion-time dependent mechanical properties of additively manufactured (AM) biodegradable porous metals. In a study [23], topologically ordered absorbable iron scaffolds were manufactured by direct metal printing (DMP). The nominal strut thickness was 200 μm , yet, after manufacturing, the struts turned out to be approximately 50 μm thicker than the design values. Static immersion tests *in vitro* were conducted (in a stirred thermostatic bath) in revised simulated body fluid (r-SBF) at 37°C for different periods (i.e. 1, 2, 7, 14 and 28 days), and samples were ultrasonically cleaned afterwards to measure weight changes. Compression tests were conducted on the corroded (uncleaned), as-built and as-polished samples.

After 28 days of immersion, a weight loss of 3.1% was observed in the scaffolds and the solution pH increased from 7.4 to 7.8. One of the reasons for such a small weight loss was the presence of adherent corrosion products after cleaning.

Compression tests on the corroded samples showed that after 1 day of immersion, the elastic modulus decreased. This was followed by an increase, yet from the 2nd to the 14th day of immersion, it did not significantly change (Figure 1.7a, adapted from [23]). However, it again significantly reduced after 28 days of immersion (Figure 1.7a). On the other hand, a general decreasing trend of the yield stress was observed from 23.7 MPa to 22.4 MPa after 28 days of immersion (Figure 1.7a). It appeared that the corrosion products contributed to carrying the load at small strains, thus maintaining the elastic modulus after corrosion. However, at

higher strains, the bonding between the corrosion product and the intact iron was not as strong, resulting in reduction of the yield stress with immersion time. Similarly, in reference [28], as compared to plateau stress and energy absorbability, elastic modulus of the corroded porous AZ63 (up to 24 hours of static immersion in phosphate buffered saline) was more influenced by the presence of corrosion products, i.e. after 24 hours of immersion, the elastic modulus did not significantly reduce, unlike the plateau stress and energy absorbability.

In reference [23], faster corrosion was observed in the periphery regions of the scaffolds. After 28 days of immersion, the struts at the center were almost intact. This difference between the corrosion of periphery and the central regions of the scaffolds was attributed to a few possible factors: 1- difference in local pH values of the central and peripheral regions, 2- stagnant flow of the solution at the center, 3- limiting the diffusion process by peripheral corrosion products acting as a barrier, 4- stabilized passive layers on the central struts.

In reference [29], topologically ordered absorbable porous magnesium (WE43) scaffolds were fabricated by selective laser melting (SLM). Static immersion tests were carried out in a custom-made set-up that was put into a thermal bath at 37°C. Also, r-SBF with 5% fetal bovine serum (FBS) was used as the solution, and the immersion periods were 1, 2, 7, 14 and 28 days. In the first 3 hours of immersion, the pH value in the vicinity of the scaffold initially increased from 7.4 to 8.1, then decreased to 7.7. During this time, the pH far from the scaffolds remained around 7.4-7.5. In the longer periods up to 28 days, pH values tended to increase with immersion time with near-scaffold pH being higher than that in the farther region. At its maximum value, the near-scaffold pH reached to around 7.9.

The measured average strut thickness and porosity were $420 \pm 4 \mu\text{m}$ and $64\% \pm 0.2\%$, respectively. μCT analysis revealed that a significant amount of corrosion products was formed in the central regions of the samples, as opposed to what was observed in the peripheral regions. The scaffolds lost around 20% of volume after 28 days of immersion. According to μCT and SEM analyses, local and uniform corrosion took place in the center and at the periphery, respectively.

The elastic modulus increased after 1 day and 2 days of immersion; it suddenly decreased after 7 days and did not significantly change thereafter (Figure 1.7b, adapted from [29]). The yield strength on the other hand slightly decreased from 22 MPa to 20 MPa after 14 days of immersion; this was followed by a significant reduction to 13 MPa after 28 days of immersion (Figure 1.7b). Again, the effect of the presence of corrosion products on elastic modulus and yield strength was different, and it was attributed to the different bonding status between the products and the intact metal at small and large compressive strains. The drop of the elastic modulus at day 7 was attributed to the local corrosions at the center which resulted in increase of stress concentrations at highly corroded struts.

In another study [33] topologically ordered absorbable zinc scaffolds were manufactured by powder bed fusion technique. Static and dynamic immersion tests were carried out (20% O₂, 5% CO₂, 37°C, 0.3 ml/min flow rate for dynamic immersion) in r-SBF and for 1, 2, 7, 14 and 28 days. The struts were ~41 μm thicker than the design value which was 400 μm. For static condition, pH values stayed around 7.5-7.6 after all immersion periods. For dynamic condition, the pH was stable around 7.5-7.6 until after 14 days of immersion, yet it increased to 7.7 after 28 days.

The yield strength of the samples corroded in dynamic immersions gradually increased from 2-day to 28-day immersion (Figure 1.7c, adapted from [33]). Significant variation of yield strength was not observed among the specimens corroded under static corrosion, yet the corroded specimens generally tended to have higher yield strengths than that of the as-built specimens (Figure 1.7c). The elastic modulus of samples increased after 1 day of static and dynamic immersion, and it was followed by a decrease for the 2-day immersed samples. For statically immersed samples, after 2 days of immersion, the modulus followed a generally decreasing trend until 28 days of immersion. Such a trend was not observed for the dynamically immersed samples (Figure 1.7c). The 28-day dynamically immersed sample had a higher elastic modulus than the as-built sample, i.e. 879.3 MPa VS. 785.7 MPa. The maintained/enhanced mechanical properties of the dynamically corroded samples was attributed to the presence of large volumes of corrosion products.

As compared to static immersion, the dynamic immersion led to more homogeneous corrosion, and it generated greater volume of corrosion products, i.e. $104 \pm 9 \text{ mm}^3$ VS. $59 \pm 8 \text{ mm}^3$. Saad et al. [31], also used dynamic immersion tests to study the variation of compressive properties of porous pure Mg samples with different porosities. The degradation tests were carried out using a simulated body fluid prepared based on reference [118], ($T=37 \pm 1 \text{ }^\circ\text{C}$, adjusted $\text{pH}=7.4$), and the flow rate was maintained at 0.025 ml/min , respectively. The immersion time intervals were 24, 48 and 72 hours. The corrosion products were removed after immersion. Figure 1.8 and 1.9 (both adapted from [31]) demonstrate the corroded porous Mg samples (before and after cleaning) as well as the variation of mechanical properties with immersion time. It was observed that all the measured compressive properties, i.e. compressive strength, yield stress and elastic modulus, decreased after immersion. Comparing with the static immersion results reported in the literature, the authors stated that the mechanical degradation of porous Mg under dynamic immersion was higher than that under static immersion tests (maximum 89% of decrease in the strength after 3 days of dynamic immersion). The corrosion rates under dynamic condition were higher than the previously reported results under static condition ($4.9\text{-}7 \text{ mm/year}$ VS. $0.4\text{-}1.53 \text{ mm/year}$), and trivial pH changes in the solution was observed (up to ± 0.4).

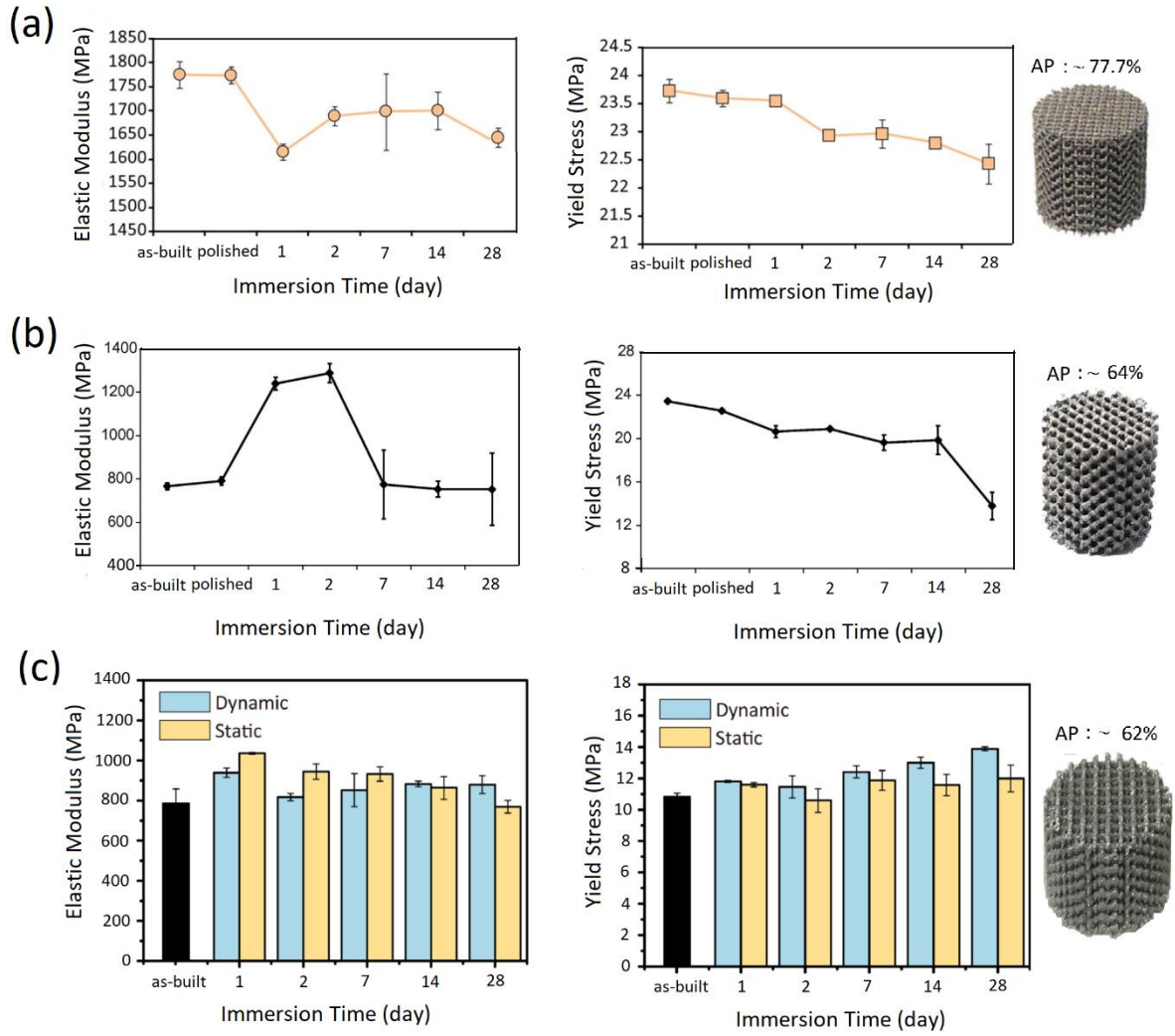


Figure 1.7- Corrosion-time dependent mechanical properties of AM porous a) Fe, b) Mg alloy, c) Zn, AP: as-built porosity from μ CT measurements (adapted from [23, 29, 33])



















Immersion Time (hours)	Initial Porosity: 30%	Initial Porosity: 41%	Initial Porosity: 55%
	Before Cleaning After Cleaning	Before Cleaning After Cleaning	Before Cleaning After Cleaning
24	 	 	 
48	 	 	 
72	 	 	 

Figure 1.8- Corroded porous Mg samples (before and after cleaning) after different immersion times (adapted from [31])

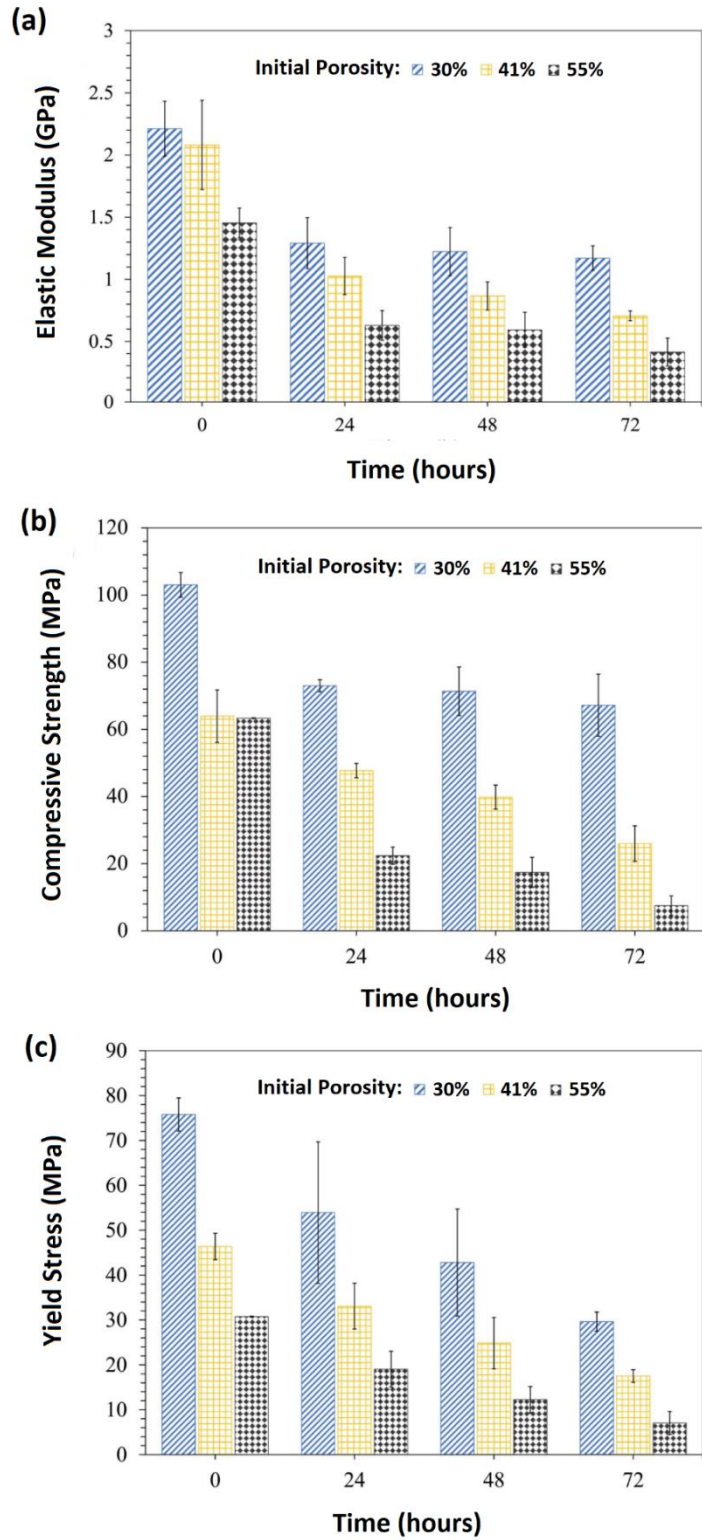


Figure 1.9- Variation of mechanical properties of porous Mg with dynamic immersion time (adapted from [31])

1.8. Effect of graded structures on corrosion and corrosion time-dependent mechanical properties of biodegradable metal scaffolds

Unlike uniform porous structures, the architectural parameters, e.g. strut thickness and pore size, vary within the functionally graded porous materials. Depending on the application, the graded structure can provide certain design advantages over the implants with uniform structures [15, 119], e.g. inhomogeneous elastic properties within the implant structure [120]. Functionally graded biodegradable scaffolds provide a possibility to concurrently tailor multiple properties, e.g. mechanical, corrosion and permeability, according to specific design requirements [15]. Although research on functionally graded absorbable metal scaffolds is still limited, with advancing additive manufacturing techniques, there exists a great potential for development of such biomaterials.

In a study [24], functionally graded absorbable porous irons were manufactured by selective laser melting (SLM). 4 groups of porous structure including 2 functionally graded and 2 uniform structures (0.2 mm and 0.4 mm nominal strut thickness, represented as Uniform-0.2 and Uniform-0.4, respectively) were developed (diamond unit cell) (Figure 1.10a, adapted from [24]), and their mechanical properties, permeability, degradation behavior and cytocompatibility were compared against each other. One of the functionally graded structures had a nominal strut thickness of 0.4 mm and 0.2 mm in the periphery and the center, respectively (Dense-out); the other had a nominal strut thickness of 0.2 mm and 0.4 mm in the periphery and the center, respectively (Dense-in) (Figure 1.10a). The strut features in the functionally graded structures varied gradually to minimize the stress discontinuities. After fabrication, the struts of samples turned out to be approximately 50 μm thicker than the design values.

Dynamic immersion tests *in vitro* were conducted (for 28 days) in a pre-equilibrated (20% O₂, 5% CO₂, 37°C) r-SBF, and they were followed by sample cleanings and weight loss measurements. Compression tests were conducted, and the stress distributions were studied using finite element analysis (FEA).

Permeability of samples from the highest to the lowest values were as follows: Uniform-0.2, Uniform-0.4, Dense-out and Dense-in. Permeability is highly affected by porosity and its distribution, so it was expected for Uniform-0.2 sample to have the highest permeability level. However, despite the similar porosity, the Dense-in sample demonstrated a lower permeability than that of the Dense-out sample which was attributed to the difference between the topology of the structures. CFD analysis showed that higher porosity regions of the functionally graded specimens experienced a higher flow velocity.

After 28 days of dynamic immersion, the solution pH slightly increased from 7.5 to approximately 7.6. The Uniform-0.2 and Uniform-0.4 experienced the highest and the lowest weight loss, respectively ($16.7 \pm 3.3\%$ Vs. $5.1 \pm 0.9\%$). The weight loss values of the functionally graded samples fell between those of the Uniform samples with Dense-out sample having a slightly higher value than that of Dense-in sample ($10.3 \pm 0.3\%$ Vs. $8.9 \pm 0.4\%$). Corrosion took place in both periphery and core regions of the samples due to the dynamic flow. The results suggested that the topology affect the degradation behavior of the porous structure by influencing the permeability and the flow velocity. For example, despite having identical geometries at the center, the central weight loss of the Dense-out sample was higher than that of the Uniform-0.2. The permeability of the Uniform-0.2 sample was higher than that of the Dense-out one. However, CFD analysis showed that the central flow velocity of the Dense-out sample should be higher than that of the Uniform-0.2 one, thus explaining the discrepancy.

Compression test results showed that the Uniform-0.4 and Uniform-0.2 samples possessed the highest and lowest values of mechanical properties (elastic modulus and yield stress), respectively (Table 1.1). The elastic modulus and the yield strength of the Dense-in sample were somewhat higher than those of the Dense-out one, despite similar porosities (Table 1.1). This was attributed to the difference in the distribution of the thicker struts and its influence on the load carrying capacity of the structures. The elastic modulus and yield strength of all the samples tended to decrease after 28 days of immersion.

Table 1.1- The porosity and mechanical properties of the samples in reference [24]

Sample design-nominal strut thickness in mm	Porosity (μ CT) %	Elastic modulus (MPa)	Yield strength (MPa)
Uniform-0.2	84.8 ± 0.1	891.6 ± 89.7	10.7 ± 0.4
Uniform-0.4	58.4 ± 2.0	2815.9 ± 126.6	53.1 ± 0.9
Functionally graded-Dense- in	70.6 ± 0.4	1767.3 ± 48.5	32.9 ± 1.6
Functionally graded-Dense- out	71.0 ± 0.2	1754.4 ± 30.8	30.5 ± 0.3

In a more recent study [15], a group of functionally graded and 2 groups of uniformly structured porous zinc were manufactured by a powder bed fusion (PBF) technique. The nominal strut thickness of the uniform structures was 0.3 mm (Uniform-0.3) and 0.4 mm (Uniform-0.4) while that of the functionally graded structure changed radially and linearly from 0.4 mm to 0.2 mm (FG-0.4-0.2), i.e. Dense-out. After manufacturing, the struts turned out to be 40-50 μ m thicker than the designed values. The porosity of the functionally graded structure was between that of the other 2 groups. The nominal porosity for the uniform structures was 81.1% and 67.4% while that of the functionally graded structure was 74.3%. The nominal porosity at the periphery regions of the functionally graded structure was around 67% while at the core region it increased to near 91%. Static and dynamic immersion tests were conducted (up to 28 days) in r-SBF under cell-culture conditions (20% O₂, 5% CO₂, 37°C). Pre-equilibrated solution with a flow rate of 0.3 ml/min was used for the dynamic test.

The highest increase of solution pH value happened after 28 days of immersion in a dynamic immersion test (from 7.5 to 7.9). The compressive elastic modulus and yield strength of the as-built functionally graded sample fell between those of the as-built uniformly structured samples, but closer to those of the Uniform-0.3 sample (Figure 1.11, adapted from [15]). This was the case for permeability as well. As compared to static immersion results, dynamic tests resulted in greater volumes of corrosion products (approximately 200% of volumes in the static tests, Figure 1.10b, adapted from [15]), and less localized corrosion. Dynamic immersion tended to result in higher degradation rates as well. Under dynamic condition, the

functionally graded structure experienced more degradation in the center than in periphery region; it was attributed to the higher flow velocity in the central region. However, static tests resulted in higher degradation in periphery region of the specimens (Figure 1.10b). After 1 day of static and dynamic immersion, the elastic modulus and the yield strength of all samples increased (Figure 1.11). After 28 days of dynamic immersion, the elastic modulus of the uniform structure sample with 0.4 mm strut thickness and that of the functionally graded sample did not drop; their yield strength however increased (Figure 1.11). After different immersion periods, samples under dynamic condition tended to have higher yield strengths, as compared with those under static condition (Figure 1.11). This was attributed to the stronger presence of corrosion products caused by dynamic degradation (Figure 1.10b), improving the strength of the porous structure. This study showed that functionally graded design of porous structure can significantly affect the corrosion-induced mechanical behavior of an absorbable scaffold by tailoring the permeability and thus the degradation rate.

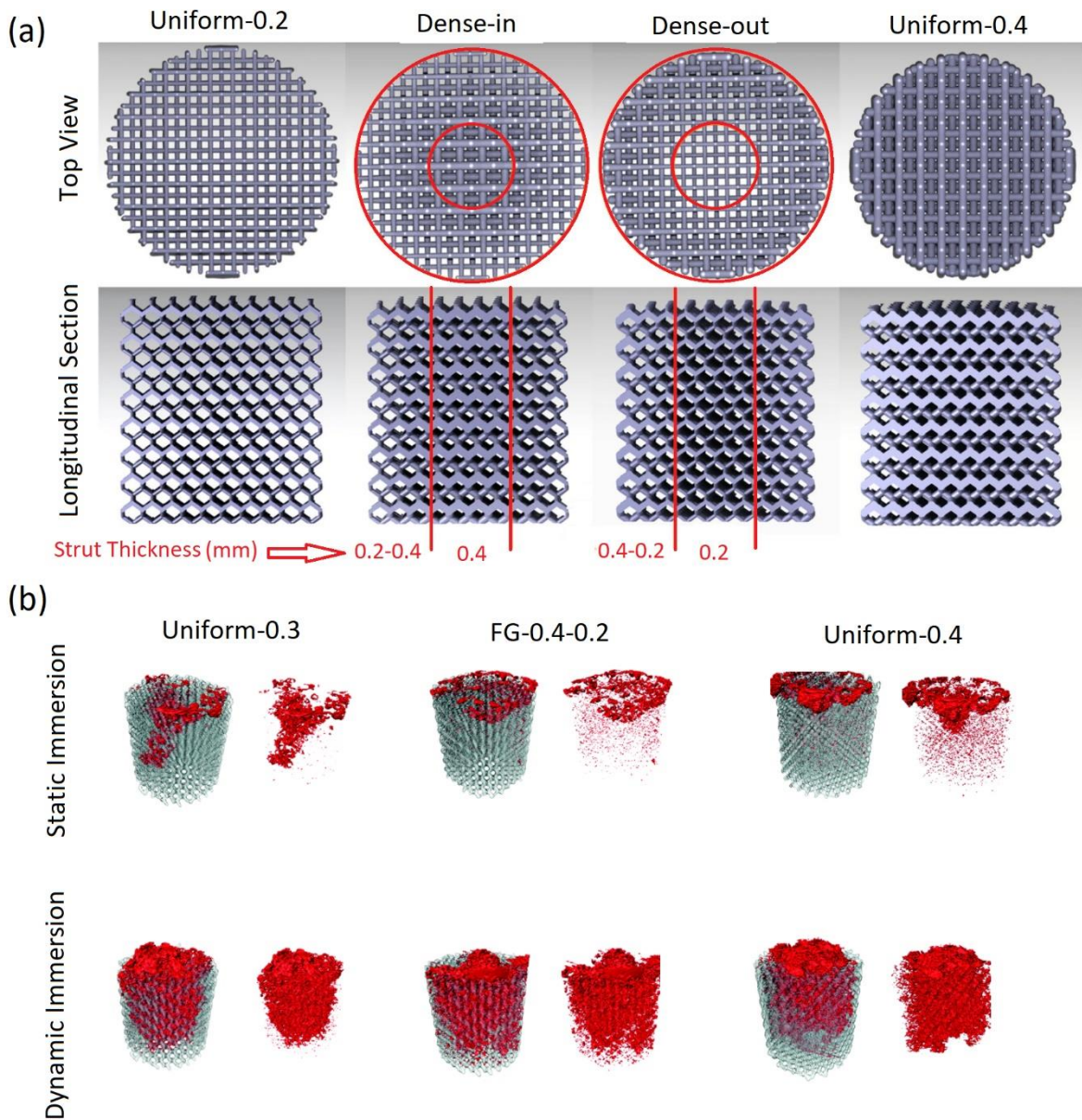


Figure 1.10- a) Topology of additively manufactured (AM) biodegradable porous iron with uniform and functionally graded structures, b) 3D reconstruction (μ CT) of 28-day corroded AM biodegradable porous zinc specimens (gray) and their corrosion products (red). (adapted from [15, 24])

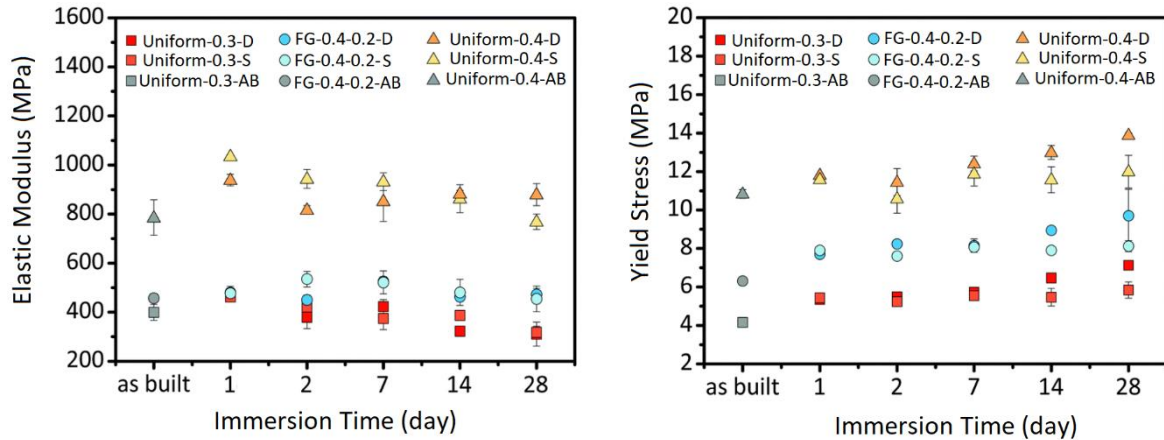


Figure 1.11- Corrosion-time dependent mechanical properties of biodegradable porous zinc with uniform and functionally graded structures. D: dynamic immersion, S: static immersion, AB: as-built. (adapted from [15])

1.9. Modeling approaches to study the mechanical behavior of metal foams

There are two general approaches to model the foams structure and study their mechanical behavior : Analytical and Finite Element (FE) modeling [121].

1.9.1. Analytical modeling

The most well-known analytical models to predict the mechanical properties of the foams have been presented by Ashby and Gibson [99, 122]. In their models, the elastic modulus and plastic collapse stress of the foams were expressed as functions of relative density. They used a cubic model (Figure 1.12, Adapted from [99]) to derive the analytical relationships for the open cell foams with the assumption that the dominant deformation mechanism is bending of the struts; this is the case when the relative density ≤ 0.1 [99].

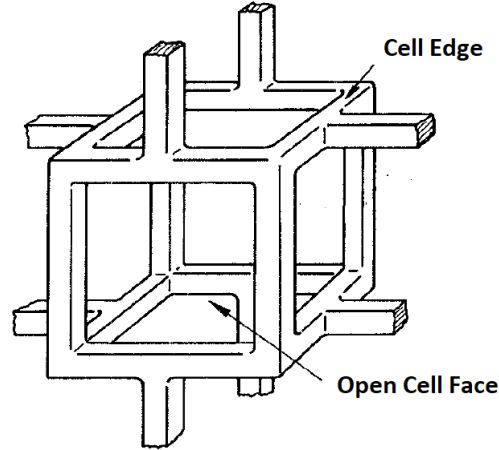


Figure 1.12- The cubic open cell model used by Ashby and Gibson (adapted from [99])

For the open cell foams, which are the focus of this study, the following equations are proposed by Ashby and Gibson:

$$\frac{\bar{E}}{E_s} = C_1 \left(\frac{\bar{\rho}}{\rho_s} \right)^2 \quad (1.13)$$

$$\frac{\bar{\sigma}_{pl}}{\sigma_{ys}} = C_2 \left(\frac{\bar{\rho}}{\rho_s} \right)^{\frac{3}{2}} \quad (1.14)$$

Wherein \bar{E} and E_s are elastic modulus of the foam and the parent material, respectively; $\bar{\rho}$ and ρ_s are the density of the foam and that of the parent material, respectively; $\bar{\sigma}_{pl}$ and σ_{ys} are plastic collapse stress of the foam and the yield stress of the parent material, respectively; C_1 and C_2 are constants related to the foam structure, and they are determined by experiments. At relative densities higher than 0.3, the cell walls yield axially prior to bending [99]. Based on some experimental data for open cell foams, values of $C_1 \approx 1$ and $C_2 \approx 0.3$ have been suggested [99]. However, these values could vary based on the foam microstructure or the orientation of the cells. It was shown that strut porosity decreased the value of C_1 to 0.3 in ceramic foams [123]. In an study on open-cell aluminum foam [124], after fitting the compression test data of longitudinal and transverse direction, the values of C_1 and C_2 turned as follows: $C_1 = 0.87$ (for longitudinal direction) and 0.45 for (transverse direction), and $C_2 = 0.67$ (for longitudinal direction) and 0.43 (for transverse direction). The effect of cell-shape

does not directly appear in the Gibson-Ashby model, so it could be determined via experiments.

In their review, Zadpoor and Hedayati [47] highlighted the importance of the morphology of the repeating unit cells on the mechanical behavior of the foams, even under the condition of equal relative density. Most of the analytical models proposed for porous biomaterials are based on Euler-Bernoulli beam theory which does not consider the shear effects and assumes that the beam cross-section stays perpendicular to the bending axis. These simplifying assumptions can significantly disturb the accuracy of the models for porous structures with higher relative densities [47]. Lists of numerous analytical models which estimate the mechanical properties of open cell structures, e.g. elastic modulus and yield stress, with different cell architecture as a function of the cell dimensions are available in reference [47]. One limitation of the analytical models for porous biomaterial is the lack of estimation for large deformations after yielding. In order to predict the mechanical properties of the porous biomaterials, Zadpoor and Hedayati [47] suggested to use alternative or complementary computational approaches such as homogenization instead of relying only on dimensional analytical techniques. Homogenization is a process through which the macro-mechanical properties of a material is obtained from its micro-mechanical response (local deformation) [125].

1.9.2. Finite element modeling

Finite element (FE) methods are widely used to study the mechanical behavior of solid or porous structures. The idea of FE analysis is to divide the complex geometries into small elements with certain degrees of freedom to estimate the response in different regions of the structure, e.g. local stress, strain, deformation, etc.

The following approaches can be used to create FE models of the cellular structures: multi-cell model of a real foam sample, unit-cell, embedded-cell models and random (or ordered [126]) structure using Voronoi technique [121, 125].

In a multi-cell model, the whole structure of a sample is modelled as accurate as possible, e.g. image-based finite element model [127] . The results of this approach could be easily

compared with those of the loading experiments. However, a challenge facing such modeling approach is to properly define the boundary conditions of the non-free surfaces, e.g. a surface that contacts the compression plate. The unit-cell models comprise a limited number of periodic unit cells with regular or random cell architecture, and they are suitable for studying the influence of architectural parameters on the effective properties of the foam. The periodic boundary condition can be used to model the structures with infinite dimensions. Embedded-cell models are used to study the micro-mechanical behavior in a specific region within a surrounding matrix of a material (local behavior), e.g. a crack tip within a cellular structure, eliminating the necessity for detailed modeling of the entire structure [125].

The random Voronoi structure provides a realistic representation of the foam structure, however the technique can be computationally expensive [121, 122]. The Voronoi tessellation is a method to subdivide a space into polyhedral cells. The distance of every point in each polyhedral cell from its seed point (cell nucleus) is equal or less than the distance of those points from the seed of other cells. The Voronoi cell size could be controlled by the number of initial seeds. The creation of cells in the Voronoi tessellation process is similar to that in the actual physical process of nucleation and growth of gas bubbles within the liquid to fabricate a cellular structure. The final structure of the Voronoi foam depends on the location and the number of the nuclei (seed points) [121, 128, 129].

In a study [129], a porous model with the aid of Voronoi tessellation was developed through the following steps: the Voronoi polyhedral cells were generated and randomly introduced into a cube. After meshing the space between the cells and the cube boundaries, the cells were deleted to create the porous structure (Figure 1.13, adapted from [129]).

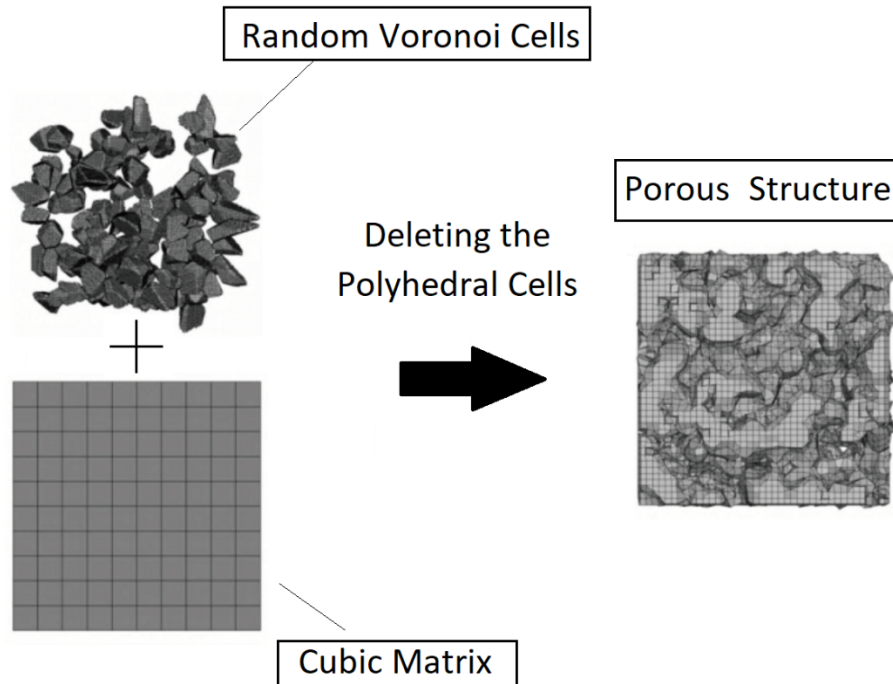


Figure 1.13- Generation of a porous structure with the aid of Voronoi polyhedral cells (adapted from [129])

Foam models generated by Voronoi technique have been used to study the effect of structural parameters on the macro-mechanical properties. Van der Burg et al. [126] studied the effect of randomness (irregularity) on the elastic modulus foams using Voronoi foams with regular tetrakaidecahedron (Kelvin cells) and rhombic dodecahedron cells as the initial samples. Different degrees of irregularities were then introduced to the regular structures by imposing random deviation ($\Delta x_1, \Delta x_2, \Delta x_3$) on the coordinates of the regularly spaced nuclei (x_1, x_2, x_3). In addition, another set of random Voronoi foams with nuclei that had been completely randomly distributed were generated. The foam struts were modeled as beams with constant circular cross-sections meeting at rigid junctions. Figure 1.14 (adapted from [126]) represents foam models with different degrees of irregularities. In their analyses, they studied the linear elastic properties of the complete regular structures, complete random structures, and the structures with progressively increasing randomness. Uniaxial tensile stresses were applied. It was shown that increasing the irregularities led to the increase of elastic modulus and Poisson's ratio. Also, as the relative density of the foams increased, the influence of axial deformation (with respect to the bending of struts) on the foam stiffness increased. Moreover,

the impact of normal stresses (with respect to bending stresses) on the linear elastic properties of random foams were higher than those of the regular foams.

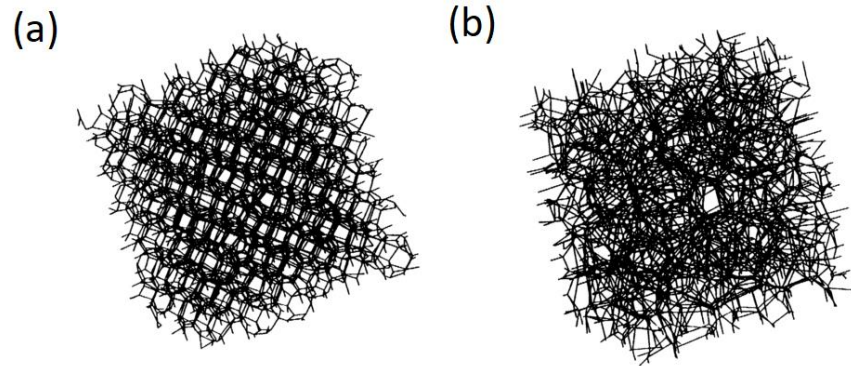


Figure 1.14- Voronoi foam models with a a) low, and b) high degree of irregularity (adapted from [126])

Finite element analysis of Kelvin cell models is a common approach to evaluate the mechanical response of open cell foams. A Kelvin cell is a space filling truncated octahedron consisting of 6 squared, 8 hexagons and 36 struts [130, 131]. Jang et al. [131], developed finite element Kelvin cell models with different degrees of complexities to estimate the elastic modulus of open cell aluminum (Al) and polyester urethane (PU) foams. They used micro computed tomography (μ CT) to estimate the architectural parameters, e.g. cell size, cell anisotropy, cross-sectional areas of the struts, strut lengths, to develop the models (Figure 1.15a, adapted from [131]). According to μ CT measurements, cells were not isotropic, so all the Kelvin cells were elongated along the rise direction. The cross-sectional area of the Kelvin cell struts varied along their length with the middle plane, which had the smallest area, being a symmetry plane of the struts. The extra volume at the junctions (caused by overlapping of the struts) was removed in the models (Figure 1.15b, adapted from [131, 132]). Three types of finite element Kelvin cell models were developed in the study: regular model with anisotropic cells meshed with shear-deformable space beam elements, regular model with anisotropic cells meshed with solid prism and brick elements, irregular model with anisotropic cells developed by the perturbation of nodes of the regular Kelvin cells; the irregular model was also meshed with the shear-deformable beam elements. In addition to

Kelvin cell models, random foam models were generated in Surface Evolver based on Voronoi approach.

Following the *in silico* uniaxial loading in rise and transverse directions, the elastic moduli of the foams were obtained and compared against the experimental results. The estimation of elastic moduli obtained by Kelvin and random models agreed well with the experimental results of the PU and Al foams. However, for Al foams, the numerical results slightly overestimated the elastic moduli, since the modelled struts had slightly larger volumes than those of the Al foams. The estimations of the random foam models were 5-10% higher than those of the Kelvin foam models. Kelvin cell models with solid elements showed the highest elastic moduli while the irregular Kelvin models showed the lowest. Given that solid elements made the models computationally expensive, they concluded that modeling the struts as shear-deformable beams is a reasonably accurate and efficient approach to predict the elastic modulus of open cell foams. However, it is crucial to account for the architectural details in the models, e.g. variation of strut cross-sectional areas along the length, cell anisotropy, volume correction at the junctions (where the struts meet). Finally, despite the simplicity of the regular (and anisotropic) Kelvin foams, the authors deemed it as a suitable engineering tool to estimate the elastic properties of open cell foams.

In a following study, Jang and Kyriakides [132] modelled the elastic and plastic compressive response of open cell Al foams using anisotropic Kelvin cell models. The struts were modelled as elastic-plastic shear-deformable beams with varying cross-sectional areas along their length. Architectural configurations were obtained from μ CT analysis. Shear bands appeared during the compression of Kelvin foams; however, their patterns were quite different from those observed in the experiments. The contact between the struts was modelled using springs (parallel to the loading direction) that had different stiffness coefficients depending on the distance between the nodes during compression. The idea of using spring elements to model the contact between the Kelvin cell struts was later adopted by Sun et al. [133] in studying the mechanical behavior of open cell Al foams coated with nanocrystalline Cu. Higher anisotropy led to higher elastic modulus and raised the compressive response of the Kelvin foams in reference [132]. The authors suggested that the

Kelvin cell model with proper representation of the architectural configuration of struts and cell anisotropy is suitable to estimate the elastic and plastic properties of the foams.

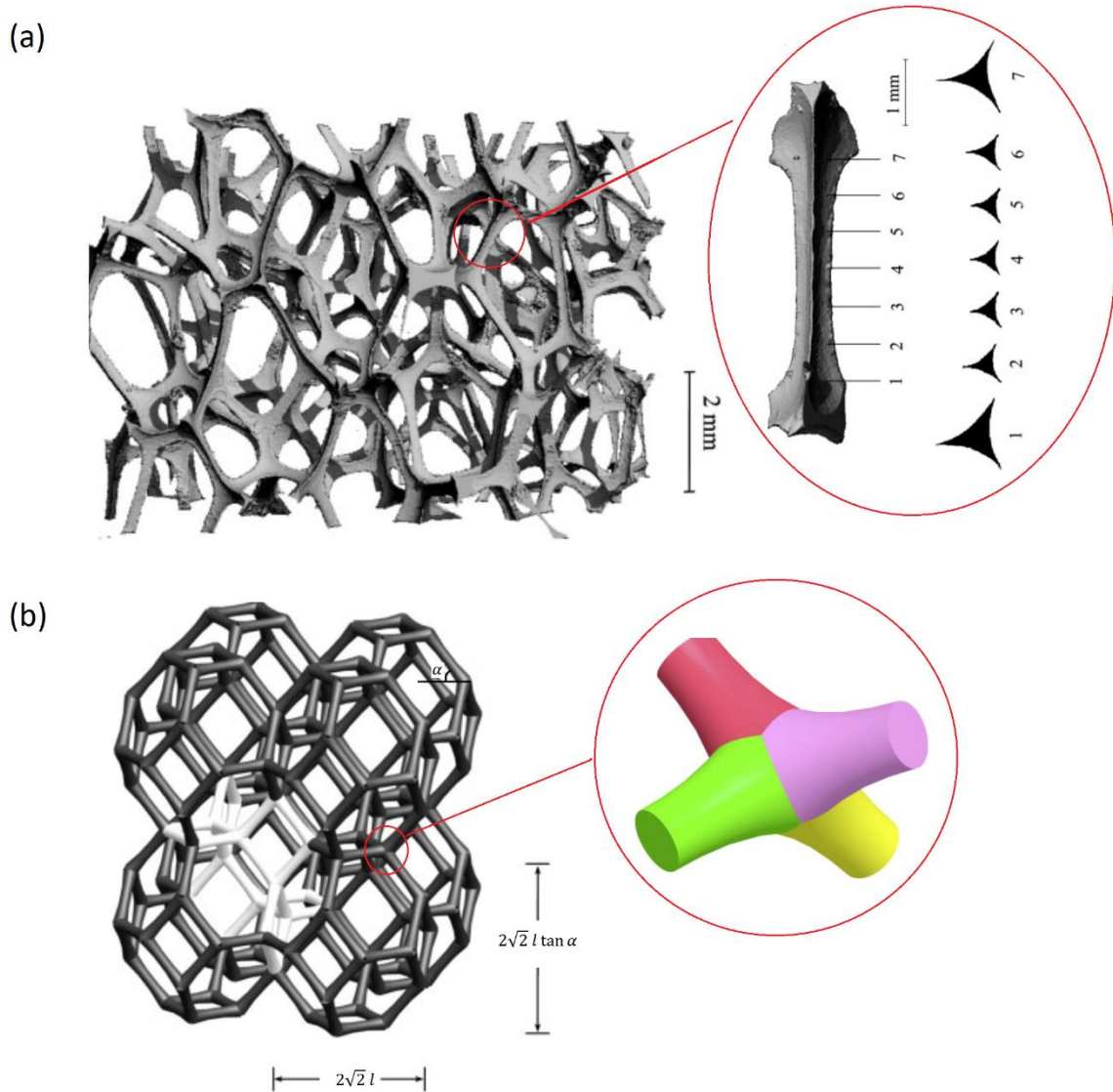


Figure 1.15- a) Micro-CT image of a PU foam and a single strut with varied cross-sectional areas (red region), b) An anisotropic Kelvin foam structure and a junction design (red region) (adapted from [131, 132])

Years after the studies of Jang et al. [131, 132], Fanelli et al. [134] proposed a finite element Kelvin cell model with 3D solid elements which represented the open cell Al foams. The model consisted of repeating Kelvin unit cells (Figure 1.16, adapted from [134]) which had struts with non-uniform cross-sectional area distribution along the length. The final

architectural configuration of the struts was obtained from the data available in the literature and the calibration of the architectural parameters based on uniaxial compression test results of the Al foams in rise and transverse directions. The Kelvin cells were regular yet anisotropic. The experimental elastic moduli of the foams were obtained by the unloading responses which better represent the elasticity than the loading response. The solid elements were defined as elastic-plastic with stress hardening. Two types of solid elements were evaluated with 8 and 20 nodes. Kelvin foams of different dimensions were generated to study the dimensional effects on the elastic modulus of Kelvin foams using linear static finite element analysis. It was observed that the foam thickness (the dimension parallel to the compressive load) did not significantly influence the Kelvin foam elastic modulus while increasing the foam area (normal to the load) increased the elastic modulus of the Kelvin foam. The model with 20-node elements led to more accurate estimations of elastic moduli in rise and transverse directions, however, it had different calibrated parameters, i.e. strut length and cell anisotropy ratio.

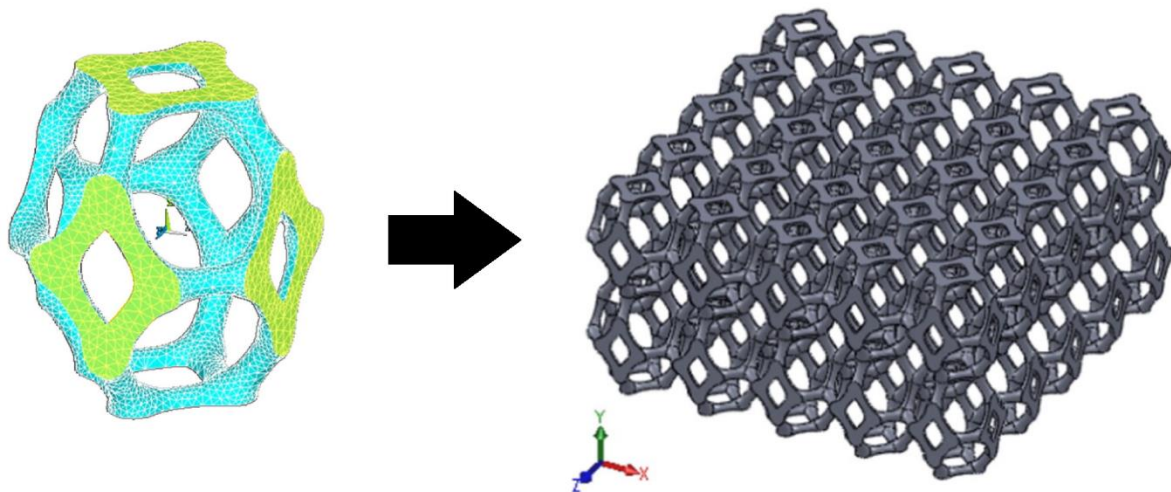


Figure 1.16- A Kelvin unit cell (left) and a Kelvin foam (right) made of repeating the unit cell (adapted from [134])

As mentioned previously, certain manufacturing approaches of open-cell foams result in foams with hollow struts. The strut hollowness increases the complexity of the open-cell structure, making it more challenging to analyze the mechanical behavior of the foam. Iio et al. [130] studied the mechanical properties of open-cell Ni-Cr foams with hollow struts (Figure 1.17a, adapted from [130]) using uniaxial compression tests and finite element

analysis of Kelvin foams which represented the foam architecture. Unlike the previously mentioned studies, the Kelvin cells were isotropic (Figure 1.17c, adapted from [130]). Elastic moduli of the foam samples were determined by linear estimation of the slope of the unloading stress-strain curves obtained by compression tests on the foam samples (Figure 1.17b, adapted from [130]). For the finite element analysis, tetrahedral elements were used, and the material was defined as elastic-plastic. Several micro-indentation tests (loading-unloading) were carried out to estimate the elastic modulus and the plastic properties (yield stress and the linear hardening parameter) of the Ni-Cr alloy. The material elastic modulus was estimated based on the unloading responses while the plastic parameters were estimated based on the combination of the loading responses of indentations as well as a FE approach (for more details, please refer to reference [130]). The architectural configuration of the Kelvin cells with hollow struts, e.g. strut length, cross-sectional dimensions and their variations along the length (Figure 1.17c), were estimated using μ CT images. The Kelvin structure with periodic boundary conditions underwent uniaxial compression, and its elastic modulus and compression strength agreed very well with the experimental results (about 10.8% and 1.1% difference for elastic modulus and the compression strength results, respectively). The authors further evaluated the strain-rate sensitivity of the Kelvin foam using a Johnson-Cook constitutive model, and they observed that higher strain-rates led to higher compressive strength values.

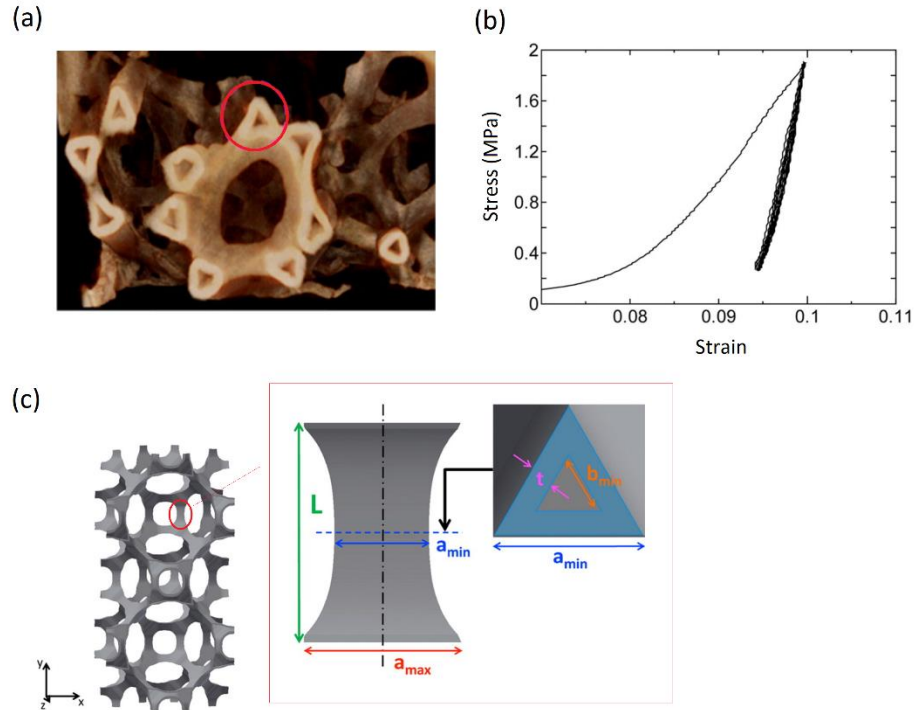


Figure 1.17- a) Micro-CT of a cell with hollow struts, b) Compressive loading-unloading responses of the Ni-Cr open-cell foam, c) Cluster of Kelvin cells and strut architectural configuration (adapted from [130])

Apart from the highlighted approaches to create a representative model of the foam structure, i.e. random cell structures based on the Voronoi technique and repeating Kelvin unit cells, image-based modeling has been also adopted by the researchers. In this approach, a 3D model of the sample is constructed using the 2D image slices obtained from micro computed tomography (μ CT) or magnetic resonance imaging (MRI) data. Various image processing codes could be used to reconstruct the 3D images (or obtain 3D data) out of 2D slices, e.g. ImageJ [135]. The advantage of this approach lies in its potential to provide a realistic and highly accurate model of the structure (assuming that suitable scanning parameters, e.g. high enough resolution). However, manipulation of architectural configurations, e.g. cross-sectional thickness of struts, to study their influence on the foam macro-mechanical properties is challenging [136]. Chen et al. [136], used this technique (using μ CT data) to develop 3D models of a closed-cell foam for subsequent FE analysis. Figure 1.18 (Adapted from [136]) shows the main three steps to produce a 3D final element foam model from μ CT

data; however, some image processing steps to increase the quality of the images explained in reference [136] are not represented.

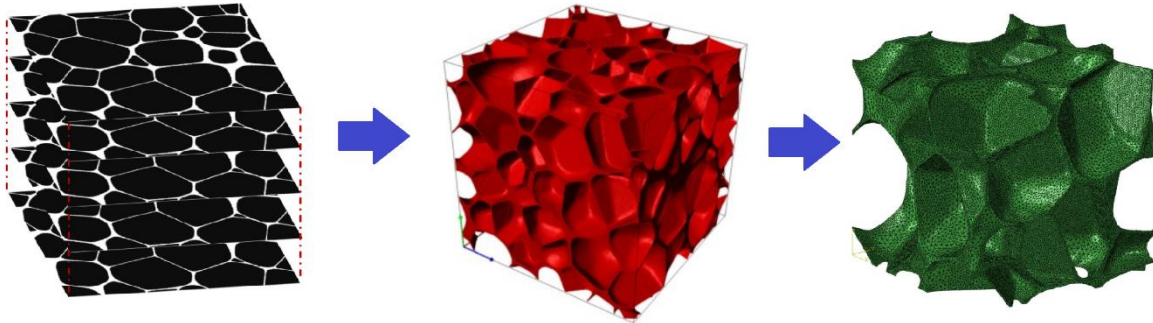


Figure 1.18- 2D μ CT slices (left), a 3D reconstructed image (middle) and a discretized model with tetrahedral elements (right) of a closed-cell foam (adapted from [136])

1.10. Computational modeling of degradation in metals

The main material degradation mechanism in metals is the corrosion of surfaces and in polymers is bulk degradation [137]. Most of the literature on computational modeling of biodegradation of metals are related to their application for temporary stents. The main types of corrosion that have been considered for modeling are uniform corrosion, pitting corrosion, and stress corrosion [137]. There are two major computational approaches to model corrosion of biodegradable metals: phenomenological and physically-based models. In phenomenological approach, unlike the physically-based approach, the effect of corrosion on architecture and material properties, e.g. mechanical properties, is modelled. Phenomenological models should be calibrated to provide realistic estimations. Physically-based models however represent the multi-physics processes causing the corrosion [137]. Given the complex nature of metal corrosion in biological environments, it would be more practical to choose phenomenological modeling approach [52]. In a few phenomenological models of biodegradability [51, 52, 138], a scalar damage parameter (D) was introduced to define the material degradation (resulting in the removal of the elements in the FE model). The damage parameter relates the elemental Cauchy stress σ_{ij} (stress at the integration point of the element) to the effective Cauchy stress $\tilde{\sigma}_{ij}$ (stress in the uncorroded part of the element) through the following equation [137]:

$$\sigma_{ij} = \tilde{\sigma}_{ij} (1-D) \quad (1.15)$$

So, when $D = 0$, no corrosion is happening, and as D approaches to 1 degradation progresses until D (almost) reaches to 1 when the material is completely degraded, leading to the removal of the element [137]. Depending on the type of the corrosion, the evolution of D from 0 to 1 (damage evolution) is defined differently. For example, simulating the uniform corrosion in magnesium stents, Gastaldi et al [138], used the following equation to define damage evolution:

$$\frac{dD_U}{dt} = \frac{\delta_U}{L_e} k_u \quad (1.16)$$

Where $\frac{dD_U}{dt}$ is the rate of damage evolution, k_u is a uniform corrosion kinetic parameter, and δ_U and L_e are the characteristic lengths of the material and the FE model, respectively. Grogan et al. [51], modelled the pitting corrosion (non-homogeneous) by introducing a stochastic pitting parameter (λ_e) into equation (1.16) as follows:

$$\frac{dD_U}{dt} = \frac{\delta_U}{L_e} \lambda_e k_u \quad (1.17)$$

Each element on the surface of the model was assigned a λ_e with a random and unique value using a “standard Weibull distribution-based random number generator” [51]. Once an element is removed, the model updates the new corrosion surface with a new value of pitting parameter which depends on the defined pit growth rate. Figure 1.19 (adapted from [51]) shows the results of the uniform and pitting corrosion models on the structure a stent model.

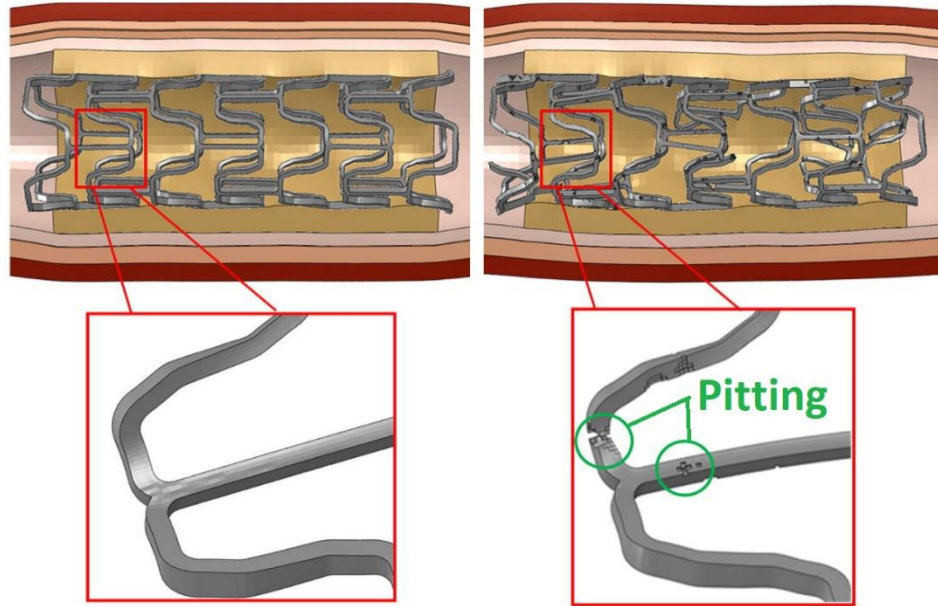


Figure 1.19- The results of the uniform (left) and pitting (right) corrosion models on the structure of a stent model (adapted from [51])

In a following study, Boland et al. [52], developed a mechanobiological FE model of Mg stent which could simulate both uniform and pitting corrosion. For elastic behavior, isotropic linear elasticity, and, for plastic behavior, J_2 flow theory and isotropic hardening were considered. An interesting novelty in the corrosion model developed in reference [52] was the conversion of fully damaged (corroded) elements (with $D \approx 1$) into “corrosion product” elements instead of deleting them, as opposed to the previous works. This was carried out by assigning a low value for both elastic modulus and yield stress of the fully damaged element, representing the soft, “shearable” and incompressible Mg corrosion products.

As mentioned earlier, the majority of the available literature on computational modeling the degradation (architectural and mechanical) of metals belong to stent applications. However, there exists publications on modeling the biodegradation of non-metallic [53] and metallic scaffolds [54]. Sulong et al. [53], modelled the surface erosion of titania scaffolds using micro computed tomography (μ CT). In their model, they estimated the erosion-induced architectural changes and their effects on the mechanical properties of the scaffolds, i.e. quasi-elastic gradient, yield and plateau stresses of the foam. To obtain the initial geometry of non-degraded foams, μ CT images (voxel resolution of $13.97 \mu\text{m}$) of the foams were used and a degradation algorithm was applied to the surface voxels to obtain the degraded foam

models. Then, in a few-step process, they were converted to FE volume meshes for the *in silico* quasi-static compression tests. Elastic-perfectly plastic material models were defined, and each degraded model (depending on its degradation level) was assigned a different material yield stress.

In a more recent study [54], μ CT image-based FE models of corroded porous Mg were developed and underwent *in silico* compression tests (Figure 1.20, adapted from [54]). In their study, Saad et al. [54], conducted dynamic immersion tests on porous Mg samples of different porosities. The degradation rate as well as the architectural parameters of the control and corroded specimens, i.e. surface area, trabecular separation (pore size) and the ratio of corroded volume to the total volume, were estimated using the constructed μ CT models (image voxel resolution of $17.2\ \mu\text{m}$). As for the *in silico* compression tests, FE models were generated from the μ CT models with the assumption of elastic-perfectly plastic material model. The estimated elastic modulus of the Mg scaffolds using the FE model were in good agreement with those of the experiments, suggesting that the relationship between the corrosion-induced architectural configuration and the elastic modulus values were decently represented by the image-based FE model. However, dependence of the accuracy of the μ CT models to the thresholding method was recognized as a limitation for such models.

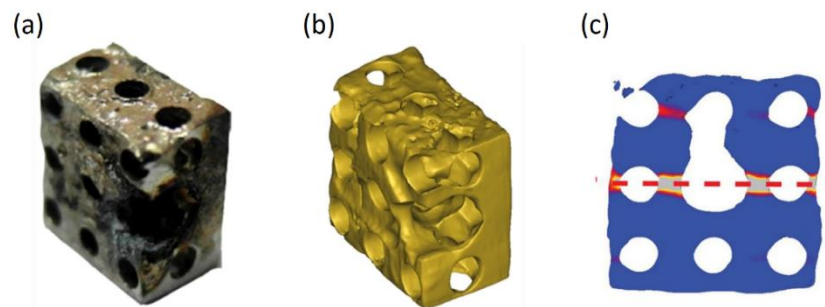


Figure 1.20- a) A corroded porous Mg specimen and b) its μ CT model, c) FE model of a corroded porous Mg under loading (adapted from [54])

2. Mechanical Properties of Open-Cell Iron Foams with Hollow Struts

2.1. Introduction

In this chapter, the influence of relative density and architectural properties (pore size, pore number, branch-strut thickness) on mechanical properties of open-cell iron foams with hollow struts were explored. Iron foam samples of different architectural properties underwent uniaxial compression tests. Deformation mechanisms of iron foam struts under compression were studied using scanning electron microscope (SEM) images. In order to study the effects of cross-sectional size/cell size and hollowness on the foam mechanical properties, Kelvin foam models with solid and hollow struts were developed and underwent *in-silico* compression tests (finite element modeling). For more details on Kelvin models please refer to section 1.9.2. of Chapter 1.

2.2. Methodology

2.2.1. Iron foam samples

The specimens were open cell pure iron foam with nominal cell diameters of 450 (IF45), 580 (IF58) and 800 (IF80) μm manufactured by Alantum. The foams were produced by the replication of open cell polyurethane (PU) foams [42]. More details on the fabrication of the Alantum iron foams are available in section 1.4 of Chapter 1. Measurements of cell sizes, pore sizes and strut thicknesses of iron foam samples were performed using scanning electron microscope images (SEM, Quanta 250 FEI, Hillsboro, OR, USA). Definition and measurements of the architectural parameters are available in section A.1 and A.2 of the Appendix, respectively (Figure A.1 and A.2, and Table A.1). One should note that these measurements are conducted on 2D SEM images, and the 3D structure of the foams is not considered. Different recommendations have been made for the pore size range of bone scaffolds [9]. The pore sizes of the IF58 and IF80 samples decently fit with the $150\mu\text{m}$ -

600 μm range referred in ref. [9]. Thus, the average measurements should be considered as estimations. The relative density of a foam is defined as the ratio of the foam density over the density of the cell-wall material, i.e. $\left(\frac{\bar{\rho}}{\rho_s}\right)$ [99]. To obtain the foam densities, the iron foam sheets were cut into cubic specimens by a stainless-steel scalpel. For each group of iron foams, three specimens were used. The dimensions of the specimens were measured via caliper to obtain the apparent volume (the bulk volume which contains the struts and pores). The mass of each specimen was measured via a sensitive digital scale. The foam densities were calculated as the ratio of masses over apparent volumes. The density of the cell-wall material (iron) was taken as 7.874 (g/cm³). The calculated average relative density values of IF45, IF58 and IF80 samples were 0.038, 0.027 and 0.025, respectively (Table 2.1). It should be mentioned that for calculation of the relative densities, it was assumed that the solid structures of the foams contained only iron, and no remainder of PU was present. To prepare the cubic samples for the mechanical tests, they were initially cut from the sheets via a stainless-steel scalpel slightly larger than the final dimensions, and the thicknesses remained unchanged. Then the width and length were reduced to the final dimension by a rotary cutting tool kit. The nominal width and length of iron foam specimens considered for the compression tests was 10 mm \times 10 mm, and the nominal thickness (along the loading direction) for IF45, IF58 and IF80 was 1.7, 2.1 and 2.6 mm, respectively. According to the ISO standard [139], the minimum value for the size of the “spatial dimensions” [139] in the specimens and for their ratio to the average pore size is 10 mm and 10, respectively. The nominal length and width of the iron foam specimens satisfy both mentioned requirements. To understand the deformation mechanisms, a new set of IF45 specimens underwent compression tests before SEM observations. They were also prepared in the same fashion as other specimens with similar nominal dimensions. However, because no quantitative analysis was involved in this part, the accuracy of the measured dimensions was not critical.

2.2.2. Mechanical testing

Different specimen sizes and cross-head speeds were considered initially to choose a proper set of test parameters. Finally, it was decided to use specimens with compression area of 100 mm², i.e. 10 \times 10 mm², and the cross-head speed of 0.001 mm/s for all the tests and analyses.

The compression tests were carried out by Instron machine (ElectroPuls E1000, Instron, Norwood, MA, USA) with a 2 kN load cell. Finally, various compression tests were carried out on IF45 specimens in order to understand the deformation mechanism of iron foam struts. The specimens underwent compression up to different strain levels, i.e. 10.8%, 12.8%, 29.8% and 49.5%. This was followed by the observation of the deformed specimens under SEM.

2.2.3. Compressive properties

In order to assess the mechanical behavior of the iron foams, the following properties were determined using the stress–strain response of the specimens: quasi-elastic gradient (QEG), yield strength (σ_y), compressive strength (σ_c). The QEG values were approximated by the linear fitting tool of the Quick Fit Gadget provided in OriginPro 2016 software (OriginLab, Northampton, MA, USA). After estimating the slope of the quasi-linear regime (QEG) on each stress–strain curve, the yield strength was approximated by 0.2% offset method [140]. For most of the iron foam specimens investigated in this study, compressive strength (σ_c) was taken as the first local maximum after quasi-elastic regime (Figure 2.8, adapted from [141]). However, if there was no apparent first local maximum, an arbitrary local maximum in the plateau region was chosen to represent the compressive strength.

2.2.4. Kelvin foam finite element model

Two groups of $2 \times 2 \times 2$ Kelvin foam models with equilateral triangular cross-sections were developed in SolidWorks Pro 2019 SP4.0 (Dassault Systemes SolidWorks Corp., Waltham, MA, USA). The first group contains 3 Kelvin foams with solid (non-hollow) struts of different dimensions, i.e. strut *cross-section side length* (Figure 2.4a) and strut *axis length* (Figure 2.4c); the Kelvin foams are referred as *Long Strut*, *Medium Strut* and *Short Strut*. The second group contains 3 Kelvin foams with hollow struts that have equal axis length but different *hollowness ratio* (r , the ratio of the *inside length* to *outside length* of the cross-section, Figure 2.4b) of 0.2, 0.5 and 0.8; the foams are referred as *Hollow Strut-r-0.2*, *Hollow Strut-r-0.5* and *Hollow Strut-r-0.8*. The relative densities of all the Kelvin foams are almost equal (0.025-0.026). Details on dimensions and relative densities of the Kelvin foams are

available in Table 2.3. After construction of the CAD model, the Kelvin foams were imported to Ansys Workbench 19.1 (ANSYS Workbench Platform, Wilde Analysis Ltd., Cheshire, UK) for finite element analysis (*in silico* compression tests) in the static structural module. Compression was applied by defining vertical displacement of the compression plate (remote displacement). Frictionless contact was defined between the bottom surfaces of the compression plate and top surfaces of the Kelvin foams. The Kelvin foams had frictionless support on the ground. Two symmetry regions were defined on the sides to reduce the computational cost. Nonlinear Mechanical elements were used, and nonlinear analysis was adopted, i.e. Large Deflection option was enabled.

Except for the *Hollow Strut-r-0.8* model which had the element size of 0.018 mm, the element size for rest of the models was 0.02 mm. The compression plate was considered to possess rigid-like material properties with an extremely high elastic modulus of 10^6 GPa. The Poisson's ratio for all materials is assumed 0.3. An elastic perfectly plastic constitutive model was used with considering effective material parameters for material elastic modulus (E_{ef}) and yield strength (σ_{yef}) (for more details on effective material parameters, please see section 3.2.7.2 and 3.2.7.3 of Chapter 3). Given that the aim of the computational modeling in this chapter is NOT to compare its results with the experimental results, the specific values of the material parameters is not critical; therefore, the same values of E_{ef} and σ_{yef} as those determined in Chapter 3 are considered for this study ($E_{ef} = 6155.99$ MPa and $\sigma_{yef} = 133.05$ MPa). The stress response was considered as the force reaction at the frictionless support divided by the area of the Kelvin foams ($1.781 \text{ mm} \times 1.781 \text{ mm}$ for the Medium Strut, $1.425 \text{ mm} \times 1.425 \text{ mm}$ for the Short Strut and $2.226 \text{ mm} \times 2.226 \text{ mm}$ for all the other models), and the strain was defined as the vertical displacement of the compression plate divided by the Kelvin foam thickness parallel to the loading direction (1.781 mm for the *Medium Strut* model, 1.425 mm for the *Short Strut* model and 2.226 mm for all the other models).

Since the effective material properties were used for the Kelvin foam model, instead of QEG and compressive strength, the phrases *elastic parameter* and *strength parameter* are employed, respectively. The elastic parameter of the Kelvin foams was obtained by the same method used for determining QEG of the iron foams in this chapter. The strength parameter of the Kelvin foams was considered as the maximum stress value on their stress-strain curves.

2.2.5. Statistical analysis

Values of E , σ_y , σ_c were compared against one another for different groups of specimens via statistical analysis. The results were shown as mean \pm standard deviation. In order to draw a reliable conclusion, hypothesis testing (One-way ANOVA followed by Tukey test) along with non-parametric tests (Kruskal–Wallis ANOVA, Two-Sample Kolmogorov–Smirnov Test) were carried out in the OriginPro software. The non-parametric tests were conducted due to the small sample sizes. Unlike parametric hypothesis tests, the normal distribution of population is not assumed when conducting non-parametric tests [142].

2.3. Results

2.3.1. Architectural properties of the iron foams

Figure 2.1 depicts the structure of iron foams with different average cell sizes. Different strut thickness values of the iron foams of different cell sizes are shown in Table 2.1. The mean values of both branch-strut and end-strut thicknesses of the IF80 specimen are significantly higher than those of the IF45 and IF58 specimens.

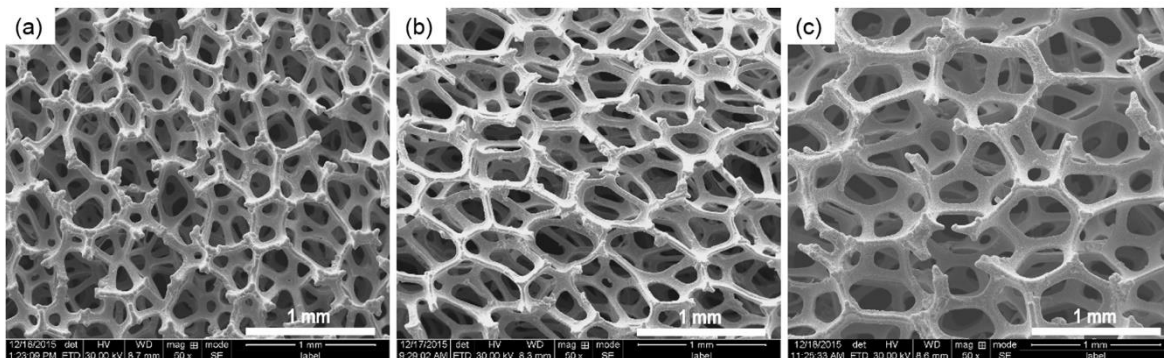


Figure 2.1- Scanning electron microscope (SEM) images of iron foam structures: (a) IF45; (b) IF58; and (c) IF80

Table 2.1- Relative density, cell size, pore size, end-strut and branch-strut thickness values of the iron foams

	Relative density	Cell size (μm)	Pore size (μm)*	End-strut (μm)	Branch-strut (μm)
IF45	0.038 ± 0.001	461.77 ± 72.26	155.2 ± 28.89	74.73 ± 10.3	55.52 ± 6.18
IF58	0.027 ± 0.001	617.73 ± 76.08	150.8 ± 29.43	63.62 ± 9.95	59.88 ± 7.55
IF80	0.025 ± 0.001	828.11 ± 79.87	157.3 ± 28.5	97.79 ± 17.54	80.91 ± 12.27

*Between 100 and 200 μm

2.3.2. Compressive behavior of the iron foams

The stress–strain curves resulted from the compression tests on iron foams of different cell sizes are shown in Figure 2.2. The shifting of the curves within a sample group can be the result of non-identical micro architectural configurations even if they are in the same sample group. The IF45 specimens tend to have higher compression strength than those of IF58 and IF80 specimens. Strain hardening up to the peak followed by a softening is more visible in the stress–strain curves of IF45 and IF80 specimens than those of IF58 specimens. The compressive properties of the iron foams are summarized in Table 2.2. There exists a “V-type” variation of the mechanical properties with respect to the cell sizes, i.e., the mean values of the compression properties of the iron foams of 580 μm nominal cell sizes tend to be lower than those of the specimens with 450 and 800 μm nominal cell size.

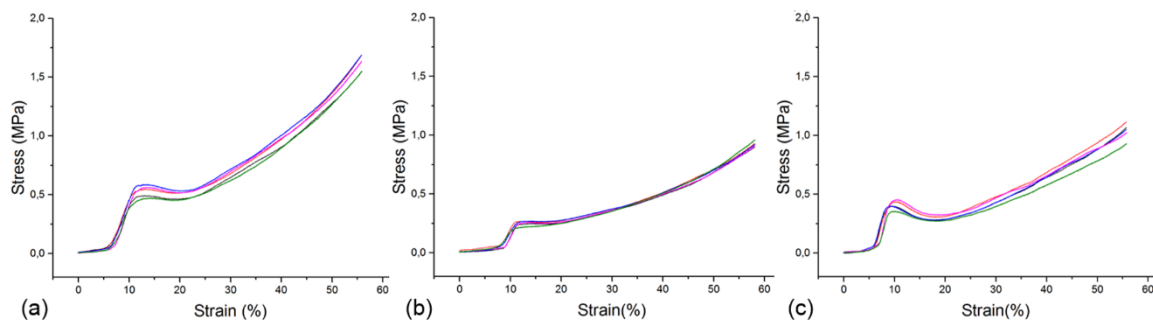


Figure 2.2- The stress-strain curves of the compression tests for different cell sizes: (a) IF45, (b) IF58, and (c) IF80

Table 2.2- Compressive properties of iron foam samples

	QEG (MPa)	σ_y (MPa)	σ_c (MPa)
IF45	11.6 ± 1.39	0.48 ± 0.07	0.53 ± 0.05
IF58	8.24 ± 0.67	0.23 ± 0.03	0.26 ± 0.02
IF80	17.1 ± 2.3	0.36 ± 0.03	0.41 ± 0.04

2.3.3. Statistical analysis

Figure 2.3a and b represents the quasi-elastic gradient (QEG) and yield strength (σ_y) box-charts of the specimens under compression, respectively. Although both properties represent a V-type variation, an interesting difference is observed between the two: the highest QEG is presented by IF80 specimens, while the highest yield strength is presented by IF45 specimens. Figure 2.3c depicts the compressive strength box-chart of the iron foam specimens of different cell sizes. The figure shows a V-type variation of the strength with IF45 sample having the highest mean value. The mean values of compression strengths for IF45, IF58 and IF80 samples are 0.53, 0.26 and 0.41 MPa, respectively. According to the ANOVA and Tukey tests, at $\alpha = 0.05$, all the population means of σ_y , E and σ_c were significantly different from one another. The results obtained from non-parametric tests agreed well with those of hypothesis tests: the null hypothesis in Kruskal–Wallis ANOVA test was rejected at significance level of 0.05. Two-sample Kolmogorov–Smirnov (K–S) tests with significance level of 0.05 were carried out within each possible sample pair. The results of K–S tests showed that except for the yield strength difference between IF45 and IF80 samples not being significantly different (which contradicts the result drawn from the Tukey test), all the other distributions were significantly different from one another. However, considering the difference shown by the box-chart of Figure 2.3b, the Tukey test result is more reliable, i.e., the difference between the yield strength value of IF45 and IF80 populations is significant.

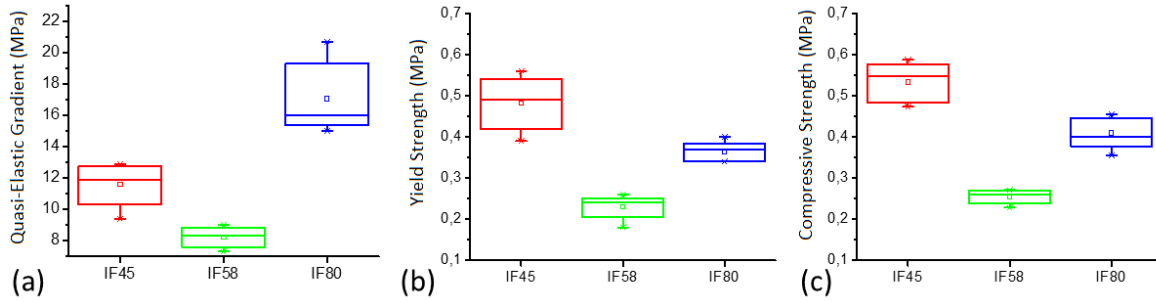


Figure 2.3- Box charts for iron foam specimens of different cell sizes: (a) QEG; (b) Yield strength; (c) Compressive strength

2.3.4. Computational modeling

The mechanical response of the Kelvin foams with solid struts were almost identical (Table 2.4 and Figure 2.5a). The elastic and strength parameter of the *Short Strut* Kelvin foam was slightly higher than those of the *Long Strut* foam by 2.4% and 4.8%, respectively, which are not significant. On the other hand, as the hollowness ratio (r) increased, the mechanical properties tended to increase (Table 2.4 and Figure 2.5b). As the hollowness ratio increased from 0.2 to 0.8, the elastic and strength parameters increased by 157.1% and 54.5%, respectively.

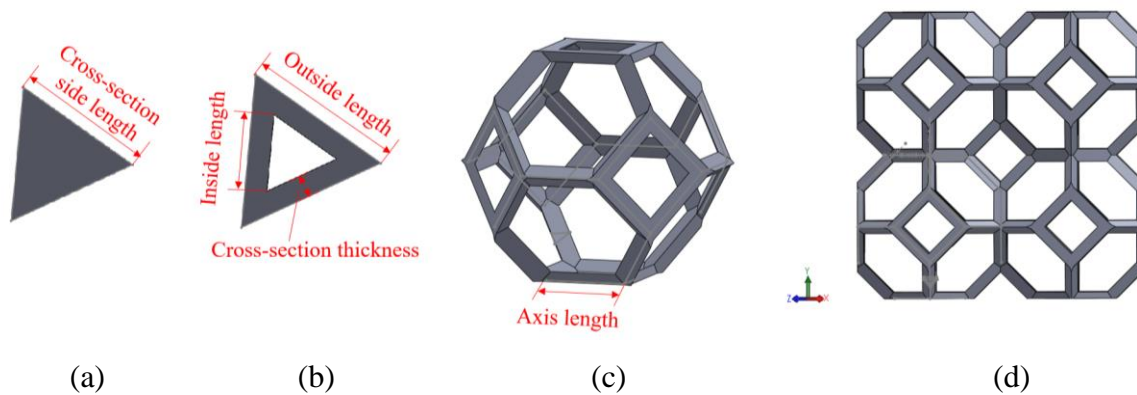


Figure 2.4- Architectural parameters of the Kelvin foams, a) Solid-strut cross-section, b) Hollow-strut cross-section, c) Kelvin unit cell, d) Kelvin foam side view

Table 2.3- Dimensions and relative density of the Kelvin foams

Kelvin Foam Type	Strut axis length (μm)	CS* side length (μm)	CS inside length (μm)	CS outside length (μm)	CS thickness (μm)	Hollowness ratio	Relative density
Long Strut	393.5	98	NA	NA	NA	NA	0.0262
Medium Strut	314.8	78.5	NA	NA	NA	NA	0.0263
Short Strut	251.9	62.7	NA	NA	NA	NA	0.0262
Hollow Strut-r-0.2	393.5	NA	20	100.02	23.1	0.20	0.0260
Hollow Strut-r-0.5	393.5	NA	56.6	113.2	16.3	0.50	0.0253
Hollow Strut-r-0.8	393.5	NA	127	163.3	10.5	0.78	0.0255

* CS: cross-section

Table 2.4- Mechanical properties of the Kelvin foams

Kelvin Foam Type	Elastic Parameter (MPa)	Strength Parameter (MPa)
Long Strut	4.1	0.21
Medium Strut	4.1	0.22
Short Strut	4.2	0.22
Hollow Strut-r-0.2	4.2	0.22
Hollow Strut-r-0.5	5.1	0.24
Hollow Strut-r-0.8	10.8	0.34

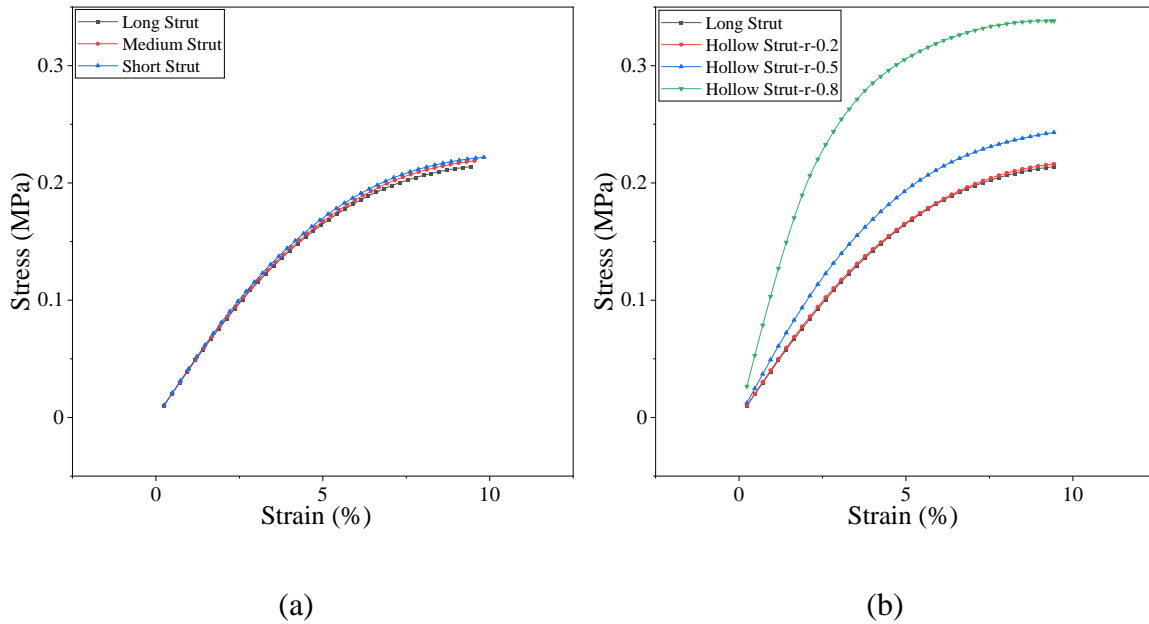


Figure 2.5- Mechanical response of the Kelvin foams with a) solid and b) hollow struts

2.3.5. Deformation of the iron foam struts under compression

Figure 2.6 depicts four specimens compressed up to strain levels of 10.8%, 12.8%, 29.8% and 49.5%. The areas marked with red circles depict the struts that experienced bending or other forms of plastic deformation. That said, some of the deformations could be wavy imperfections already existed in the foams before compression. Because the direction of the compressive force is perpendicular to the image surfaces, it is difficult to identify buckling in the struts, if existed. However, considering that the majority of the struts are not completely perpendicular or parallel to the loading direction, it is expected that both bending and buckling contributed to the deformation of some struts.

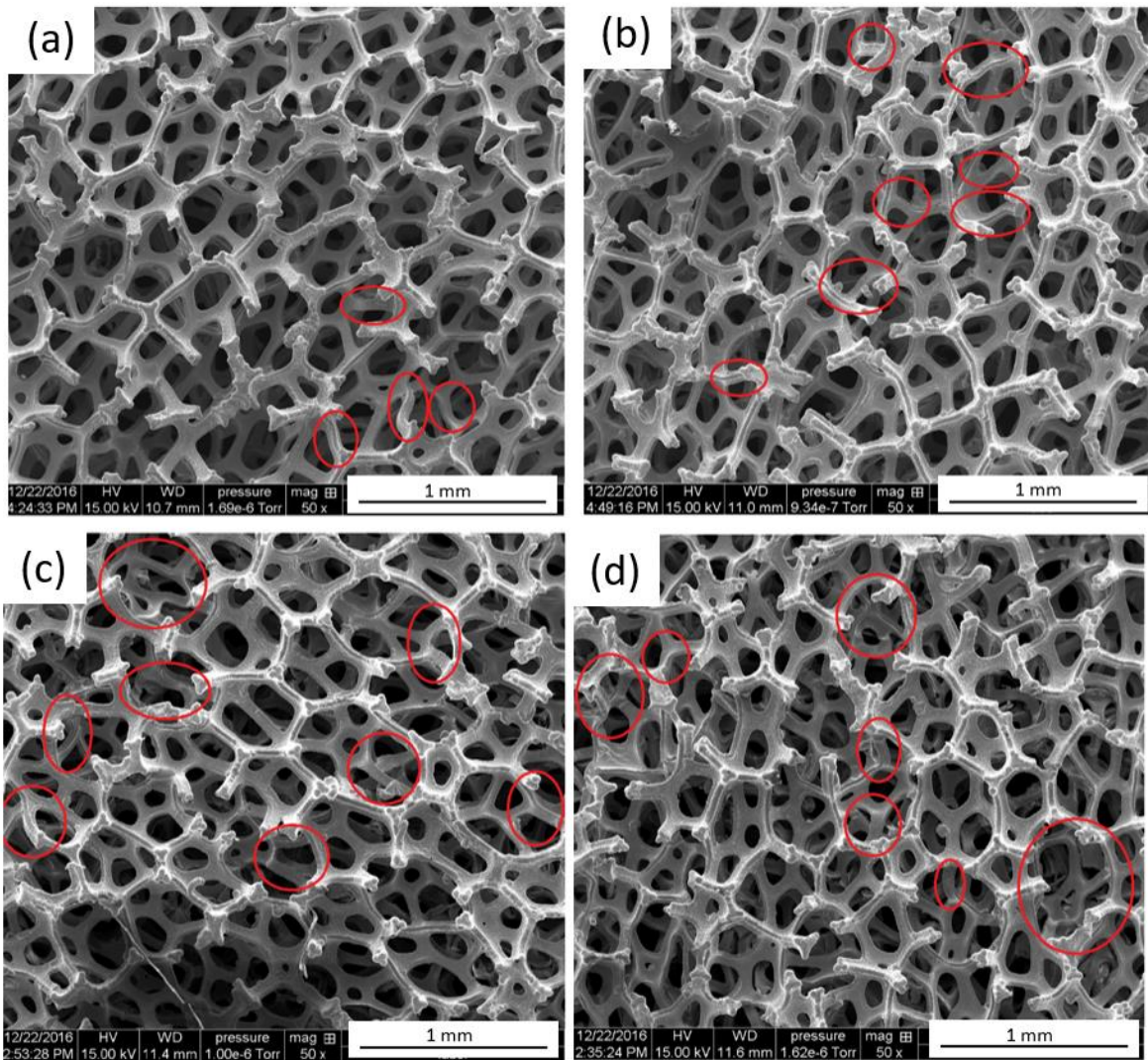


Figure 2.6- Deformed structure of four IF45 specimens at compression strain of: (a) 10.8%; (b) 12.8%; (c) 29.8%; and (d) 49.5%

Figure 2.7 depicts the magnified images of some of the marked regions in Figure 2.6. It shows the deformation of struts of four specimens at different stages of compression after quasi elastic regime. In samples with the maximum compression strain levels of 10.8%, 12.8% and 29.8%, formation of S-shape plastic hinges in some of the marked regions can be observed, e.g., region 3, 8, and 14 (Figure 2.7a). C-shape bending is observed in some of the struts of specimens with compression strains of 29.8% and 49.5%, e.g., region 13, 24 and 26 (Figure 2.7b). Plastic S-shape and C-shape deformation in some struts of open cell aluminum alloy (A356) and 316L stainless steel foams under quasi-static compression has been observed in the previous works [143, 144]. Deformation bands are present in a few struts of

the specimen with the highest level of compression strain (49.5%). These adjacent struts are marked with red circles of number 21, 23 and 27 (Figure 2.7c).

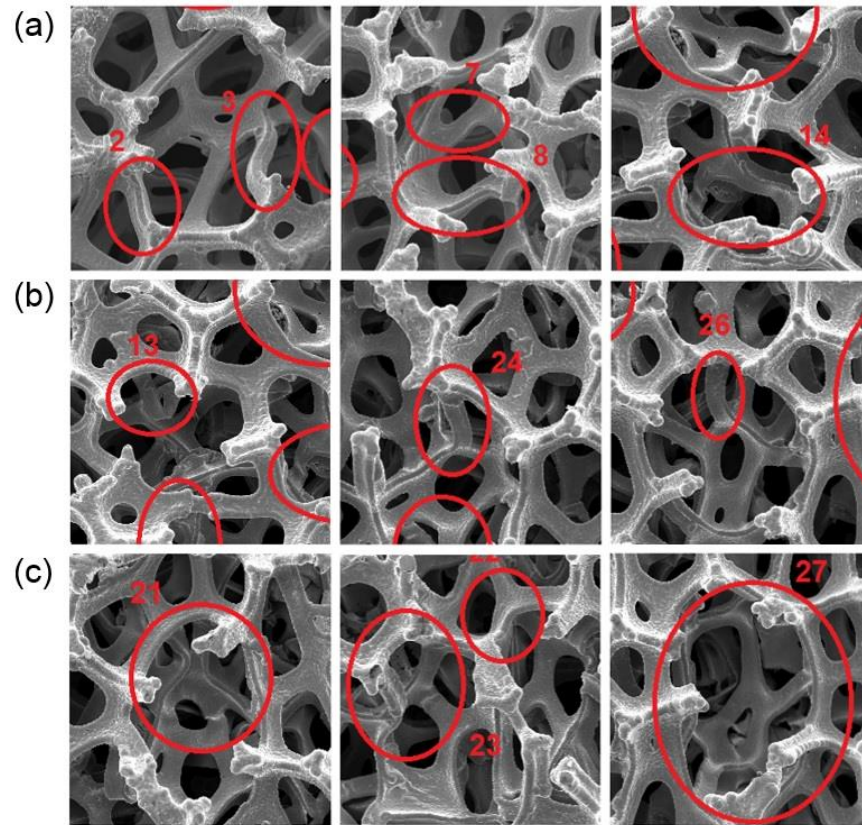


Figure 2.7- Different shapes formed on plastically deformed struts: (a) S-shape; (b) C-shape; and (c) Deformation bands

2.4. Discussion

2.4.1. Mechanical properties of the iron foams, the influence of architectural properties

The architectural of the foam as well as mechanical properties of the parent material influence the mechanical properties of the foam [99]. Figure 2.8 (adapted from [141]) represents a typical mechanical response of a foam under compression. During compression, three main regimes are experienced: linear elastic, plateau, and densification which are represented by numbers 1, 2 and 3, respectively. Based on the stress-strain response of the iron foams in this

study, it is expected that they only underwent (quasi) elastic and plateau regimes. In metal foams, or other foams made of materials with a plastic yield point, as the stress goes beyond the linear elastic region, plastic collapse, i.e. appearance of plastic hinges, takes place. The collapse of cell walls continues until almost the entire cells collapse, then, to apply further strain, much higher level of stress is required. This marks the onset of densification in the compression diagrams [99]. Some metal foams experience significant local plastic deformations during elastic regime, e.g. closed cell aluminum foams [122]. Such plastic deformations would cause the loading stiffness of the foam become lower than the unloading stiffness, thus it is preferable to use the phrase quasi-elastic instead of elastic when referring to the first deformation regime during loading. Follow up compression tests on IF80 foams showed that loading stiffness is lower than the unloading one.

Significant softening after the stress peak was observed in many of the iron foam specimens (mostly IF45 and IF80 foams, Figure 2.2). In reference [122], softening in closed-cell aluminum foams (with different loading and unloading stiffness values) was attributed to the collapse of the cells across a section of the foam; this is resulted from the plastic collapse of a deformation band that is oriented almost perpendicular to the loading direction. Similarly, plastic collapse of struts/cells may have caused the softening in IF45 and IF80 iron foams, leading to softening after the peak. Thus, absence of a significant softening indicates that massive cell collapses did not take place immediately after the beginning of the plateau.

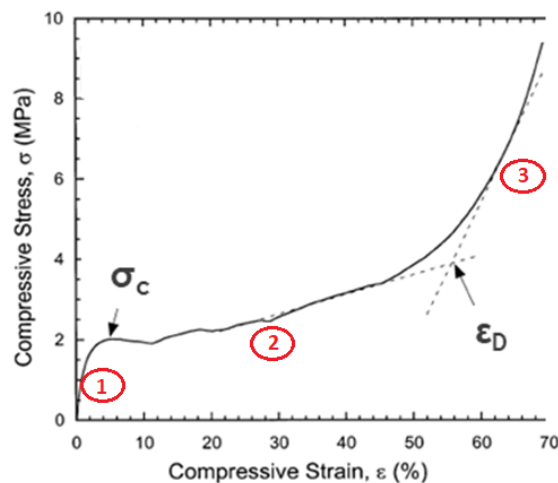


Figure 2.8 - A typical stress-strain response of a metal foam under compression (adapted from [141])

The most important architectural properties in terms of foam mechanical properties are relative density, cell type (open or close) and the level of anisotropy in the cells. The most influential parent material properties are the material density, the elastic modulus, the yield stress, the fracture strength and the creep parameters [99]. Because the cell-wall material properties of the samples were not significantly different in this study, it is expected that the relative density and architectural properties such as pore size, cell anisotropies, and strut thicknesses (branch strut and cross-sectional thickness values) influence the mechanical behavior of the iron foams. In the work of Amsterdam et al. [145], it was observed that the plastic collapse stress and tensile strength values of open cell aluminum foams tended to increase with increasing the relative density. In this study, however, the relative density of IF58 and IF80 samples are very close, so it is expected that architectural parameters had more contribution to the difference between the mechanical properties of the two samples.

The influence of cell size on mechanical behavior of the open cell structures has been a matter of controversy. As stated in reference [122], in most cases, mechanical properties of metal foams do not depend on cell size. This was observed in the study of the deformation behavior of the open-cell stainless steel conducted by Kaya and Fleck [144], wherein, at the same relative density, the inhomogeneity differences in the microstructure (and not the cell size) was found the cause of difference between plateau stress values. Investigating the influence of density, cell size and cell shape on the mechanical properties of open cell 6101 aluminum foams, Nieh et al [146] observed that, with similar densities, cell size did not significantly influence the strength while the cell shape did to some extent [146]. On the other hand, difference in cell size led to different elastic modulus and compressive strength of rhombic dodecahedron lattice structures [147]. In this study, finite element analyses of Kelvin foams with solid struts, different cell size and (almost) equal relative densities suggest that cell size does not significantly influence the stiffness and compressive strength of the open cell cellular structure. This is in line with the Ashby and Gibson theoretical models (Eqs. 1.13 and 1.14) which derive the relative density based on the ratio of strut cross-section side length to the strut axis length [99]. This ratio among the Kelvin foams with solid struts developed in this study was 0.25, leading to (almost) equal stiffness and strength.

In their work, Jian et al. [148] observed that the young's modulus and compressive and fracture strength of porous NiTi alloy samples (manufactured by space-holder method) increased with decreasing mean pore size. The samples of different porosities and pore sizes underwent quasi-static compression tests (crosshead speed of 2.4 mm/min) while the range of porosities and mean pore sizes were 53%–55.6% and 277.2–1013.7 μm , respectively. Therefore, the variation between pore size values was more considerable than that of the porosities. However, studying the effect of pore size on the mechanical properties of open cell aluminum foams with spherical pores, Jiang et al. [149] demonstrated that compressive stress–strain diagrams of aluminum foams (manufactured by space holder method) generally raised as the pore sizes increased.

Unlike the aforementioned research works wherein increasing pore size resulted in either increasing or decreasing the compression strength, in the study of Xu et al. on biomedical porous NiTi alloys (manufactured by space-holder technique) [150], the elastic modulus, strength and microhardness values of the foams varied with pore sizes in a “S type” fashion (all samples had a porosity of $\sim 50\%$), i.e., as the pore size increased once, the values of the mechanical properties dropped initially, and after the second and third increase of the pore size, they increased and decreased, respectively. They attributed this behavior of porous NiTi alloys to the pore size as well as the number of pores both of which represent the same effect on the mechanical properties of the porous alloys, i.e., the increase of the pore size and the number of pores would result in a decrease in the values of mechanical properties. According to the information provided by the manufacturer, the nominal pore density of iron foams with nominal cell size of 450, 580, 800 μm is 100–110, 90–100, and 60–70 ppi (the number of pores per linear one inch). Therefore, it is expected that the number of pores in IF80 specimens to be significantly lower than that of IF45 and IF58 specimens (around 38% and 32%, respectively). On the other hand, increasing the average pore size from IF58 to IF80 is around 4% for both pore size ranges of $100 < \text{pore size} < 200$ and $\text{pore size} > 200$ (using the data provided in Table A.1 of the Appendix). Therefore, it is expected that the decrease of the number of pores is more influential than the increase of the pore sizes, leading to raise the QEG, yield and compression strength from IF58 to IF80 sample. An important parameter which influences the compressive strength of the foam is the ratio of strut thickness to length,

and it has a direct relationship with it [151]. According to the measurements on SEM images, the ratio of the average value of the branch-strut thickness to that of strut length for IF45, IF58 and IF80 is 0.35, 0.30 and 0.37, respectively. This can also explain the higher strength of IF80 sample than that of the IF58. One should note that the effects of strut hollowness on the mechanical properties of the iron foams in the abovementioned arguments is not considered.

For the case of QEG values, although the V-type variation is still present, an important difference is noticed: IF80 specimens showed the highest values of QEG unlike the other two properties (σ_y , σ_c) for which IF45 specimens shows the maximum values. This can be due to the high influence of the branch strut thicknesses which are significantly higher for IF80 specimens than those of the other two groups (Table 2.1). It is possible that higher branch-strut thickness leads to higher second moment of inertia (I) at the strut cross-sections, leading to a higher elastic stiffness of the bending struts which results in higher stiffness of the foam under compression [99, 152]. That said, data regarding the cross-sectional features of IF45 and IF80 struts is not available, so higher I values in IF80 struts is only a possibility. Lower QEG of IF45 could also be attributed to the higher plastic deformations during quasi-elastic regime, or higher influence of surface plasticity during loading due to the lower thickness of the specimens (1.7 mm Vs. 2.6 mm) [144]. FE analysis of Kelvin foams shows that stress concentrations tend to take place near the junctions. Thus, having smaller cell size would increase the number of such highly stressed sites.

In open cell foams, hollowness of the struts significantly influences the mechanical properties of the foams [153]. One limitation in this study is that the detailed cross-sectional features of the struts of the foams were not available. Thus, comparison of strut hollowness ratios is not presented (in the next chapter, detailed cross-sectional analysis for only one type of the open-cell foams is presented). However, FE analysis of the Kelvin foam models clearly show that under constant relative density, increasing strut hollowness results in increasing both stiffness and compressive strength. Also, the increase of the stiffness is higher than that of the strength. As the hollowness ratio of the Kelvin foams increase from 0.2 to 0.8, the stiffness increases 2.6 times as much while the strength increases 1.5 times as much. This is consistent with the modified version of Ashby-Gibson models which introduces hollowness enhancement

factors to estimates the elastic modulus and plastic collapse stress of open cell foams with hollow struts [153]:

$$\left(\frac{\bar{E}}{E_s}\right) = f_1 C_1 \left(\frac{\bar{\rho}}{\rho_s}\right)^2 \quad (2.1)$$

$$\left(\frac{\bar{\sigma}_{pl}}{\sigma_{ys}}\right) = f_2 C_2 \left(\frac{\bar{\rho}}{\rho_s}\right)^{\frac{3}{2}} \quad (2.2)$$

Where f_1 and f_2 are the enhancement factors of foam elastic modulus and plastic collapse stress, respectively, and they are obtained as follows [153]:

$$f_1 = \frac{1+r^2}{1-r^2} \quad (2.3)$$

$$f_2 = \frac{1-r^3}{(1-r^2)^{\frac{3}{2}}} \quad (2.4)$$

Where r is the hollowness ratio. Table 2.5 presents f_1 and f_2 based on different r values. Once r increases from 0.2 to 0.8 f_1 increases by 3.8 folds while f_2 increases by 2.0 folds. Thus, hollowness has a higher influence on the stiffness than the compressive strength of an open cell structure. One should note that when r is too large, e.g. $r > 0.9$, the struts may fail due to buckling as the cross-sections are extremely thin [153].

Table 2.5- Variation of f_1 and f_2 as a function of r values

Hollowness ratio (r)	f_1	f_2
0.2	1.08	1.05
0.5	1.67	1.35
0.8	4.11	2.14

2.4.2. Deformation of struts under compression

In open cell foams with low relative densities, $\left(\frac{\bar{\rho}}{\rho_s}\right) \leq 0.1$, cell wall bending mainly controls the linear elastic regime. Plastic collapse, i.e. formation of plastic hinges in the struts of metal foams, of the cells during compression gives rise to the plateau regime. The plastic hinges form in the foams made by materials that experience plastic yielding such as metals or rigid polymers [99]. Figure 2.9 (adapted from [99]) represents a simple model of an open cell foam under linear elastic deformation as well as the formation of plastic hinges during plastic collapse.

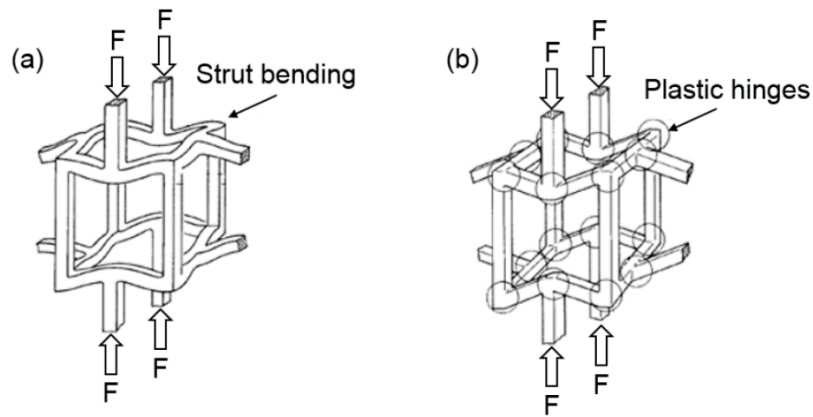


Figure 2.9- A simple model of an open cell foam experiencing: (a) Linear elastic deformation; and (b) Formation of plastic hinges during plastic collapse (adapted from [99])

Different modes of plastic deformation of struts, including S-shape and C-shape deformations and deformation bands in IF45 specimens are shown in Figure 2.7. In Kaya and Fleck's work [144], struts bending and buckling were addressed as the deformation mechanisms leading to plastic response of open cell stainless-steel foams. In Daxner's work [154], buckling and bending are pointed out as dominant deformation mechanisms in open-cell metal foam struts. In the work of Schuler et al. [143], C-shape and S-shape deformation of struts of open-cell aluminum foams under compression are attributed to bending and torsion. Thus, given that the strut orientation relative to the loading direction is an influential factor on deformation mode of the foams [151], the deformation of an open cell iron foam under compression is a complex mechanism which could be the product of different mechanisms in conjunction with each other such as bending, buckling and torsion. However,

some of the struts may experience only one form of deformation. The complexity of the strut deformations has been acknowledged in reference [143] as well.

2.5. Concluding remarks

Open cell iron foams with hollow struts with different architectural properties, i.e. cell size, pore size, branch-strut thickness, underwent compression tests, and the strut deformations were explored. The effects of cell size and strut hollowness ratio on the mechanical behavior of foams were studied using finite element analysis of Kelvin foams. The following concluding remarks can be stated:

- A “V-type” variation of the mechanical properties, i.e. QEG, yield and compressive strength, were observed with IF58 foams showing the minimum values of the mechanical properties.
- IF45 shows the highest yield and compressive strength due to the highest relative density among the foam samples.
- Although the relative density of IF80 foams is lower than those of IF45 foams, they indicated the highest QEGs. This is attributed to two possible reasons: *i*) IF80 struts had higher second moment of inertia (I) as the result of higher branch-strut thickness, *ii*) IF45 foams experience more plasticity during quasi-elastic deformation due to stronger presence of structural inhomogeneities, or the influence of surface plasticity during loading is higher in IF45 foams due to their lower thickness.
- FE analysis of Kelvin foams confirmed that higher hollowness ratio of struts leads to higher stiffness and compressive strength; both Kelvin and analytical models indicated that the influence is more significant for stiffness values.
- S-shape and C-shape plastic deformations as well as deformation bands were observed in struts of IF45 foams under compression.
- Deformation of the open cell iron foams under compression could be the product of different mechanisms in conjunction with each other such as bending, buckling and torsion.

3. Post-corrosion Mechanical Properties of Absorbable Open Cell Iron Foams with Hollow Struts

Résumé

Des analyses approfondies des propriétés mécaniques post-corrosion et de l'architecture des mousses de fer à cellules ouvertes avec des entretoises creuses comme échafaudages osseux résorbables ont été effectuées. Les variations des caractéristiques architecturales des mousses après 14 jours d'immersion dans une solution de Hanks ont été étudiées à l'aide de microtomographie et d'images au microscope électronique à balayage. Un modèle de mousse Kelvin par éléments finis a été développé, et la modélisation numérique et les résultats expérimentaux ont été comparés les uns aux autres. Il a été observé que les échantillons de mousse de fer étaient principalement corrodés dans les régions périphériques. À l'exception du gradient quasi-élastique, les autres propriétés mécaniques (c'est-à-dire la résistance à la compression, la limite d'élasticité et l'absorption d'énergie) ont diminué de manière monotone avec le temps d'immersion. La présence de produits de corrosion adhérents a amélioré la capacité de charge des mousses de fer à cellules ouvertes à de petites déformations. La prédiction par éléments finis de la réponse quasi-élastique de la mousse corrodée à 14 jours était en accord avec les résultats expérimentaux. Cette étude souligne l'importance de considérer le mécanisme de corrosion lors de la conception d'échafaudages résorbables; ceci est indispensable pour offrir des propriétés mécaniques souhaitables dans des matériaux poreux lors de la dégradation dans un environnement biologique.

Abstract

In-depth analyses of post-corrosion mechanical properties and architecture of open cell iron foams with hollow struts as absorbable bone scaffolds were carried out. Variations in the architectural features of the foams after 14 days of immersion in a Hanks' solution were investigated using micro-computed tomography and scanning electron microscope images. Finite element Kelvin foam model was developed, and the numerical modeling and

experimental results were compared against each other. It was observed that the iron foam samples were mostly corroded in the periphery regions. Except for quasi-elastic gradient, other mechanical properties (i.e. compressive strength, yield strength and energy absorbability) decreased monotonically with immersion time. Presence of adherent corrosion products enhanced the load-bearing capacity of the open cell iron foams at small strains. The finite element prediction for the quasi-elastic response of the 14-day corroded foam was in an agreement with the experimental results. This study highlights the importance of considering corrosion mechanism when designing absorbable scaffolds; this is indispensable to offer desirable mechanical properties in porous materials during degradation in a biological environment.

3.1. Introduction

Bone tissue scaffolds are considered as alternatives to bone grafting without potential drawbacks that involve a risk of morbidity, disease transmission or donor site shortage ([5, 6]). They provide mechanical support and space for regeneration of bone tissues. Bone scaffolds can be considered as temporary implants since they are not needed after the complete formation of new tissues. Absorbability (biodegradability) is one of the inherent characteristics of temporary tissue scaffolds [8]. An ideal absorbable (biodegradable) scaffold degrades gradually while providing mechanical and biological support for tissue formation. When a new tissue is formed, the scaffold would disappear. Design and fabrication of biodegradable scaffolds are topics of interest for the researchers due to the growing need for such cellular implants [9].

Many biodegradable scaffolds are made of polymers; however, metallic scaffolds are better suited for load-bearing applications due to their superior mechanical properties [18, 39]. Therefore, extensive research has been conducted on porous absorbable metals for bone scaffolding applications [18, 21, 23]. In scaffolds, the pores must be extensively interconnected (open cells) to facilitate tissue regeneration, vascularization and nutrient transfers [10]. Introducing porosity increases degradation (corrosion) rate of metals by enhancing the surface area and thus reduces their mechanical stiffness/strength [30]. Absorbable metal scaffolds need to maintain their mechanical integrity during the

degradation process to prevent implant failure under mechanical loads [6, 13]. Among the mostly investigated absorbable metals, iron has the lowest corrosion rate and the highest mechanical strengths [40]. These two properties inhibit iron foams from having excessively high corrosion rate and low mechanical strength, making them a proper candidate for tissue scaffolding.

Corrosion of absorbable metal implants introduces a potential risk for mechanical failure [46]. Therefore, understanding the variation of mechanical properties during corrosion is crucial. The architectural features highly influence the multifunctional properties of porous materials [47, 48, 155, 156]. Corrosion alters the microarchitecture of metallic foams, leading to a variation in their mechanical properties [19]. This highlights the necessity to study the post-corrosion architectural features (e.g. pore size and strut shape/dimension) of the biodegradable porous scaffolds. A few studies have investigated the variations of the mechanical properties of absorbable porous metals during corrosion [15, 23, 28, 31, 33, 49, 50]. However, there is a lack of detailed analysis to explain such variations based on the post-corrosion architectural parameters. To the best of the authors' knowledge, no study has assessed the variation of the microarchitecture of open-cell iron foams with hollow struts after degradation. Finite element (FE) modelling has been performed to understand and predict the post-corrosion mechanical behavior of absorbable metal stents and scaffolds [51, 52, 54]. For the case of absorbable porous scaffolds, FE modelling can provide insights on the effect of variation of architectural parameters on the mechanical properties of scaffolds. *In vitro* immersion tests in conjunction with elastic-plastic FE modeling have been performed to predict the variation of mechanical properties in magnesium-based and zinc specimens [49, 54, 61].

Highly porous open cell iron foams (above 90% porosity) with hollow struts possess the values of the quasi-elastic gradient (QEG) and the compressive strength that fall within the order of the corresponding properties of the human cancellous bones. The elastic modulus and compressive strength for certain types of human cancellous bone is approximately 10–190 MPa and 0.25–35 MPa, respectively [43]. This present study aims at exploring the corrosion time-dependent mechanical properties and architectural features of open cell iron

foams with hollow struts, and at presenting a computational methodology to estimate the mechanical properties of absorbable scaffolds based on their post-corrosion microarchitectures. At first, *in vitro* static immersion tests in a simulated biological environment up to 14 days were conducted, followed by mass measurements, uniaxial compression tests, and microarchitectural elucidation by using micro-computed tomography (μ CT) and scanning electron microscopy (SEM) imaging. Then, *in silico* compression tests on idealized Kelvin cellular structures [55, 56] were conducted in the FE framework by assuming an elastic-perfectly plastic constitutive material model. The predicted mechanical properties after 14 days of immersion are compared against the experimental results. Eventually, to understand the effect of a homogenous corrosion, a modified Kelvin foam model was developed and underwent the same FE analysis.

3.2. Materials and methods

3.2.1. Sample preparation

Open cell pure iron foams with a nominal cell size of 800 μm and hollow struts were provided by Alantum, Korea. The iron foams were manufactured through the replication of polyurethane (PU) foams where pure iron is electroplated on PU foam which was made conductive in advance by deposition of a thin Ni layer. After electroplating and heat treatment processes, the PU precursor was pyrolyzed and the remaining iron foam was annealed resulting into an open cell iron foam with hollow struts. More details on the foam fabrication process can be found in reference [42]. A SEM image (Quanta 250 FEI, Hillsboro, OR, USA) of the foam microstructure along with the geometrical definitions are demonstrated in Figure B.1 of the Appendix. Relative density of the foams was determined as the ratio of the foam density to the density of the cell-wall material, i.e. iron (7.874 g/cm^3). The foam densities were calculated through measuring the foam dimensions with a caliper to obtain the bulk volume and measuring the mass on a scale. Specimens were prepared in two steps: (i) long rectangular prisms with a nominal width of 10 mm were cut from iron foam sheets of 2.4 mm nominal thickness using a rotatory saw (Bosch 4310 with Dewalt DW3106 blade) and (ii) rectangular prisms were cut into $10 \text{ mm} \times 10 \text{ mm} \times 2.4 \text{ mm}$ cuboid specimens using a Dremel rotatory cutting tool.

3.2.2. Immersion tests

Static immersion tests were conducted for 1, 3, 5, 7, 10 and 14 days (the immersed samples are 1d, 3d, 5d, 7d, 10d, and 14d). Before immersion, samples were ultrasonically cleaned first in acetone for 3 min and then in ethanol for 1 min, and they were stored in the desiccator for subsequent mass measurement. Iron foam specimens were immersed in Hanks' solution (H1387, Sigma Aldrich, Saint Louis, MO, USA) without adding sodium bicarbonate. The solution was prepared by dissolution of 9.75 g of the Hanks' salts in 1 L of nano-pure water; the pH of the solution is adjusted at 7.4. Specimens were immersed in closed bottles containing 100 mL of the prepared solution. They were hung from a wire passing through a small hole at the middle of the bottle caps. During immersion, the bottles were kept in an incubator at a temperature of 37 °C with 5% CO₂ concentration. At the end of each immersion time point, samples were removed from the incubator and stored in a desiccator. One day after removing the immersed samples, they underwent a cleaning process (6 specimens in each sample) as follows: ultrasonically cleaning in acetone and ethanol for 3 times: (the samples would be cleaned in acetone for 10 min and then in ethanol for 10 min; this process would be repeated two more times and each time with fresh acetone and fresh ethanol). After cleaning, samples were stored in the desiccator for subsequent dimensional and mechanical characterizations. Prior to performing the mechanical characterization, the mass and the volume of the corroded cleaned samples were obtained for density calculations. The mechanical compression tests were carried out the next day after cleaning. The mass of each specimen was measured in three stages: before immersion (*bi*), after immersion and before cleaning (*ai-bc*), and after immersion and after cleaning (*ai-ac*). Mass gain/loss and total mass-change percentages were calculated according to the following relationships:

$$\text{Mass gain/Mass loss/Total mass change} = (M_2 - M_1)/M_1 \quad (3.1)$$

Where M_2 and M_1 were determined as: $M_2 = M_{ai-bc}$ and $M_1 = M_{bi}$ (for mass gain); $M_2 = M_{ai-ac}$ and $M_1 = M_{ai-bc}$ (for mass loss); and $M_2 = M_{ai-ac}$ and $M_1 = M_{bi}$ (for total mass change).

3.2.3. Material characterization

The presence of corrosion products and their elemental composition was studied using the SEM and Energy-dispersive X-ray spectroscopy (EDS, SwiftED 3000, Oxford Instruments, Concord, MA, USA), respectively. Given that the focus of this study was on the architectural/mechanical characteristics of the samples, the results of EDS analysis are only available in Figure B.6 of the Appendix.

3.2.4. Mechanical tests

Samples of the corroded and cleaned specimens underwent a uniaxial compression test with a crosshead speed of 0.001 mm/s using an Instron machine (Instron 5944, Instron, Norwood, MA, USA) with a 2 kN load cell. Each sample contained four specimens. No lubrication is applied on the compression plates. From the stress-strain curves, the quasi-elastic gradient (QEG), yield strength (σ_y), compressive strength (σ_c) and energy absorbability up to 50% of strain (W) were calculated for each specimen using OriginPro 2020 (OriginLab, Northampton, MA, USA). Also, σ_c was defined as the first local maximum of stress after yielding; QEG was defined as the slope of the linear fit of stress-strain curve from σ_{30} to σ_{75} that was corresponding to 30% and 75% of σ_c , respectively. Yield strength was also approximated by using 0.2% offset method [140]. The energy absorbability was considered as the area underneath the stress-strain diagram from $\varepsilon = 0$ to $\varepsilon = 50\%$ [139] where $\varepsilon = 0$ was defined as the intersection of the extension of the quasi-elastic region (its linear fit) and the horizontal axis.

3.2.5. Ashby-Gibson models for elastic modulus and plastic collapse stress of open cell foams

To better understand the effect of adherent corrosion products on the mechanical properties of the iron foams, the experimental values for QEG and compressive strength of corroded iron foams were compared against their corresponding values predicted by the theoretical models proposed by Ashby and Gibson [99, 122]. The *elastic modulus* and the *plastic collapse stress* of open cell foams with low relative densities (*bending-dominant cellular materials*):

$$\frac{\bar{E}}{E_s} = C_1 \left(\frac{\bar{\rho}}{\rho_s} \right)^2 \quad (1.13)$$

$$\frac{\bar{\sigma}_{pl}}{\sigma_{ys}} = C_2 \left(\frac{\bar{\rho}}{\rho_s} \right)^{\frac{3}{2}} \quad (1.14)$$

where \bar{E} and E_s represented elastic modulus of the foam and the parent material, respectively; $\bar{\sigma}_{pl}$ and σ_{ys} were also the plastic collapse stress of the foam and the yield stress of the parent material, respectively. In addition, $\bar{\rho}$ and ρ_s were the density of the foam and the parent material, respectively, while C_1 and C_2 were constants depending on the microarchitectural features of the foam. For the sake of the qualitative comparison, it was assumed that E_s , ρ_s , σ_{ys} , C_1 and C_2 remained constant during corrosion. The models were used to predict \bar{E} (QEG) and $\bar{\sigma}_{pl}$ (compressive strength) of the corroded foams with respect to the average of those for the control (*non-immersed*) sample. The average values of density, QEG and the compressive strength of the control sample were assumed as $\bar{\rho}$, \bar{E} and $\bar{\sigma}_{pl}$, respectively. Then, to predict the quasi-elastic gradient and plastic collapse stress of the corroded foams, it sufficed to replace $\bar{\rho}$ in Eq. 1.13 and 1.14 with the density of the corroded specimens by assuming that the power laws in Eq. 1.13 and 1.14 remained unchanged for corroded and uncorroded samples.

3.2.6. Measurement of architectural parameters

3.2.6.1. Strut cross-sectional parameters

The strut thicknesses of the iron foams were estimated using μ CT data of one control and one cleaned 14d specimen (Skyscan1172, Bruker, Santa Barbara, CA, USA) operated with source voltage of 70 kV, source current of 141 μ A, rotation step of 0.3° and pixel size of 2.25597 μ m. Due to the required high resolution, the specimens' dimensions should be reduced to be able to include the entire volume of the specimens in the scans. Therefore, they were manually cut using a scalpel prior to being scanned. To identify the variations of the architectural parameters within the volume, both control and 14d specimens were virtually divided into four layers from the top surface downward, and each layer is divided into three

virtual sublayers. Therefore, the architectural measurements were conducted within layers and/or sublayers. Figure 3.1 demonstrates a 3D reconstructed model of the control foam in Dragonfly software (Dragonfly, Object Research Systems (ORS) Inc., Montreal, Canada) along with the layer/sublayer divisions.

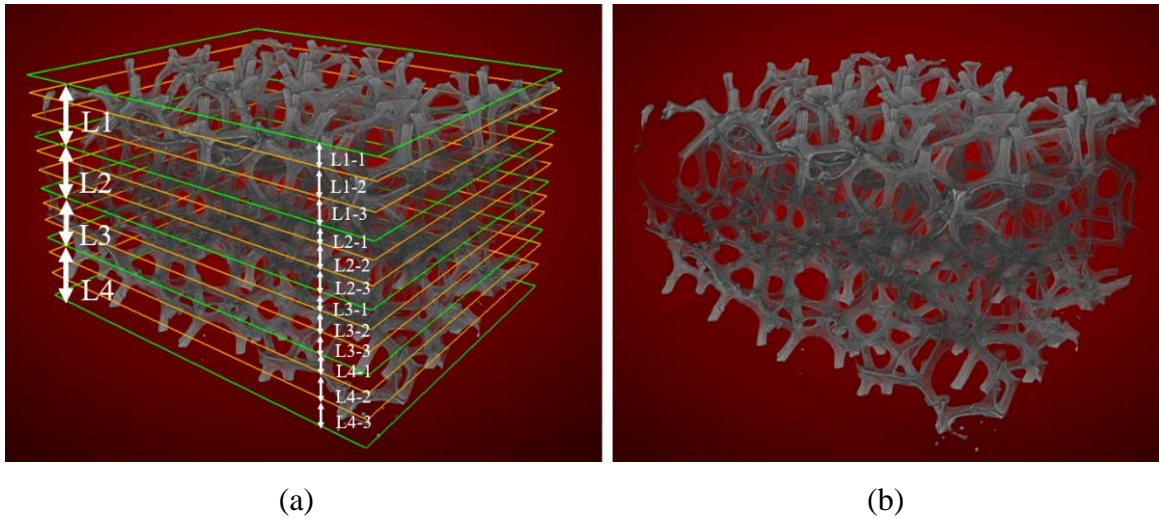


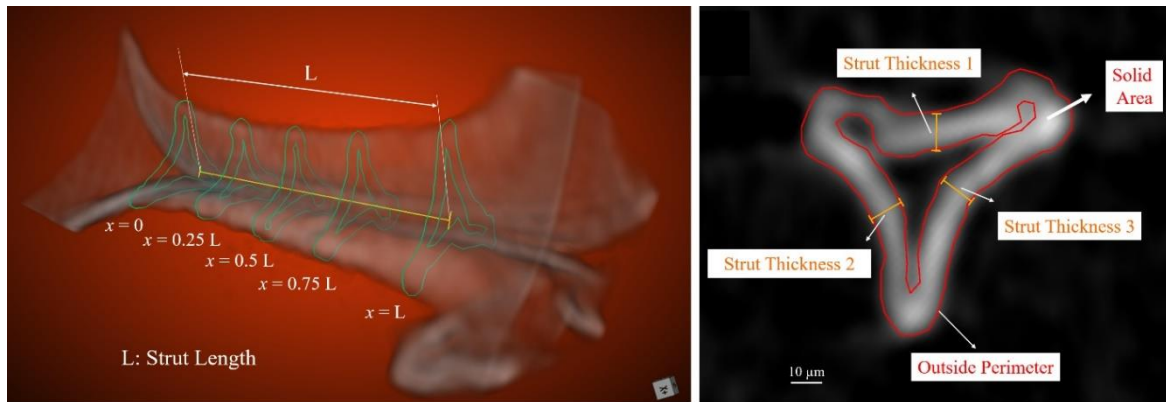
Figure 3.1- (a) (sub)layer division for μ CT analysis, (b) 3D reconstructed model of an iron foam (control specimen)

Two types of architectural analyses were conducted: whole-body and the single-strut analysis. In the whole-body analysis, the thickness of the struts in a region of interest (ROI) was estimated using the BoneJ plugin of ImageJ (NIH, Bethesda, MD, USA) where analyses were conducted within layers and within sublayers [157, 158]. For single-strut analysis, the Dragonfly software was utilized to estimate the architectural parameters of the single struts that were virtually cut from the reconstructed models. In the whole-body analysis, all the measurements were performed in cuboid regions of interests (ROI). The ROI configurations are provided in Table B.1.

The lengths and the widths of the ROI cuboids for the control and the 14d specimens were $4061 \mu\text{m} \times 2707 \mu\text{m}$ and $2707 \mu\text{m} \times 2256 \mu\text{m}$, respectively. Prior to the whole-body measurements, the stack of 2D slices were converted to 8-bit images, and they got segmented using the IsoData (iterative intermeans) thresholding algorithm [159] that was the default auto-thresholding method in ImageJ. The measured parameter using BoneJ was trabecular thickness (Tb.Th) that considered the local thickness at a point as the diameter of the largest

sphere that fit inside the structure and contained that point [160]. The estimated Tb.Th values were referred as strut thickness.

For single-strut analysis, 24 single struts were selected from each 3D reconstructed μ CT models of the control and 14d specimens (6 struts from each layer). It was tried to choose the struts with different lengths and from different regions within a layer. The length of the strut (L), parallel to the estimated longitudinal axis, was defined as the distance between the two ends located in the vicinity of the nodes. The end locations were visually estimated. After determining the end points of the struts (Figure 3.2a), the following cross-sectional parameters were estimated at key locations of the struts: Strut thickness and Solid area of cross-sections (Figure 3.2b). The thickness of a hollow strut was considered as the average thickness of five cross-sections measured at the key locations (Figure 3.2a). The thickness at a cross-section was defined as the average value of the three thickness measurements (approximately at the middle of each side) on the cross-section (Figure 3.2b).



(a)

(b)

Figure 3.2- (a) 3D reconstruction of a single strut with the key locations where the cross-sectional measurements are conducted, and (b) Strut cross-sectional parameters

3.2.6.2. Pore size analysis

To investigate the effect of corrosion on the pore sizes of the periphery regions of the foams, the pore sizes of the control and the 14d samples (2 specimens per sample) were determined using SEM images and were compared against each other. Each pore area was selected using the Wand tool in ImageJ, and then the area was measured. The area of 160 and 156 pores were estimated on the control and the 14d samples, respectively. After obtaining the area,

pore size was determined as the diameter of the equivalent circle with an area equal to that of the pore by:

$$Pore\ size = 2 \times \sqrt{\frac{Pore\ area}{\pi}} \quad (3.2)$$

Therefore, pore size values only depend on the measured pore areas, and they are independent of the pore shapes.

3.2.7. Computational modelling

Using the geometrical data obtained from the μ CT measurement, a finite element model with ideal Kelvin cell architecture was developed. Kelvin cell, a truncated octahedron with 8 hexagonal and 6 quadrilateral faces [55], has been used in the literature as an ideal model for open cell foams [130, 134, 161, 162]. It is a simple yet satisfactorily accurate model to predict the elastic properties and compressive strength of the open cell foams [130, 131]. The Kelvin foam CAD models representing the control and 14d samples are developed in SolidWorks Pro 2019 SP4.0 (Dassault Systemes SolidWorks Corp., Waltham, MA, USA), based on single-strut measurements conducted in the Dragonfly software. The models (henceforth referred as Kelvin-Control and Kelvin-14d) were then exported to Ansys Workbench 19.1 (ANSYS Workbench Platform, Wilde Analysis Ltd., Cheshire, UK) for finite element modelling (FEM) wherein the conditions of the compression tests were simulated (*in silico* tests). The iron foam control and 14d samples were referred as Control-Experiment and 14d-Experiment to conveniently distinguish between the computational model and experimental results. When comparing the mechanical properties obtained by experiments and FEM, the quasi-elastic gradient and compressive strength are referred as *elastic parameter* and *strength parameter*, respectively.

3.2.7.1. Kelvin-cell model

The struts of the Kelvin models had hollow equilateral triangular cross-sections (Figure 3.3a) whose areas vary along the length (Figure 3.3b). All the struts in a Kelvin cell were symmetric with respect to their middle plane located at $x = 0.5L$ (Figures 3.2a and 3.3b). Each Kelvin-cell contains two groups of struts: periphery struts (blue struts in Figures 3.3c and d) and core

struts (red struts in Figures 3.3c and d). The dimensions of the periphery struts were based on the μ CT measurements of the struts in the periphery layers of the foams (L_1 and L_4 in Figure 3.1a), while the core struts were designed based on measurements associated with their core layers (L_2 and L_3 in Figure 3.1a). The design steps of the Kelvin struts are explained in section B.2 of the Appendix.

The strut length and axis length (Figure B.2) in all struts of Kelvin foams were considered 223.5 μm and 393.5 μm , respectively. Single Kelvin-Control and Kelvin-14d cells were tessellated to create $3 \times 3 \times 2$ K foams. The dimension of both Kelvin foams was 3.339 mm \times 3.339 mm \times 2.226 mm. After following the procedure explained in section B.3 of Appendix, the following nominal strut thicknesses (t) were obtained: 19.32 μm for Kelvin-Control periphery struts, 11.53 μm for Kelvin-Control core struts, 13.25 μm for Kelvin-14d periphery struts and 11.21 μm for Kelvin-14d core struts. The relative densities of the Kelvin-Control and Kelvin-14d foams were 2.625% and 1.905%, respectively. The average relative density of Experiment-Control and Experiment-14d samples were 3.01% (12.8% difference with that of the Kelvin-Control foam) and 1.97% (3.3% difference with that of the Kelvin-14d foam), respectively. This shows an acceptable proximity between relative densities of Kelvin foams and their corresponding foams used in the experiment.

To design the Kelvin-14d-HC foam (the model that represents homogeneous corrosion), the outside length (l_o) and the thickness (t) values of the strut cross-sections (at key locations) of the Kelvin-Control foam were reduced in a way that their inside length (l_i in Figure 3.3a) values remain almost unchanged. This would resemble the condition in the uniform corrosion when the outer surfaces uniformly dissolve. For both groups of the struts (periphery and core), l_o and t of triangular cross-sections were reduced by 12.80 μm and 3.70 μm , respectively. So, the nominal periphery and core strut thicknesses in Kelvin-14d-HC became 15.63 μm and 7.84 μm , respectively, and RD was 1.905% (almost equal to that of Kelvin-14d foam). More details on dimensions of the developed Kelvin foams are available in Table B.2 of Appendix.

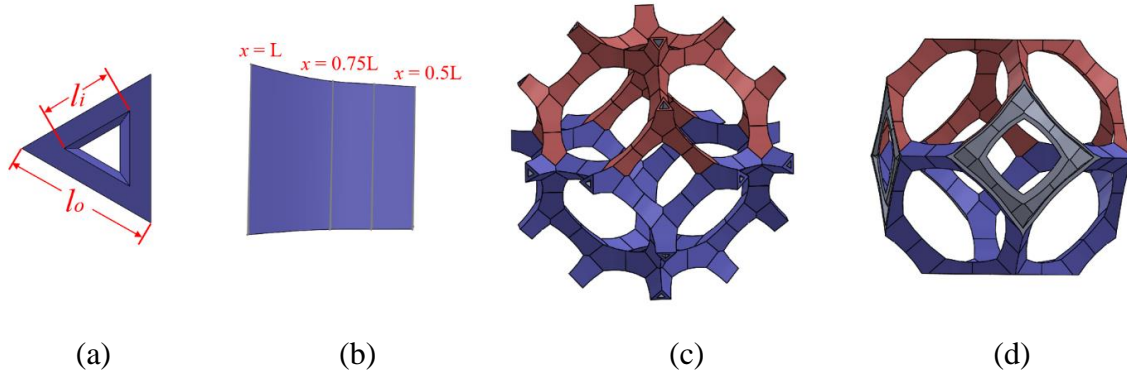


Figure 3.3- (a) Kelvin strut cross-section, (b) Half-strut with a varying cross-section, (c) Single porous Kelvin cell with hollow struts and (d) the Kelvin cell suitable for tessellation.

3.2.7.2. Finite element simulation

The $3 \times 3 \times 2$ K foams (18 cells in each Kelvin foam) were imported to Ansys Workbench to perform *in silico* compression tests within the static structural module. Compression was applied by defining vertical displacement of the compression plate (remote displacement). A frictionless contact was defined between the bottom surfaces of the compression plate and top surfaces of the Kelvin foams. The Kelvin foams had frictionless support on the ground. Two symmetry regions were defined on the sides (Figure B.4) to reduce the computational cost. Nonlinear Mechanical elements were used, and nonlinear analysis was adopted, i.e. Large Deflection option was enabled. Mesh sensitivity analysis was carried out for the 3 K models. The Kelvin-control, Kelvin- 14d and Kelvin-14d-HC models had 770899, 713426 and 794966 elements, respectively. The compression plate was considered to possess rigid-like material properties with an extremely high elastic modulus of 106 GPa. The Poisson's ratio for all materials was assumed 0.3. An elastic-perfectly plastic constitutive model was considered for the nonlinear finite element analysis. The stress response was considered as the force reaction at the frictionless support divided by the area of the Kelvin foams ($3.339 \text{ mm} \times 3.339 \text{ mm}$), and the strain was defined as the vertical displacement of the compression plate divided by the Kelvin foam thickness parallel to the loading direction (2.226 mm).

As defining the input material properties for the FE model, it was realized that if the Young's modulus of the base material was as high as the reported value for pure iron ($E \approx 200 \text{ GPa}$ [163]), the QEG of the Kelvin-Control foam would be extremely overestimated. Such stiffness overestimation in numerical models of a foam, when using the mechanical properties of the

base material, has been reported and it has been attributed to the presence of plastic deformations even at low stains [164]. It has been argued that the microstructure of struts and their porosity influence the overall stiffness of the foam [123]. Figure B.3 demonstrates the presence of micropores on the surface of two struts of iron foams used in this study. However, the overall strut microporosity was not very high, unlike those presented in reference [123]. One factor that significantly influenced the microstructure of struts was the manufacturing process of the foam. The open cell iron foam used in this study was fabricated by electroplating process [42]; it has been shown that choosing different electroplating parameters, i.e. plating temperature and current density, significantly affects the Young's modulus of thin films [165]. Therefore, fabrication process of iron foams could have had a role in decreasing the foam stiffness.

3.2.7.3. Determining the effective material parameters

Like the work in reference [164], instead of taking the Young's modulus of pure iron as an input material property, an *effective elastic parameter of material*, (E_{ef}), as well as an *effective yield parameter of material* (σ_{yef}) were introduced to reproduce the mechanical response of the Control-Experiment foam. To estimate E_{ef} , it substituted for E_s , the elastic modulus of the cell-wall material, in the following equation [123, 153]:

$$\left(\frac{\bar{E}}{E_s}\right) = f_1 C_1 \left(\frac{\bar{\rho}}{\rho_s}\right)^2 \quad (2.1)$$

This equation is the modified version of Eq. (1.13) for open cell foams with hollow struts, where coefficient f_1 , was the enhancement function of the Young's modulus [153], and it depended on the hollowness of the strut; it was obtained by the following equation:

$$f_1 = \frac{1+r^2}{1-r^2} \quad (2.3)$$

where r was the ratio of the inside length of the hollow strut cross-section (l_i in Figure 3.3a) to its outside length (l_o in Figure 3.3a), i.e. $r = \frac{l_i}{l_o}$. Given that the cross-sectional dimensions

vary along the strut length, r value then changed along the strut length. Therefore, li and lo values at multiple cross-sections of periphery and core Kelvin-Control struts were measured in SolidWorks, and r and f_l were calculated for each of them. For a strut, f_l was estimated as the mean of the calculated values of its cross-sections. Eventually, for the whole Kelvin-Control structure, the weighted average of f_l values associated with its struts was placed in Eq. (2.1) according to the number of periphery and core struts in a single cell, i.e. 20 and 16, respectively.

Coefficient C_l in Eq. (2.1) depends on the geometry of the cells and struts [56, 122]; it was also influenced by strut microstructure and porosity [123]. Various experimental data related to open cell polymeric foams has shown $C_l \sim 1$ [122]. So, $C_l = 1$ was considered for the Kelvin-Control foam. The average elastic parameter (QEG) of the Experiment-Control sample (8.13 MPa) was considered for \bar{E} ; $\left(\frac{\bar{\rho}}{\rho_s}\right)$ was substituted with the relative density of the Kelvin-Control foam that was 0.02625. To estimate the σ_{yef} value, it substituted for σ_{ys} , the yield stress of the cell-wall material, in the following equation [153]:

$$\left(\frac{\bar{\sigma}_{pl}}{\sigma_{ys}}\right) = f_2 C_2 \left(\frac{\bar{\rho}}{\rho_s}\right)^{\frac{3}{2}} \quad (2.2)$$

This equation is the modified version of Eq. (1.14) for open-cell foams with hollow struts, where f_2 was the enhancement function for plastic collapse stress [153] obtained by the following equation [153]:

$$f_2 = \frac{1-r^3}{(1-r^2)^{\frac{3}{2}}} \quad (2.4)$$

where r was the same ratio defined for Eq. (2.3). We should note that although Eq. (2.4) is not analytically correct for f_2 values of triangular cross-sections, it can still provide an adequate estimation for equilateral triangular cross-sections [153]. The procedures for assignment of f_2 for a strut and for the whole Kelvin-Control structure are the same as those

explained for assignment of f_1 . Coefficient C_2 in Eq. (2.2) depended on the cell architecture; $C_2 \sim 0.3$ provided a good fit for various pieces of experimental data [122]. However, for the model used in this work, the strength parameter of the Kelvin-Control agreed better with that of the Experiment-Control for $C_2 = 0.47$. As a result, the value of 0.47 was adopted based on the analysis made in reference [166]. The average strength parameter (compressive strength) of the Experiment-Control sample (0.382 MPa) was considered for $\bar{\sigma}_{pl}$. Finally, using Eqs. (2.1) and (2.2), the following values were calculated for the effective material parameters of the Kelvin foams: $E_{ef} = 6155.99$ MPa and $\sigma_{yef} = 133.05$ MPa. Table 3.1 summarizes the parameters and the methods implemented for determining the effective material parameters.

Table 3.1- Summary of the parameters and the methods by which their values are obtained

Parameter	Value	Method to obtain the value
f_1	1.917	f_1 for Kelvin-Control periphery and core struts are determined and the weighted average is placed in Eq. 2.1
C_1	1	Reference [122]
f_2	1.436	f_2 for Kelvin-Control periphery and core struts is determined and the weighted average is placed in Eq. 2.2
C_2	0.47	Reference [166]
$\left(\frac{\bar{\rho}}{\rho_s}\right)$	0.02625	The relative density of the Kelvin-Control foam
\bar{E}	8.13 MPa	Average elastic parameter (QEG) of the Experiment-Control sample
$\bar{\sigma}_{pl}$	0.382 MPa	Average strength parameter (compressive strength) of the Experiment-Control sample
E_{ef}	6155.99 MPa	Substituting E_{ef} for E_s in Eq. 2.1
σ_{yef}	133.05 MPa	Substituting σ_{yef} for σ_{ys} in Eq. 2.2

After obtaining the results of *in silico* tests, the elastic parameter of the Kelvin foams was obtained by the same method used for determining QEG of the Experiment foams. The strength parameter of the Kelvin foams was considered as the maximum stress value on their stress-strain curves (Figure 3.11a).

3.3. Results and discussion

3.3.1. Immersion tests

Figure 3.4 a–d represent a control as well as uncleaned dry specimens after 3, 7 and 14 days of immersion; corrosion products on the specimens were present, and they were evenly distributed on the surface. Figure 3.4 b-d show that after 3 days of immersion, the corrosion products were light brown. After 7 days of immersion, the corrosion products had a reddish tone and after 14 days of immersion, they turned to dark brown with a reddish tone. After cleaning the corroded specimens, it was observed that as the immersion time increases, corrosion products tend to become less adherent and were easily removed by ultrasonic cleaning. In another study [16], α -FeOOH and γ -FeOOH were detected in non-adherent corrosion products of iron after 14 days of immersion in commercial and modified Hanks' solutions [16], thus it is likely that the non-adherent corrosion products in this study contain the same compounds. Figure 3.4 f-i depict the SEM images of corroded surfaces of the specimens after cleaning. It is evident that most of the struts of the depicted region of the 3d specimen were covered with the adherent corrosion products while many struts of the 14d specimen were almost as clean as those of the control specimen. That said, observation of the specimens (not shown in the figure) confirms that even the cleaned 14d specimens contained adherent corrosion products in their structures. The considerable presence of corrosion products on the 5d and 7d specimens was evident (Figure 3.4 g and h).

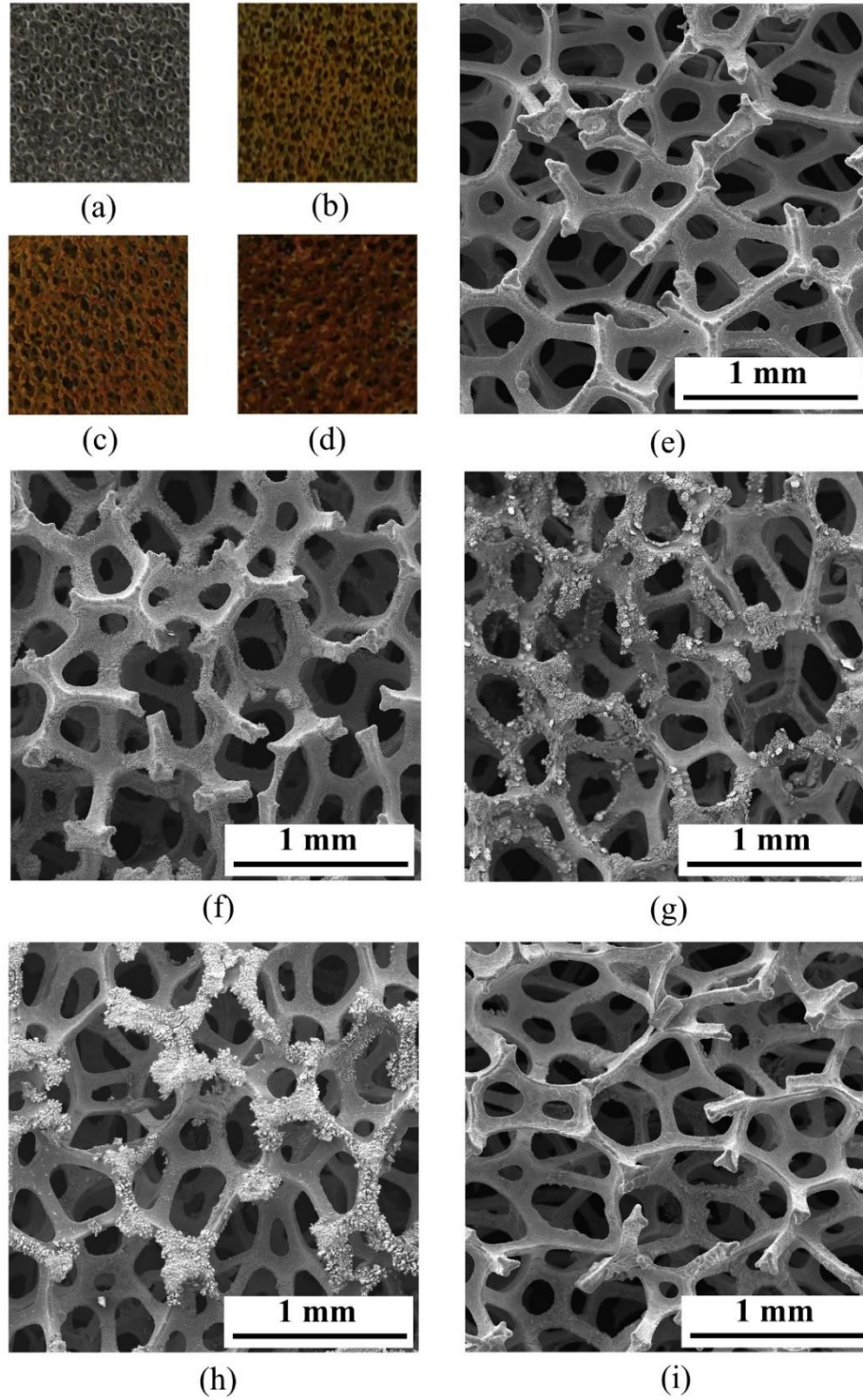


Figure 3.4- Surface of (a) control, (b) 3d, (c) 7d and (d) 14d corroded specimen before cleaning, and the SEM image of (e) control, (f) 3d, (g) 5d, (h) 7d, and (i) 14d corroded specimens after cleaning

To understand the corrosion effect on the core regions of the foams, uncleaned corroded samples were cut using scalpel for cross-sectional observations (Figure B.5 of the Appendix).

Interestingly, the core regions of all corroded samples were significantly less corroded than the periphery. Lower degradation of the core regions under static immersion has been reported for additively manufactured (AM) porous iron [23] and AM functionally graded porous zinc [15]. This may be due to the difference between the local pH of the core and periphery regions, stagnant flow at the central region [23], and/or low permeability of the porous structure. Permeability is one of the influencing factors on corrosion behavior of porous structures, and it is in a direct relationship with porosity [24]. According to μ CT measurements on the control specimen, the struts of the periphery layers had higher cross-sectional thicknesses and perimeters than those in the core layers. Thus, the local porosity between the struts of periphery regions should be lower than that in the core regions, resulting in decreasing the permeability of the iron foams. In addition, accumulation of corrosion products on the periphery layers could impede the solution access to the core regions (time dependent permeability)[23]. It is expected that under dynamic immersion, both periphery and core regions would highly corrode due to the flow of solution into the porous structure, generating higher volumes of corrosion products [15, 24].

Visual inspection of the cross-sections reveals that some struts of a cross-section significantly corroded while others remained almost intact (Figure B.5 a-d of Appendix). It suggests that corrosion rate of struts could be different, even if they were in a similar distance from the surface exposing to the solution. This may be due to the electrochemical heterogeneity within the structure of electrodeposited iron foams, making some struts more active than the others. Iron dissolution may also continue in the already corroded struts due to the galvanic reactions between the intact iron and its oxides/hydroxides [167].

3.3.2. Effect of corrosion on physical and mechanical properties of iron foams

Figure 3.5a shows a monotonic increase of mass-gain percentage up to 5 days of immersion and a sudden decrease after 7 days of immersion, possibly due to fallout of the highly accumulated surface corrosion products. The average mass-gain percentage of the 7d sample (5.72%) is very close to that of the 1d sample (5.74%). However, the average mass-loss

percentage after cleaning (Figure 3.5b) for the 7d sample (11.21%) is almost twice that for the 1d sample (5.69%), indicating that the portion of the non-adherent corrosion products on sample 7d was significantly higher than that on sample 1d.

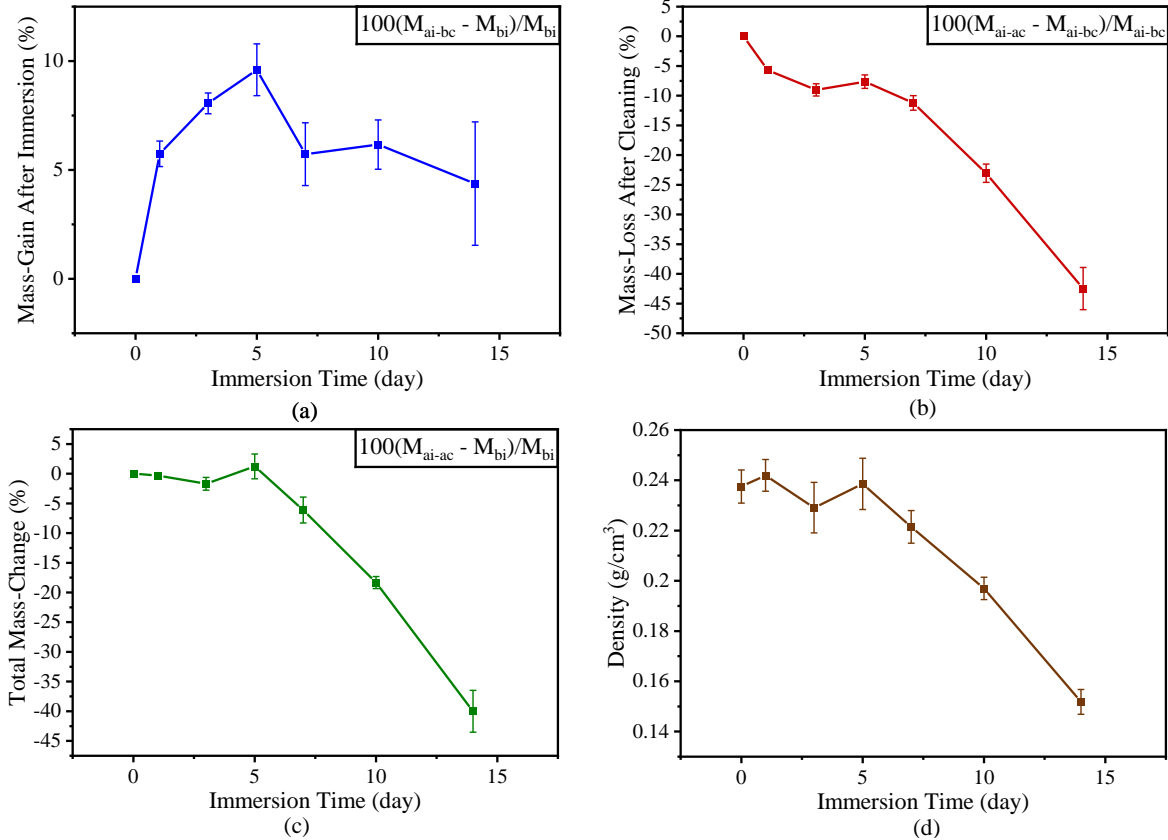


Figure 3.5- Effect of corrosion on the mass and the density of iron foams: (a) Mass-gain after immersion, (b) Mass-loss after cleaning, (c) Total mass-change after cleaning and (d) Foam density of the cleaned samples

The total mass-change of the corroded samples after cleaning with respect to their initial mass before immersion is demonstrated in Figure 3.5c. It indicates that the mass of the foams did not notably change after 1–5 days immersion although they were obviously corroded. However, a monotonic total mass loss was observed after 7 days of immersion onward. This suggests that the mass portion of the non-adherent corrosion products rapidly increases from sample 7d, and it continues after 14 days of immersion. Expansion of clean regions after 14 days of immersion is easily noticeable under the SEM observations. The variation of foam density with immersion time is depicted in Figure 3.5d; it shows a similar trend as that of the total mass-change. This is because the volume of the specimens after immersion does not

alter as much as the mass does, so the density changes are mostly controlled by the mass change. The average dimensions of the 14d sample changed from 9.69 mm × 9.49 mm × 2.415 mm before immersion to 9.41 mm × 9.29 mm × 2.365 mm after immersion and after cleaning. This indicates only 6.9% volume reduction after 14 days of immersion, which is significantly less than 40.0% mass reduction after this period. Table 3.2 contains the densities and mechanical properties of the control and corroded (for 7 and 14 days) iron foam samples obtained from the experimental tests. Pitting was observed on some struts of the corroded samples (Figure 3.6), which was expected to result from the presence of Cl⁻ ions in the solution that breaks down the passive layers and promotes the localized corrosion [16, 167].

Table 3.2- Density and mechanical properties of the control, 7-day and 14-day corroded iron foams determined from experimentation

	Control sample	7-day-immersed sample	14-day-immersed sample
Density (g/cm ³)	0.238 ± 0.007	0.221 ± 0.007	0.152 ± 0.005
QEG (MPa)	8.13 ± 2.15	6.60 ± 1.03	3.70 ± 0.30
Compressive strength (MPa)	0.382 ± 0.024	0.290 ± 0.021	0.162 ± 0.015
Yield strength (MPa)	0.335 ± 0.017	0.247 ± 0.027	0.140 ± 0.012
Energy absorbability (MJ/m ³)	0.237 ± 0.014	0.161 ± 0.010	0.096 ± 0.005

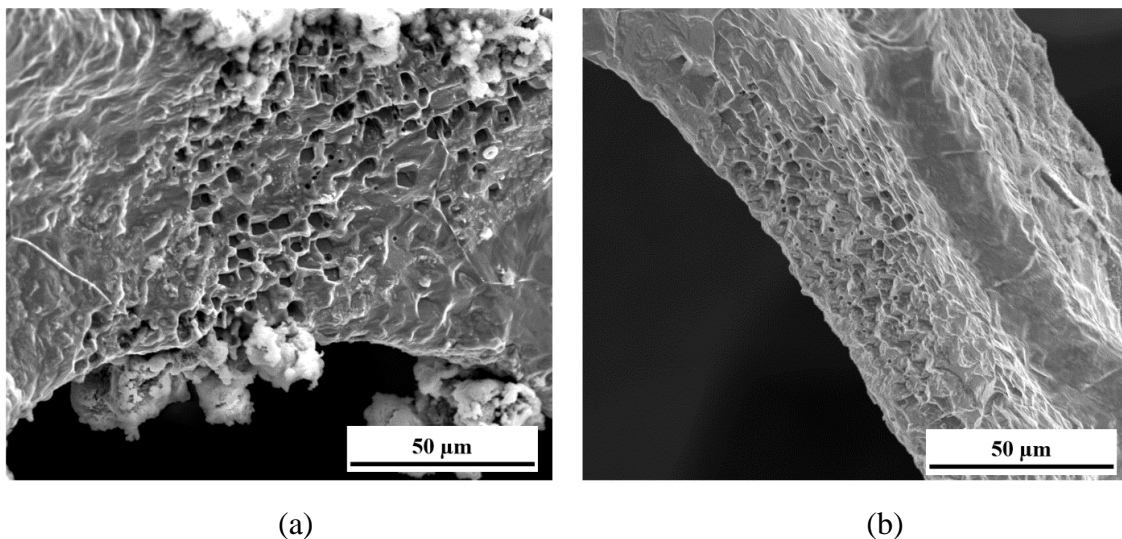


Figure 3.6- Presence of pits on a strut of (a) 7d and (b) 14d specimens.

The compressive response of all samples contains a quasi-elastic region followed by a plateau and densification. Figure B.7 of Appendix demonstrates the stress-strain responses of the control, 3d, 7d and 14d samples. The plateau for this kind of foam with a nominal cell size of 800 μm , is much longer than what was erroneously perceived in our previous work [19], suggesting that the plateau of other samples in reference were also mistakenly assumed as densification. Figure 3.7 demonstrates the variation of mechanical properties with immersion time. After 14 days of immersion, the average density, QEG, compressive strength and energy absorbability of the iron foams decreased by 36.1%, 54.5%, 57.6% and 59.5%, respectively. The experimental results show that, except for quasi-elastic gradient (QEG), the other mechanical properties experience a monotonic decreased with immersion time.

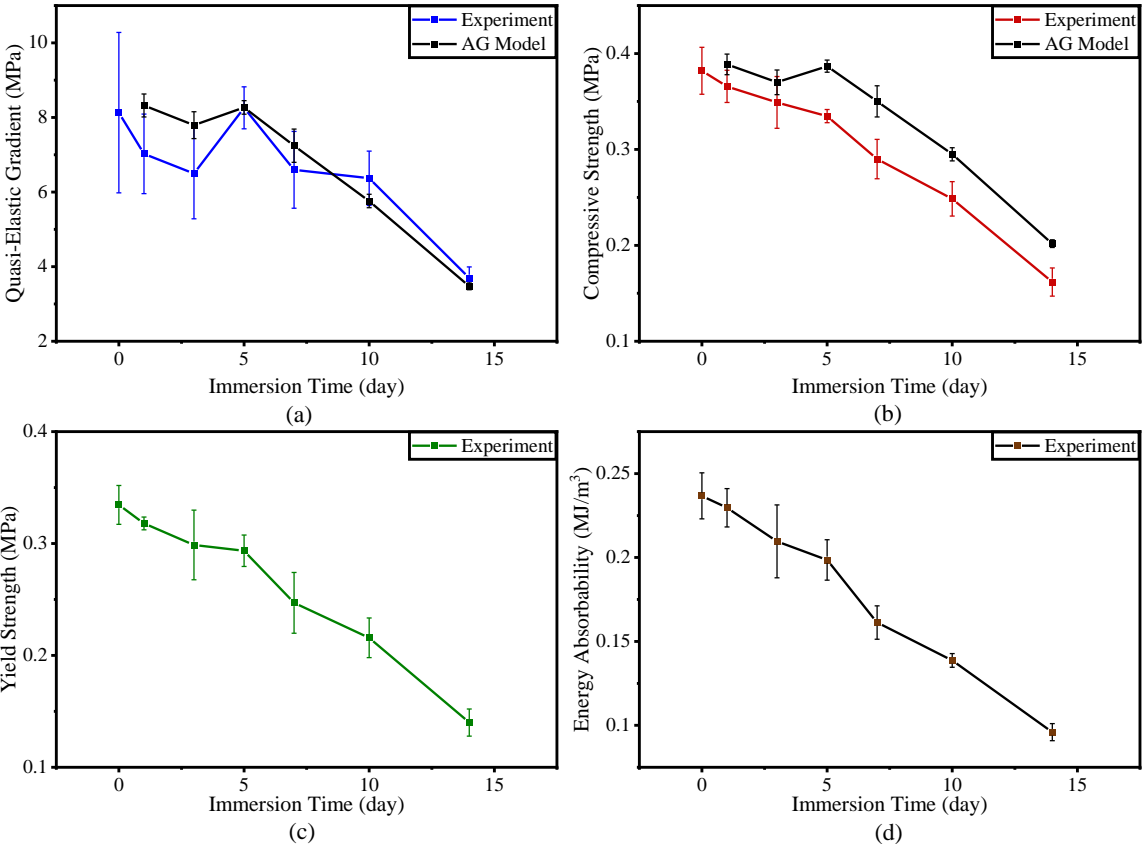


Figure 3.7- Variation of mechanical properties with immersion time: (a) Quasi-elastic gradient, (b) Compressive strength, (c) Yield strength, and (d) Energy absorbability.

As explained by Eqs. (2.1) and (2.2), the mechanical properties of foams depend on the base material of cell walls, cell geometries, strut hollowness and the relative density; having the

highest power in Eqs. (2.1) and (2.2), relative density is the most influential factor. Therefore, decreasing the density can lead to a reduction of the elastic modulus/ QEG and plastic collapse stress of the foams. The latter leads to lowering the plateau stress in the stress-strain diagram, thus reducing the area underneath the stress-strain curve that determines the energy absorbability.

The non-monotonic variation of QEG can be attributed to the presence of adherent corrosion products; in lower strains prior to yielding, the adhesion between the products and the intact iron was strong enough for corrosion products to carry the load. Therefore, by increasing the cross-sectional area, the stiffness of the strut enhances. However, as the compression strain increased, the adherent products would not resist as much against the load, so it was mostly the intact part of the struts that bear the load. Figures 3.7a and b compare the QEG and the compressive strength values obtained by experimental results and those predicted by AG model (Eq. 1.13 and 1.14). It is evident that for 5d and 7d samples, which had a high amount of adherent corrosion products, the difference between the AG predicted and experimental QEG values (0.11% for 5d and 9.79% for 7d samples) is significantly less than that of compressive strength values (15.6% for 5d and 20.7% for 7d samples). This indicates that the rise of density due to the presence of corrosion products effectively increased the QEG of the corroded foams unlike their compressive strength. Higher contributions of corrosion products in enhancement/ maintenance of stiffness (than that of yield/plateau strength) of corroded porous magnesium (WE43 [29] and AZ63 [28]) and iron [23] scaffolds has also been reported. In other studies, the presence of corrosion products produced under dynamic immersion has increased the yield strength of absorbable porous zinc scaffolds, even after 28 days of immersion [15, 33]; these improvements have been attributed to the high volumes as well as high hardness (which can be translated into sufficiently high strength) of corrosion products. The dynamically immersed porous zinc samples have also shown higher yield strength values than the statically immersed ones due to the greater volumes of corrosion products produced under dynamic condition [15, 33]. Thus, beside the strength of interfacial bonding between the corrosion products and the intact metal, the amount of corrosion products and their associated mechanical properties influence the mechanical behavior of absorbable metal scaffolds.

3.3.3. Effect of corrosion on architectural parameters of the foams

3.3.3.1. Strut thickness and cross-section surface area

Figure 3.8a shows the variation of the strut thickness along the depth (within layers) of the control and the 14d specimens. It also compares the results obtained by BoneJ and Dragonfly software. The strut thickness measurements within sublayers are provided in Table B.1 of the Appendix. It is evident that the struts in the periphery layers of the control specimen, i.e. L₁ and L₄, tend to be thicker than those in the core layers, i.e. L₂ and L₃. Moreover, after 14 days of immersion, only the thickness of struts in periphery layers was significantly reduced which was expected after cross-sectional observations of the corroded foams. Faster corrosion in the periphery layers than in center of porous iron was also reported in reference [23].

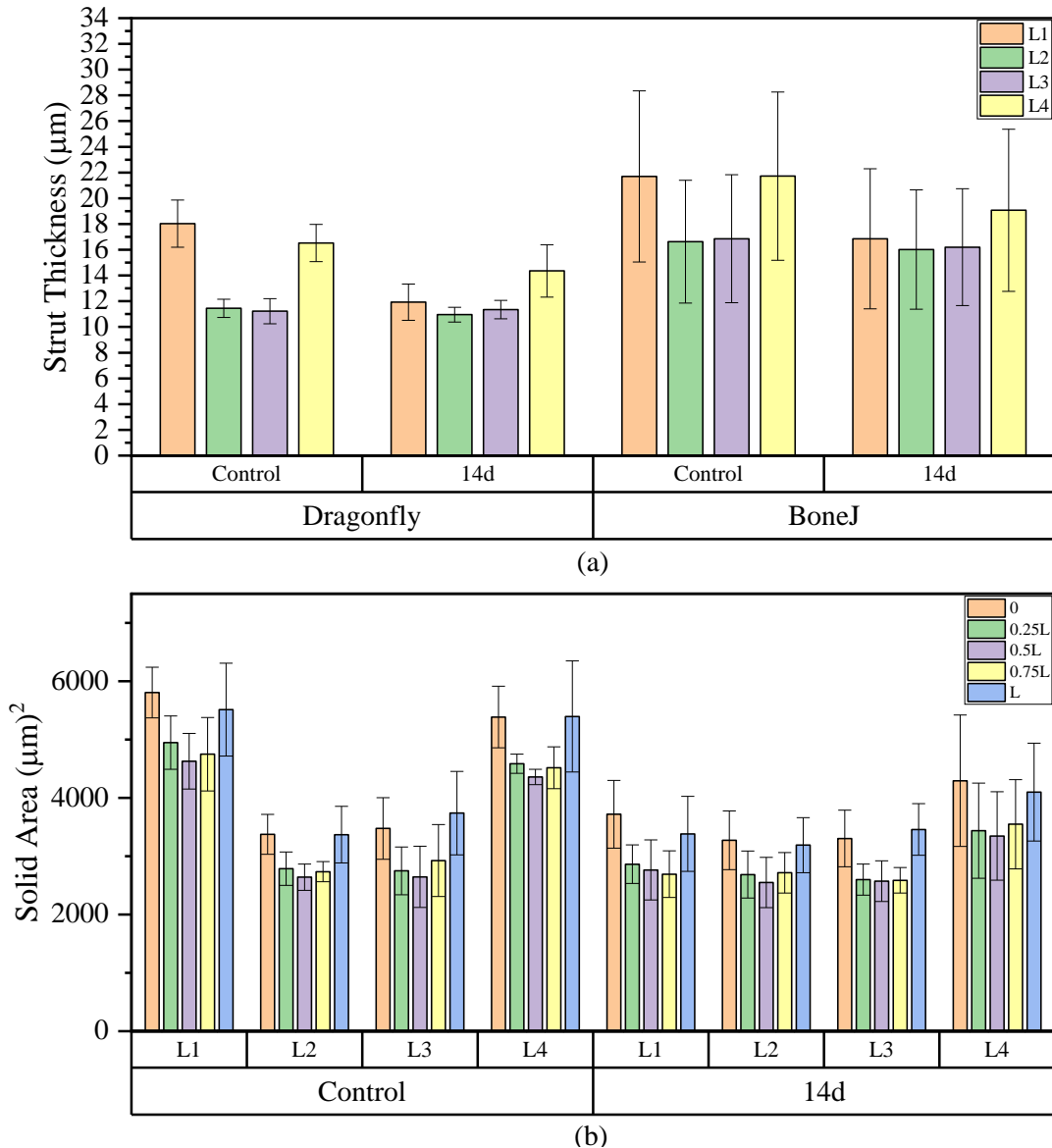


Figure 3.8- Variation of (a) strut thickness in the Control and 14d foam layers (b) cross-sectional solid area along the strut length in layers of the control and the 14d specimens.

Another observation from Figure 3.8a is that the thickness values estimated in BoneJ tend to be higher than those measured in Dragonfly. This could emanate from the effect of thresholding the μ CT images. However, the difference between the average strut thickness of the core and periphery layers, obtained by both methods, are notably close. The results of BoneJ and Dragonfly indicate that at L₁ layer, the average strut thickness of the control sample was 4.8 μ m and 6.1 μ m higher than that of the 14d specimen, respectively. The average thickness difference at L₄ was 2.7 μ m and 2.2 μ m according to the BoneJ and

Dragonfly results, respectively. Despite the considerable difference in the number of analyzed struts by each method, the proximity of the results demonstrates the validity of both techniques for comparative studies on the strut thickness of open cell foams with hollow struts.

The variation of the cross-section solid area (Figure 3.2b) along the length of the single struts within the specimens is presented in Figure 3.8b. As expected from Figure 3.2a, the area rapidly increases near the strut ends where it approaches the junctions. This is reflected in the area measurements for both specimens. Similar to the average strut thickness, the cross-sectional areas tend to be higher in the struts within periphery layers, i.e. L₁ and L₄, of the control specimen. In the 14d specimen, the surface area values in the periphery struts (at L₁ and L₄) approach toward those of the core struts (L₂ and L₃) that confirms that corrosion mainly takes place in the periphery regions.

3.3.3.2. Pore size

The distribution of pore size on the surface of the control and the 14d foam samples are presented in Figure 3.9. As shown by the normal distribution curves, after 14 days of immersion, the graph expands toward larger pore sizes that is expected to be the result of the thinning of the struts in the periphery layers; the mean pore size increases from 235.56 μm to 248.73 μm , i.e. 13.2 μm .

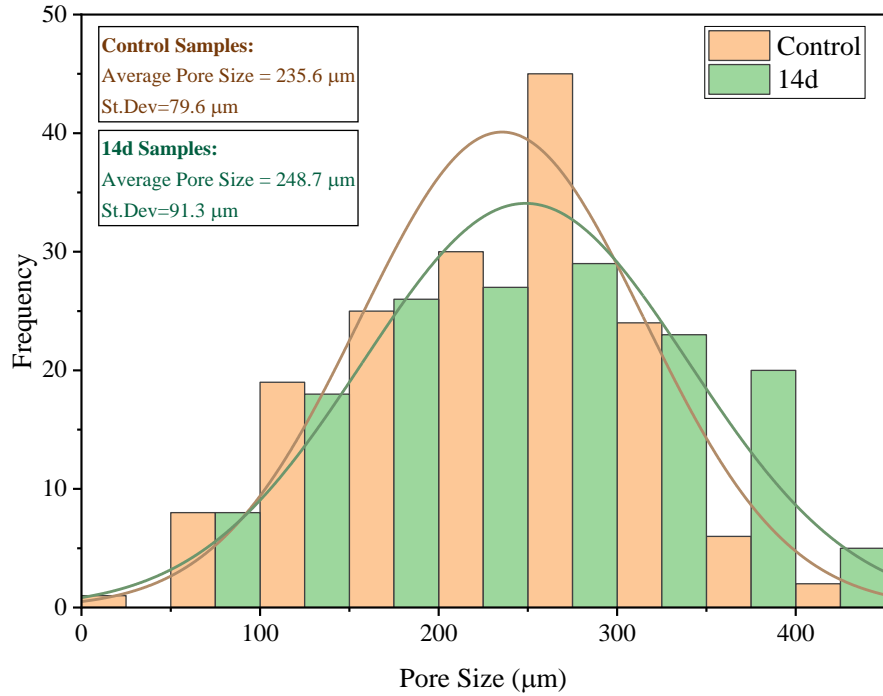


Figure 3.9- Distribution of pore-size on the surface of the control and the 14d foam samples.

3.3.4. Finite element modeling

The undeformed and deformed states of the Kelvin-Control foam simulated by finite element modelling (FEM) are depicted in Figure 3.10. Presence of stress concentrations within the junctions where the struts meet is evident in the shown stress contour.

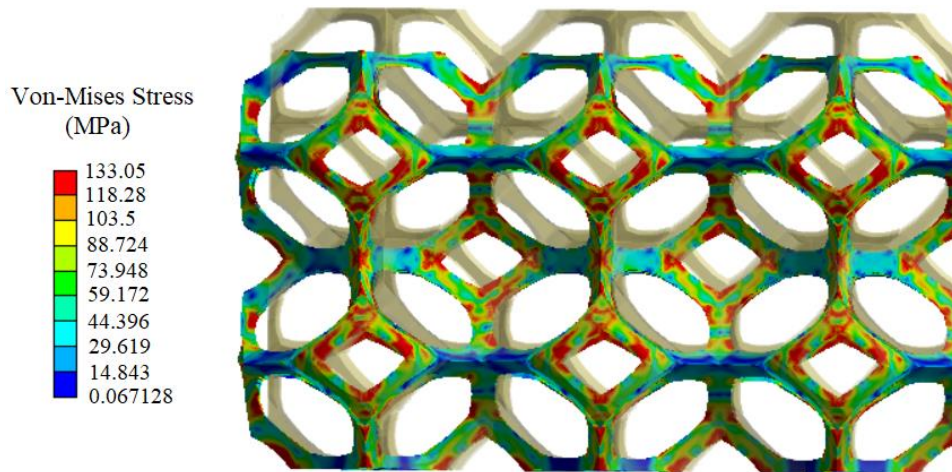


Figure 3.10- Control-Kelvin foam in undeformed and deformed states simulated by FEM

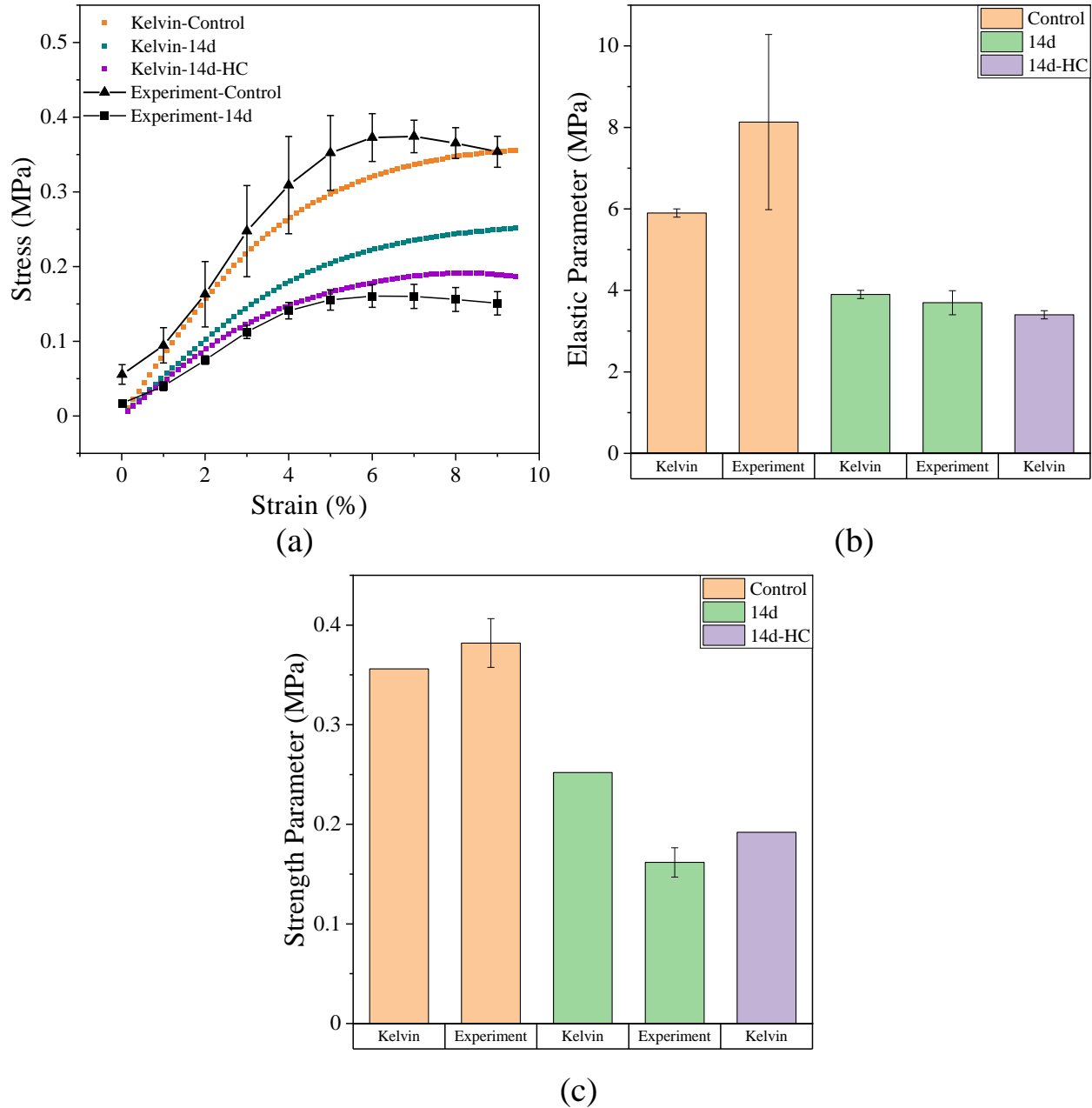


Figure 3.11- (a) Mechanical response (stress-strain curve) of Kelvin (FEM) and Experiment foams, and comparison of the b) elastic parameters and c) strength parameters obtained from the FE models and the experiments.

The mechanical properties of the Kelvin-Control, Kelvin-14d and Kelvin-14d-HC foams along with the experimental results are presented in Table 3.3 and the diagrams of Figure 3.11b and c. From Figure 3.11a, it is evident that the linear part of the mechanical response of the Kelvin control foam agreed very well with the initial part of the average mechanical response associated with the Experiment-Control sample (between 1% and 2% strain).

However, with the increase of strain, the mechanical response of the Kelvin-Control foam tends to become lower than the average of that for the Experiment-Control sample (until the strain of around 8.9%). Therefore, Kelvin-Control elastic parameter was significantly lower than the average value of that for the Experiment-Control sample (Figure 3.11b). However, as intended, the strength parameter of the Kelvin-Control is very close to the average of that for the Experimental-Control sample, with only 6.8% difference. It can be said that the Kelvin-Control foam properly reproduced the mechanical response of the Experiment-Control within the presented strain range.

Table 3.3- Mechanical properties of Kelvin foams and the corresponding experimental results

	Elastic Parameter (MPa)	Strength Parameter (MPa)
Kelvin-Control (FEM)	5.9 ± 0.1	0.356
Experiment-Control	8.13 ± 2.15	0.382 ± 0.024
Kelvin-14d (FEM)	3.9 ± 0.1	0.252
Experiment-14d	3.70 ± 0.30	0.162 ± 0.015
Kelvin-14d-HC (FEM)	3.4 ± 0.1	0.192

It is evident in Figure 3.11 a-c that the Kelvin-14d foam has a significantly lower value of elastic and strength parameters than those of the Kelvin-Control foam. However, the elastic and strength parameters of the Kelvin-14d foam are, respectively, 5.4% and 55.6% higher than their corresponding average experimental values. The overall lower mechanical response of the Experiment-14d sample can be observed in Figure 3.11a. The FEM results show that the model quite decently predicts the quasi-elastic response of the foam after 14 days of immersion, but it overestimates the plastic response. It is worth mentioning that due to its definition, the elastic parameter of Kelvin foams does not represent the slope of the most-linear part of their mechanical responses. The slope of the most-linear region of the stress-strain curves for the Kelvin-Control, Kelvin-14d and Kelvin-14d-HC were estimated as 8.1 MPa, 5.2 MPa and 4.6 MPa, respectively.

According to Figure 3.11 a, the stress response of the Kelvin-14d-HC foam is lower than that of the Kelvin-14d foam despite their almost-equal densities. The elastic and strength parameters of the Kelvin-14d-HC foam are 12.8% and 23.8% lower than those of the Kelvin-

14d foam, respectively. Dimensional and mass analysis reveals that although the core-struts in Kelvin-14d-HC foams have higher f_1 and f_2 enhancement coefficients than those of the Kelvin-14d foams (f_1 and f_2 of a single core-strut of the Kelvin-14d-HC cell is, respectively, 1.42 and 1.20 times as much as those of a core-strut in the Kelvin-14d cell), the mass of the Kelvin-14d-HC core region in a single cell is 0.71 times as much as that of the core region in a Kelvin-14d cell. This leads to a lower relative density in the core region of the Kelvin-14d-HC foam, causing it to be weaker than its corresponding region in the Kelvin-14d foam. The same analysis shows that the periphery regions of the Kelvin-14d-HC foam have higher mass and thus higher relative density than those of their corresponding regions in Kelvin-14d foam. Having a weaker core region makes the entire Kelvin-14d-HC structure more susceptible to failure under compression, leading to a lower mechanical response. This is in agreement with the results reported in reference [24], when the compressive properties of two types of functionally graded porous iron structures with similar total porosities were compared.

Comparison of the mechanical behavior of the homogeneously corroded and preferentially corroded models highlights the importance of considering corrosion mechanism when designing absorbable scaffolds; this is indispensable to offer desirable mechanical properties in porous materials during degradation.

3.4. Conclusions

Post-corrosion mechanical properties of open cell iron foams as absorbable bone scaffolds were studied, and the variation of architectural parameters after 14 days of immersion was investigated. Based on μ CT measurements, FE models for a control and 14-day-corroded specimens were developed based on Kelvin cells. The Kelvin foams undergo static compression (*in silico*) and their mechanical responses were compared against the experimental results. Eventually, using the FE modeling, the effect of a homogeneous corrosion (the corrosion mechanism that was not observed in the experiments) on the mechanical properties of a Kelvin foam was investigated. The following remarks are derived from the experimentation and computational study:

- Except for the quasi-elastic gradient, other mechanical properties, i.e. compressive and yield strength and energy absorbability, decrease monotonically with the immersion time.
- Adherent corrosion products enhance the load-bearing capacity of the open cell Fe foams in small strains.
- Using single-strut analysis of μ CT images, it is feasible to estimate the pre- and post-corrosion architectural parameters of the open cell iron foams with hollow struts, i.e. strut cross-sectional thickness and solid area. However, presence of corrosion products may introduce a challenge to distinguish between them and the intact iron in the μ CT images.
- Applying μ CT measurement to the Kelvin foam CAD model leads to a good representation of the control and 14-day-corroded foams in terms of relative density.
- The proposed FE Kelvin foam model decently predicts the quasi-elastic response of the 14-day-corroded iron foam. However, prediction of the plastic response should become more accurate.
- Homogeneously corroded Kelvin foam shows a significantly different mechanical response than that of the heterogeneously corroded one, despite almost equal relative densities.
- To offer desirable mechanical properties during degradation, it is crucial to consider the corrosion mechanism (homogeneous or heterogeneous) when designing absorbable metal scaffolds.

Conclusion

Biodegradable (absorbable) bone scaffolds are temporary implants that provide mechanical support and biological space for bone tissue regenerations (the terms “biodegradable” and “absorbable” were used interchangeably in the present thesis). During degradation, the scaffolds must provide sufficient mechanical support without failure as the result of the mechanical loads in the anatomic site. Porosity is an inherent characteristic of the scaffold structure which facilitate the tissue formation process. In the studies conducted for this PhD project, electroplated iron foam with hollow struts (manufactured by Alantum) was considered as a potential candidate for scaffolding applications, and the structural-mechanical properties relationships as well as the post-corrosion mechanical properties were studied.

In the first phase of the project, effects of different architectural properties, i.e. cell size, pore size and branch-strut thickness, on the mechanical properties of open cell iron foams were explored through compression tests. *In silico* compression tests (finite element analysis) were conducted on Kelvin foams to understand the influence of cell-size and strut hollowness level on the mechanical response of the cellular structure. The IF45 foam (450 μm cell size) with the highest relative density and the smallest pores demonstrated the highest yield and compressive strength values. Although the relative density of IF80 foams (800 μm cell size) was lower than that of IF45 foams, they indicated the highest quasi-elastic gradients. This was attributed to two possible reasons: *i*) IF80 struts having higher second moment of inertia (I) as the result of higher branch-strut thickness, *ii*) IF45 foams experienced more plasticity during quasi-elastic deformation due to stronger presence of structural inhomogeneities, or the influence of surface plasticity during loading is higher in IF45 foams due to their lower thickness.

In the next phase that was the focus of the project, detailed analyses of post-corrosion architectural and mechanical properties of the iron foams with hollow struts were conducted. Kelvin foam finite element models were developed to represent the control and the 14-day corroded iron foams; the strut dimensions were assigned based on μCT measurements. The models underwent *in silico* static compression. In addition, the influence of homogeneous

corrosion (the corrosion mechanism that was not observed in the experiments) on the mechanical properties of a Kelvin foam was explored. This study showed that adherent corrosion products significantly increase the stiffness of the degrading scaffold. Also, it confirmed that the micro-architectural features of the clean corroded foam, i.e. cross-sectional thickness and area of struts, can be successfully measured via micro-computed tomography and applied to Kelvin foam models to obtain a decent representation of the iron foam sample. Although pitting was observed on some struts during corrosion, the finite element Kelvin foam model with the assumption of uniform corrosion (no pitting) decently predicted the quasi-elastic response of the 14-day corroded foam. Yet, the assumption of uniform corrosion is a limitation of the presented model. The mechanical response of the homogeneously corroded Kelvin foam was significantly different from that of the heterogeneously corroded one, despite almost equal relative densities. This portrays the importance of considering the corrosion mode when designing the scaffolds.

One limitation of this research was the lack of 3D architectural data, e.g. μ CT measurements in the study presented in Chapter 2. Other limitations were as follows: static immersion condition and the produced Hanks' solution did not perfectly represent the physiological environment in the body. The low thickness of iron foam specimens could have introduced size effects in the compression tests. Only one type of mechanical characterization test (quasi-static compression test) was carried out in the experiments. Presence of a small amount of corrosion products on the 14-day corroded specimen could have, to some extent, influenced the μ CT architectural measurements. The regular Kelvin cell model with periodic structure did not perfectly represent the semi-random structure of iron foams. The material model in the FE model was simplified as the elastic-perfectly plastic, and the structural damages, e.g. fractures, were not considered in the model.

Future studies on mechanical behavior of absorbable metallic scaffolds, e.g. magnesium or zinc-based scaffolds, can take advantage of the results of the present study as a reference for comparison. In addition, studies under different experimental conditions for immersion or mechanical characterizations can compare their results with those of this study.

For future work, experimental conditions closer to the biological conditions of a specific anatomic site could be adopted. For example, suitable dynamic immersion apparatus, different immersion test solutions and longer test durations, and different mechanical characterization tests can be carried out, e.g. fatigue testing. Moreover, the interaction between the corrosion products and the intact metal as well as their role in the post-corrosion mechanical response of the scaffold can be explored in more details. The effects of mechanical properties of the corrosion products on the global mechanical response of the scaffold can be studied. The presented Kelvin model can be used to estimate the post-corrosion quasi-elastic response of other biodegradable open-cell bone scaffolds, e.g. Zn and Mg-based scaffolds, as long as the assumption of uniform corrosion is valid. The model can be developed further to include localized corrosion (pitting) to study its effect on the post-corrosion mechanical response of the metallic scaffolds. This may lead to better estimation of post-corrosion mechanical properties of the biodegradable open-cell metallic foams. Corrosion effects can also be introduced to other forms of finite element models of porous structures such as image-based models.

Appendix

A. Architectural features of the iron foam samples in the study presented in Chapter 2

A.1. Definition of architectural parameters

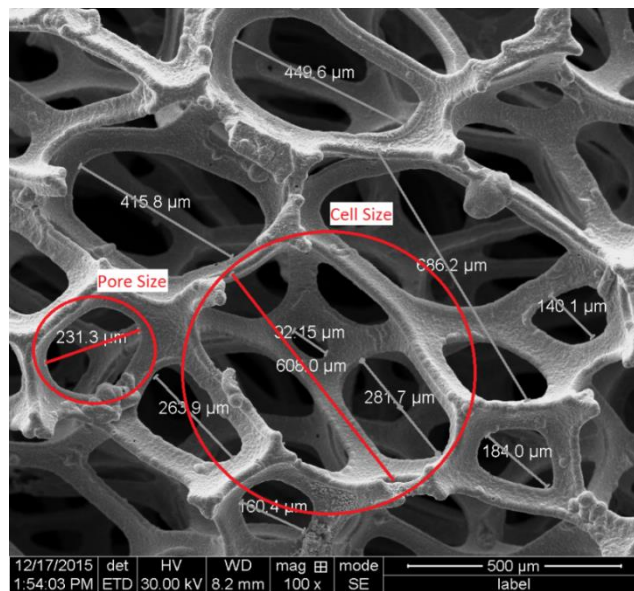


Figure A.1- Definition of cell size and pore size for the iron foams presented in Chapter 2

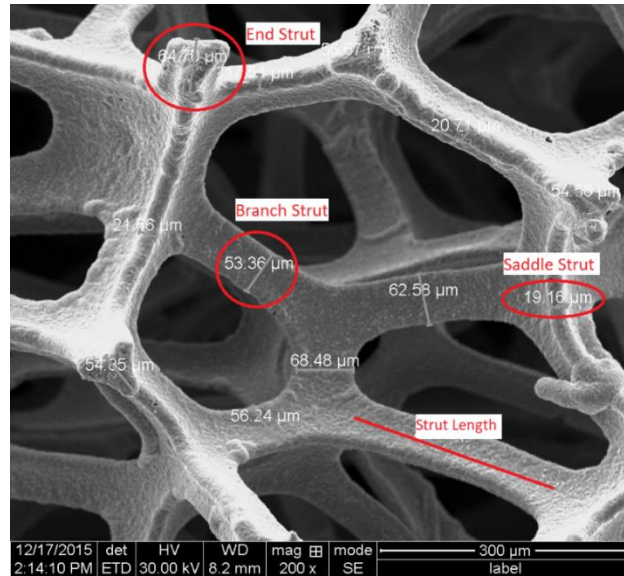


Figure A.2- Definition of different strut thickness parameters as well as the strut length for the iron foams presented in Chapter 2

A.2. Measurements of the architectural parameters on SEM images of the iron foams

Table A.1- Measurements of architectural parameters of the iron foams presented in Chapter 2

Fe foam type	Number of Measured Cells	Mean (μm)	SD	Min (μm)	Median (μm)	Max (μm)
IF45	81	461.77	72.26	275	455.5	641.3
IF58	113	617.73	76.08	433.6	601.9	836.2
IF80	45	828.11	79.87	691.2	805.2	1008
Cell size						
IF45	24	69.5	17.08	39.23	68.3	99.35
IF58	6	68.01	12.42	59.01	62.73	92.15
IF80	5	66.78	18.72	42.4	67.59	91.16
40 μm < Pore size < 100 μm						
IF45	43	155.20	28.89	102.3	154.75	199.9

IF58	31	150.8	29.43	101.2	150.5	198.9
IF80	29	157.33	28.5	100.5	164.8	198.3
100 μm < Pore size < 200 μm						
IF45	27	249.57	30.54	201.1	248.9	310.2
IF58	94	319.98	71.81	200.4	318.75	525.3
IF80	82	333.61	87.07	213	315.65	546.4
Pore size > 200 μm						
IF45	86	74.73	10.3	54.92	71.44	103.1
IF58	78	63.62	9.95	42.23	62.41	93.12
IF80	39	97.79	17.54	71.45	95.88	167.3
End strut thickness						
IF45	52	55.52	6.18	43.71	56.56	78.33
IF58	53	59.88	7.55	44.39	60.88	74.66
IF80	30	80.91	12.27	61.16	76.77	123.8
Branch strut thickness						
IF45	70	25.52	4.8	16.61	25.11	38.45
IF58	51	21.67	4.12	13.82	21.01	30.6
IF80	13	29.066	5.14	20.61	29.14	37.09
Saddle strut thickness						
IF45	76	156.40	39.41	91.74	149.89	259.60
IF58	76	197.81	56.08	92.11	201.56	357.84
IF80	76	215.97	55.31	116.17	212.40	365.04
Strut length						

B. Supplementary material of Chapter 3, post-corrosion mechanical properties of absorbable open cell iron foams with hollow struts

B.1. Geometrical and dimensional configurations of iron foams

Figure B.1 shows the cells, pores and struts of the iron foams used in this study. The dimension of sublayers, as depicted in Figure 3.1a of the manuscript, and the strut thickness values obtained by BoneJ are presented in Table B1.

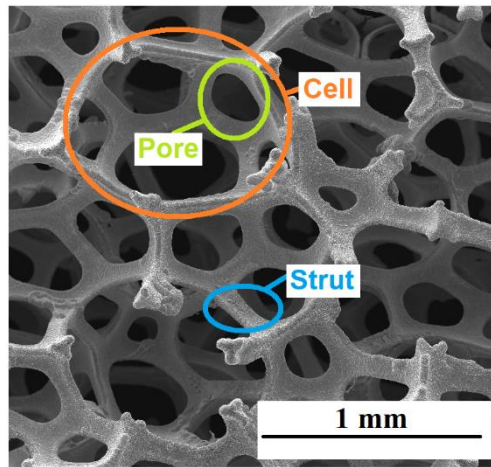


Figure B.1- SEM image of the iron foam microstructure with definition of the geometrical features.

Table B.1- Dimension and strut thickness in the sublayers (whole-body analysis) of the iron foams analyzed with BoneJ

Specimen-layer	Sublayer	ROI dimensions ($\mu\text{m} \times \mu\text{m} \times \mu\text{m}$)	Strut thickness \pm Standard deviation (μm)
Control-L ₁	L ₁₋₁	4061×2707×135	26.99 \pm 6.52
	L ₁₋₂	4061×2707×226	22.49 \pm 6.52
	L ₁₋₃	4061×2707×226	18.75 \pm 5.46
Control-L ₂	L ₂₋₁	4061×2707×212	16.96 \pm 5.02
	L ₂₋₂	4061×2707×226	16.77 \pm 4.77
	L ₂₋₃	4061×2707×226	16.24 \pm 4.69
	L ₃₋₁	4061×2707×214	16.37 \pm 4.85

Control-L₃	L₃₋₂	4061×2707×226	16.94 ± 5.06
	L₃₋₃	4061×2707×226	17.45 ± 5.18
Control-L₄	L₄₋₁	4061×2707×77	18.60 ± 5.63
	L₄₋₂	4061×2707×226	20.56 ± 6.21
	L₄₋₃	4061×2707×226	24.28 ± 6.48
14d-L₁	L₁₋₁	2707×2256×126	21.12 ± 7.02
	L₁₋₂	2707×2256×226	16.81 ± 5.60
	L₁₋₃	2707×2256×226	16.28 ± 4.81
14d-L₂	L₂₋₁	2707×2256×171	16.31 ± 4.83
	L₂₋₂	2707×2256×226	15.90 ± 4.60
	L₂₋₃	2707×2256×226	15.96 ± 4.64
14d-L₃	L₃₋₁	2707×2256×171	16.08 ± 4.57
	L₃₋₂	2707×2256×226	16.00 ± 4.52
	L₃₋₃	2707×2256×226	16.54 ± 4.66
14d-L₄	L₄₋₁	2707×2256×153	17.10 ± 4.90
	L₄₋₂	2707×2256×226	17.88 ± 5.56
	L₄₋₃	2707×2256×226	21.36 ± 7.03

B.2. Design steps of the Kelvin struts in SolidWorks using μ CT measurements

The first step is to estimate the outside perimeter of each triangular cross-section at strut key-locations ($3 \times l_0$, Figure 3.3a). This is conducted by taking the average values of the corresponding μ CT measurements. In Figure 3.2b, the length of the larger red loop is the outside perimeter of the depicted cross-section. For example, for determining the outside perimeter of the cross-section in the middle of the Kelvin-Control periphery struts ($x=0.5L$), the average value of the measured outside perimeters at key location $x = 0.5L$ of 12 struts (in periphery layers) of the Control specimen is considered. Given that all the Kelvin struts are symmetrical, the perimeter values corresponding to $x=0.75L$ locations are in fact the average

of the obtained values associated with $x = 0.25L$ and $0.75L$. Same applies to the values associated with $x = 0$ and L key locations.

Figure 3.3b of the manuscript shows a single half-strut with varying cross-sectional perimeters. We should note that the final cross-section (not shown in the Figure) located inside the node (the region where the half-strut meets 3 other half-struts) are designed based on trials. The next step is to draw the triangular cross-sections at key locations. Then the solid body of the half-strut is created using the Loft tool in the SolidWorks. The half struts are repeated using the Mirror feature, properly combined, and then hollowed out using the Shell tool (periphery and core strut thicknesses are different) to form a cell structure as shown in Figure 3.3c. Eventually, the corners of the cell are cut to obtain a single cell with hollow struts for tessellation (Figure 3.3d).

B.3. Strut thickness estimation

To determine a strut thickness (t), the average of t values calculated at cross-sectional key locations is considered. To obtain t at a key location, i.e. $x = 0.5L$, $x = 0.75L$ or $x = L$, the following equation is used:

$$t = \frac{\sqrt{3}}{6} (l_o - l_i) \quad (\text{B.1})$$

where l_o and l_i represent the outside and the inside length, respectively (Figure B.2b). Eq. B.1 presents the thickness of a hollow equilateral triangle as a function of its outside and inside lengths; l_o value at a key location is 1/3 of the average of measured outside perimeters of the cross-sections at the corresponding key location/layer/specimen. For example, the corresponding value for l_o of Control-Kelvin periphery struts at $x = 0.5L$ is equal to 1/3 of the average of the measured outside perimeter values at $x = 0.5L$ of struts in L_1 and L_4 of Experiment-Control specimen. On the other hand, l_i , the average of the inside-length values at a key location is calculated as:

$$l_{in} = \left(l_o^2 - \frac{4S}{\sqrt{3}} \right)^{0.5} \quad (\text{B.2})$$

where S is the average value of the measured cross-sectional solid areas (Figure 3.2b) at the corresponding key location/layers/specimen. Given that all the Kelvin struts are symmetrical, l_0 and S values corresponding to $x=0.75L$ locations are in fact the average of the values associated with $x=0.25L$ and $0.75L$. Same applies to the values associated with $x = 0$ and L key locations. The nominal strut thickness values obtained using this method are as follows: $18.87 \mu\text{m}$ for Kelvin-Control periphery struts, $11.27 \mu\text{m}$ for Kelvin-Control core struts, $14.02 \mu\text{m}$ for Kelvin-14d periphery struts and $11.52 \mu\text{m}$ for Kelvin-14d core struts.

Using the mentioned nominal strut thickness values, the relative density (RD) of the Kelvin-Control and the Kelvin-14d foams is 2.565% and 2.003%, respectively. The average values of relative densities for Experiment-Control and Experiment-14d samples are 3.01% and 1.97%, respectively, indicating a decent proximity of RD values of the Kelvin foams with their corresponding Experiment foams. However, to have a better representation of the samples for FE analysis (higher RD for the Kelvin-Control and a lower RD for the Kelvin-14d foams), four strut measurements are removed from each of the control and 14d iron foams μCT measurements, and the Kelvin foams are redesigned. This leads to the following nominal strut thicknesses: $19.32 \mu\text{m}$ for Kelvin-Control periphery struts, $11.53 \mu\text{m}$ for Kelvin-Control core struts, $13.25 \mu\text{m}$ for Kelvin-14d periphery struts and $11.21 \mu\text{m}$ for Kelvin-14d core struts. The final relative densities for the Kelvin-Control and Kelvin-14d foams are 2.625% and 1.905%, respectively. The relative density of the Kelvin foams developed in SolidWorks as well as the configuration of their struts at different key locations are presented in Table B.2.

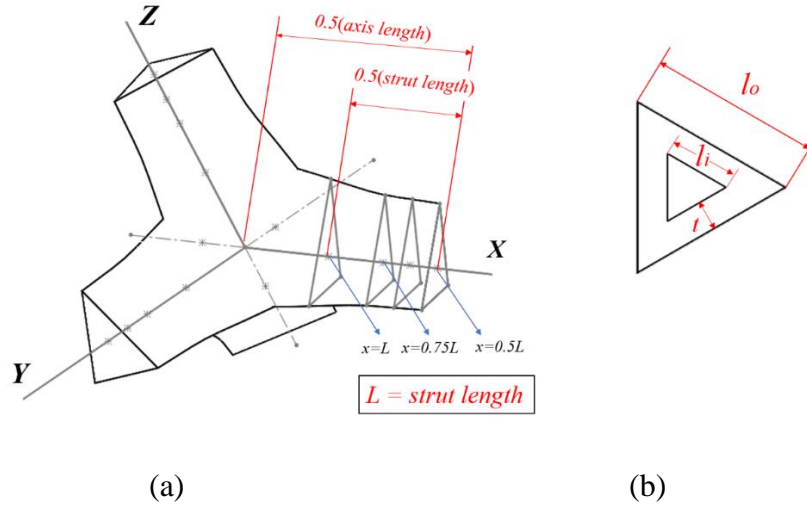


Figure B.2- (a) Structure containing 4 half-struts meeting at the node in a Kelvin cell, (b) A triangular cross-section of a Kelvin strut.

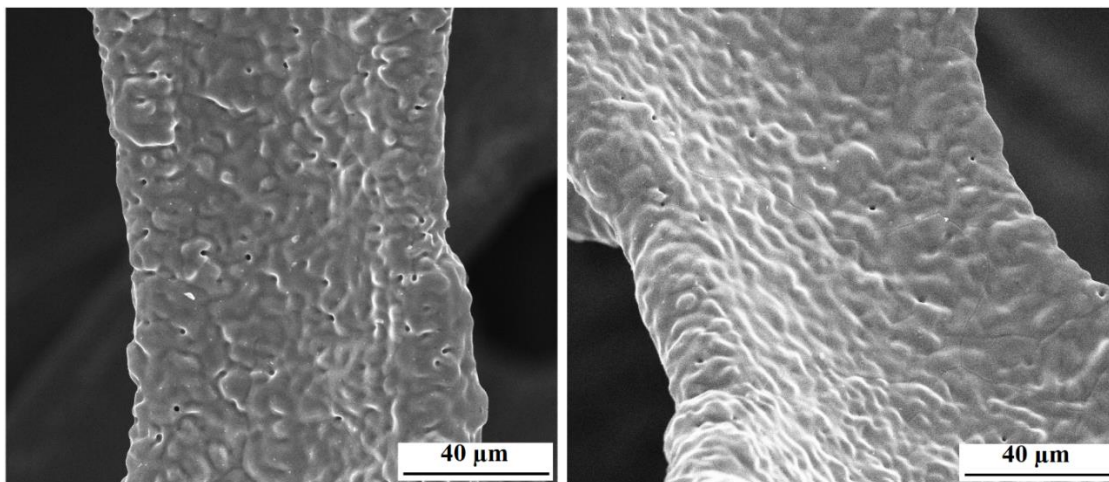
Table B.2- Strut dimensions and relative densities of the developed Kelvin foams.

Kelvin-foam type	Strut type	Key* location, x	l_0 (μm)*	Nominal* t (μm)	Strut* length (μm)	Axis* length (μm)	Relative density (%)				
Control	Periphery	0.5L	111.11	19.32	223.53	393.53	2.625				
Control	Periphery	0.75L	115.48								
Control	Periphery	L	133.06								
Control	Core	0.5L	98.51	11.53			223.53	393.53	2.625		
Control	Core	0.75L	103.18								
Control	Core	L	125.18								
14d	Periphery	0.5L	92.49	13.25					223.53	393.53	1.905
14d	Periphery	0.75L	95.07								
14d	Periphery	L	119.13								
14d	Core	0.5L	90.11	11.21	223.53	393.53					1.905
14d	Core	0.75L	93.96								
14d	Core	L	117.32								
14d-HC	Periphery	0.5L	98.31	15.63			223.53	393.53			1.905

14d-HC	Periphery	0.75L	102.68				
14d-HC	Periphery	L	120.26				
14d-HC	Core	0.5L	85.71	7.84			
14d-HC	Core	0.75L	90.38				
14d-HC	Core	L	112.38				

* Parameters are depicted in Figure B.2.

Figure B.3 depicts the high magnification SEM images of the iron foam struts and the presence of micropores on their surface.



(a)

(b)

Figure B.3- Examples of micropores on the surface of two struts of iron foams used in this study

B.4. Kelvin foam model

A Kelvin foam model with a compression plate model along with the boundary conditions for the *in silico* tests are depicted in Figure B.4.

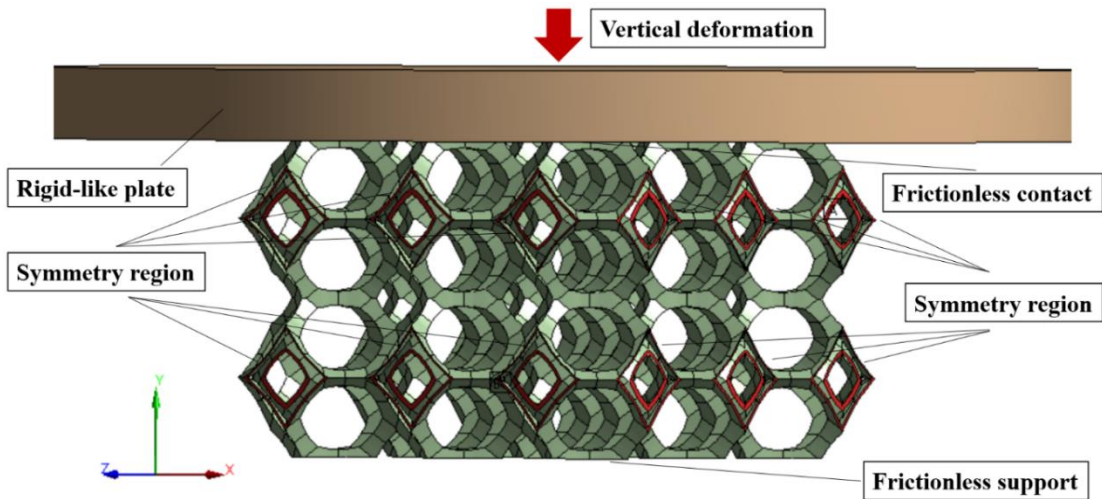


Figure B.4- Kelvin foam model, compression plate and the boundary conditions of the model.

B.5. Cross-section of corroded specimens

Figure B.5 shows the cross-section of corroded uncleaned specimens containing corroded and intact struts after different immersion times. Elemental composition of some of the corrosion products determined by EDS are depicted in Figure B.6.

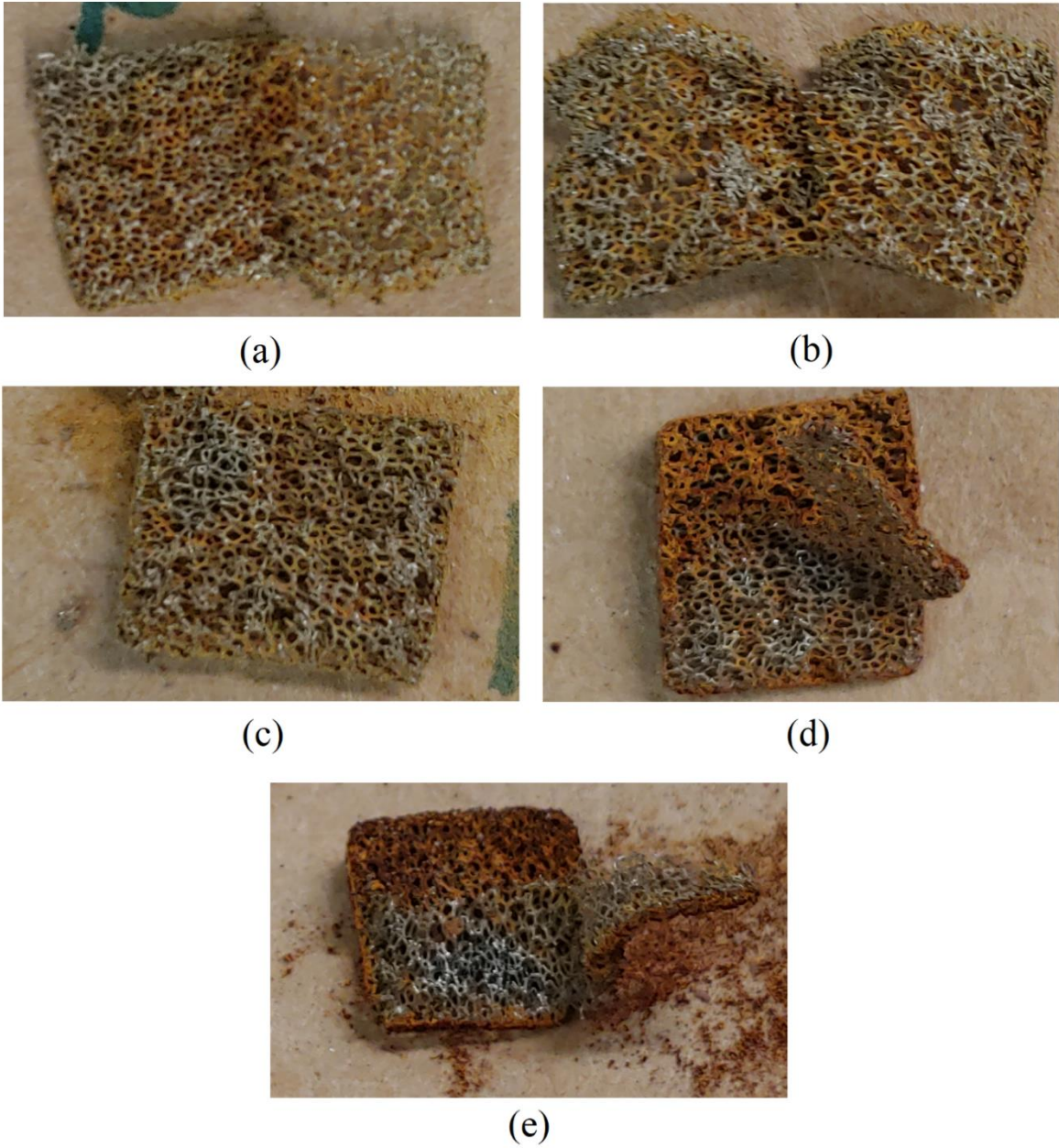
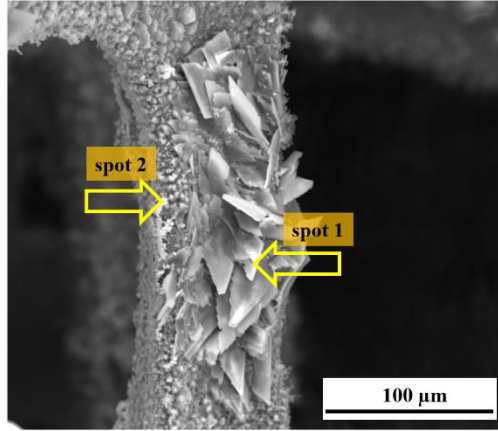


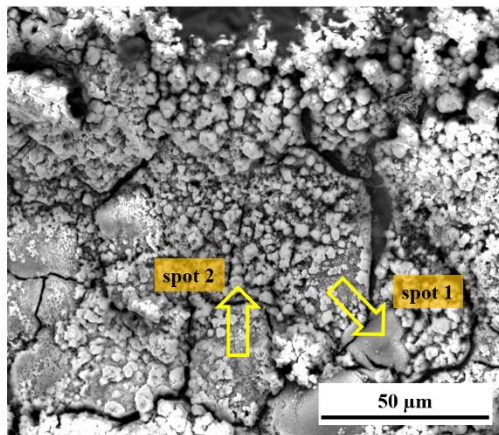
Figure B.5- Cross-sectional observation of an uncleaned (a) 1d, (b) 3d, (c) 5d, (d) 7d, and (e) 10d specimens.



Elements spot 1	Weight %	Atomic %
Fe K	34.14	14.19
O K	47.94	69.52
P K	13.25	9.92
C K	2.21	4.27
Others	2.46	2.11

Elements spot 2	Weight %	Atomic %
Fe K	58.53	30.45
O K	28.79	52.30
P K	2.53	2.38
C K	3.06	7.40
Na K	3.29	4.16
Others	3.79	3.31

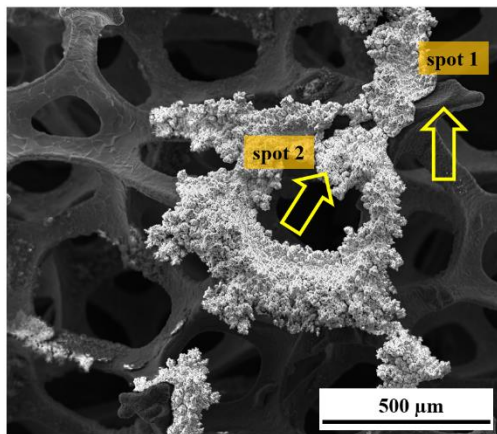
(a)



Elements spot 1	Weight %	Atomic %
Fe K	35.62	15.57
O K	33.58	51.25
P K	8.90	7.02
C K	7.34	14.92
Ca K	7.55	4.60
Na K	3.95	4.20
Others	3.06	2.43

Elements spot 2	Weight %	Atomic %
Fe K	37.77	16.24
O K	38.16	57.27
P K	9.69	7.51
C K	5.87	11.73
Ca K	2.54	1.52
Na K	4.27	4.46
Others	1.71	1.27

(b)



Elements spot 1	Weight %	Atomic %
Fe K	87.01	63.02
O K	2.14	5.40
C K	8.06	27.15
Na K	1.88	3.31
Others	0.91	1.13

Elements spot 2	Weight %	Atomic %
Fe K	55.06	25.99
O K	38.2	62.93
C K	3.47	7.62
Na K	1.99	2.28
Others	1.28	1.18

(c)

Figure B.6- Examples of adherent corrosion products and their EDS analyses, (a) 3d, (b) 5d, and (c)

14d

B.6. Compression stress-strain curves

Figure B.7 depicts the compressive stress-strain curves of the control sample and the corroded iron foams after different immersion periods.

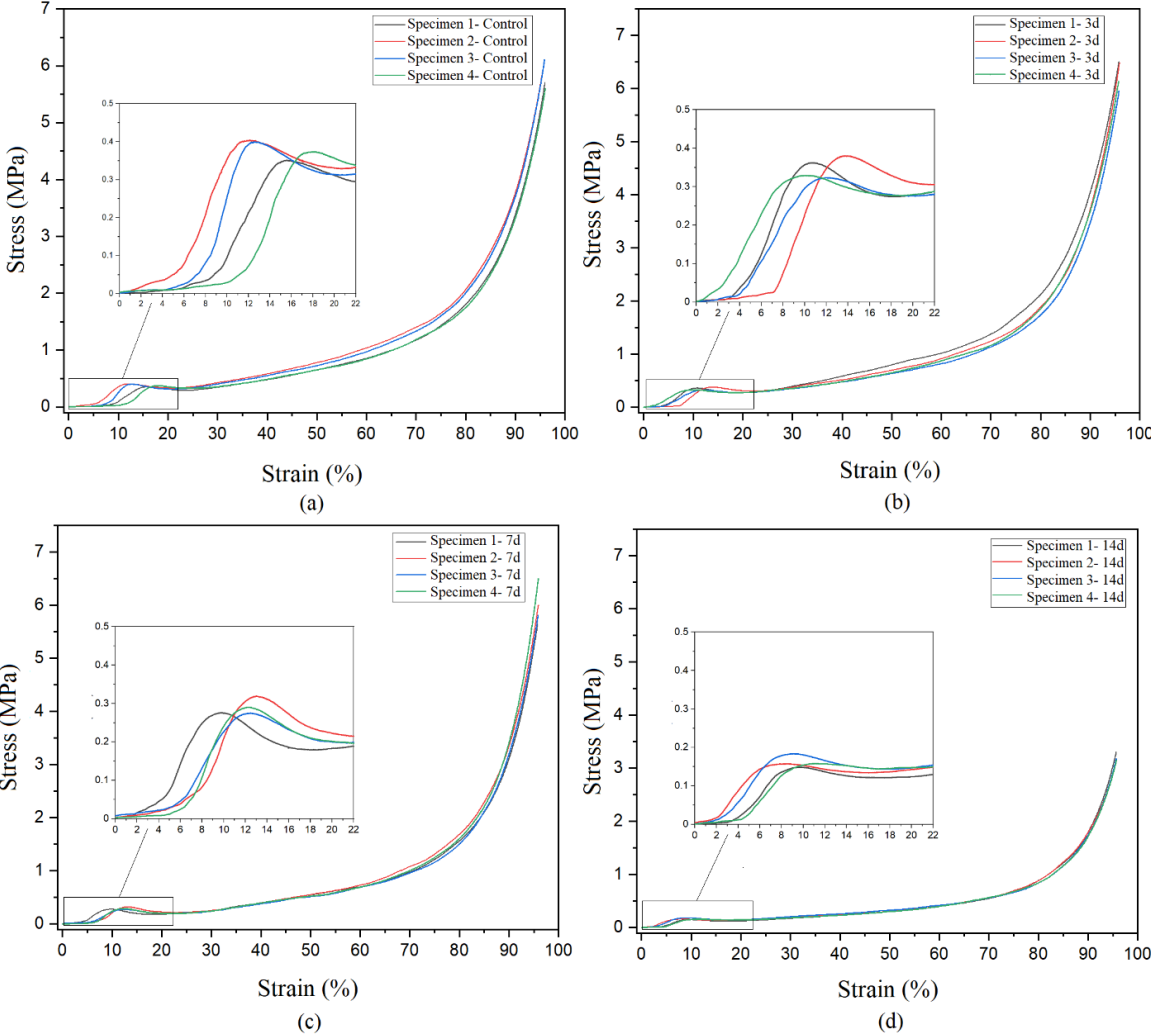


Figure B.7- Compressive response of (a) control and (b, c, d) corroded samples

Bibliography

- [1] A.R. Amini, C.T. Laurencin, S.P. Nukavarapu, Bone tissue engineering: recent advances and challenges, *Critical Reviews™ in Biomedical Engineering* 40(5) (2012) 363-408.
- [2] D. Smrke, P. Rožman, M. Veselko, B. Gubina, Treatment of Bone Defects—Allogenic Platelet Gel and Autologous Bone Technique, *Regenerative Medicine and Tissue Engineering*, IntechOpen2013.
- [3] P. Chocholata, V. Kulda, V. Babuska, Fabrication of scaffolds for bone-tissue regeneration, *Materials* 12(4) (2019) 568.
- [4] L. Polo-Corrales, M. Latorre-Esteves, J.E. Ramirez-Vick, Scaffold design for bone regeneration, *Journal of nanoscience and nanotechnology* 14(1) (2014) 15-56.
- [5] S. Hammouche, D. Hammouche, M.J. McNicholas, Biodegradable Bone Regeneration Synthetic Scaffolds In *Tissue Engineering*, *Current Stem Cell Reseach & Therapy* 7 (2012) 134-42.
- [6] X. Wang, S. Xu, S. Zhou, W. Xu, M. Leary, P. Choong, M. Qian, M. Brandt, Y.M. Xie, Topological design and additive manufacturing of porous metals for bone scaffolds and orthopaedic implants: A review, *Biomaterials* 83 (2016) 127-41.
- [7] S. Wu, X. Liu, K.W. Yeung, C. Liu, X. Yang, Biomimetic porous scaffolds for bone tissue engineering, *Materials Science and Engineering: R: Reports* 80 (2014) 1-36.
- [8] B. Guo, B. Lei, P. Li, P.X. Ma, Functionalized scaffolds to enhance tissue regeneration, *Regen Biomater* 2(1) (2015) 47-57.
- [9] M.A. Velasco, C.A. Narvaez-Tovar, D.A. Garzon-Alvarado, Design, materials, and mechanobiology of biodegradable scaffolds for bone tissue engineering, *Biomed Res Int* 2015 (2015).
- [10] M. Navarro, A. Michiardi, O. Castano, J.A. Planell, Biomaterials in orthopaedics, *Journal of the Royal Society Interface* 5(27) (2008) 1137-1158.
- [11] W. Suchanek, M. Yoshimura, Processing and properties of hydroxyapatite-based biomaterials for use as hard tissue replacement implants, *Journal of Materials Research* 13(1) (1998) 94-117.
- [12] G. Bini, F. Bini, R. Bedini, A. Marinozzi, F. Marinozzi, A topological look at human trabecular bone tissue, *Mathematical biosciences* 288 (2017) 159-165.
- [13] D.P. Byrne, D. Lacroix, J.A. Planell, D.J. Kelly, P.J. Prendergast, Simulation of tissue differentiation in a scaffold as a function of porosity, Young's modulus and dissolution rate: application of mechanobiological models in tissue engineering, *Biomaterials* 28(36) (2007) 5544-5554.
- [14] M. Long, H. Rack, Titanium alloys in total joint replacement—a materials science perspective, *Biomaterials* 19(18) (1998) 1621-1639.
- [15] Y. Li, P. Pavanram, J. Zhou, K. Lietaert, F. Bobbert, Y. Kubo, M. Leeflang, H. Jahr, A. Zadpoor, Additively manufactured functionally graded biodegradable porous zinc, *Biomaterials Science* 8(9) (2020) 2404-2419.
- [16] R. Tolouei, J. Harrison, C. Paternoster, S. Turgeon, P. Chevallier, D. Mantovani, The use of multiple pseudo-physiological solutions to simulate the degradation behavior of pure iron as a metallic resorbable implant: A surface-characterization study, *Physical Chemistry Chemical Physics* 18(29) (2016) 19637-19646.
- [17] G. Ryan, A. Pandit, D.P. Apatsidis, Fabrication methods of porous metals for use in orthopaedic applications, *Biomaterials* 27(13) (2006) 2651-2670.

- [18] A.H. Yusop, A.A. Bakir, N.A. Shaharom, M.R. Abdul Kadir, H. Hermawan, Porous biodegradable metals for hard tissue scaffolds: a review, *Int J Biomater* 2012 (2012) 641430.
- [19] R. Alavi, A. Trenggono, S. Champagne, H. Hermawan, Investigation on Mechanical Behavior of Biodegradable Iron Foams under Different Compression Test Conditions, *Metals* 7(6) (2017) 202.
- [20] M. Hrubovcakova, M. Kupkova, M. Dzupon, Fe and Fe-P Foam for Biodegradable Bone Replacement Material: Morphology, Corrosion Behaviour, and Mechanical Properties, *Advances in Materials Science and Engineering* (2016).
- [21] J. He, F.L. He, D.W. Li, Y.L. Liu, D.C. Yin, A novel porous Fe/Fe-W alloy scaffold with a double-layer structured skeleton: Preparation, in vitro degradability and biocompatibility, *Colloids Surf B Biointerfaces* 142 (2016) 325-33.
- [22] P. Sharma, P.M. Pandey, Corrosion behaviour of the porous iron scaffold in simulated body fluid for biodegradable implant application, *Materials Science and Engineering: C* 99 (2019) 838-852.
- [23] Y. Li, H. Jahr, K. Lietaert, P. Pavanram, A. Yilmaz, L.I. Fockaert, M.A. Leeflang, B. Pouran, Y. Gonzalez-Garcia, H. Weinans, J.M.C. Mol, J. Zhou, A.A. Zadpoor, Additively manufactured biodegradable porous iron, *Acta Biomater* 77 (2018) 380-393.
- [24] Y. Li, H. Jahr, P. Pavanram, F. Bobbert, U. Puggi, X.-Y. Zhang, B. Pouran, M. Leeflang, H. Weinans, J. Zhou, A.A. Zadpoor, Additively manufactured functionally graded biodegradable porous iron, *Acta biomaterialia* 96 (2019) 646-661.
- [25] A.H.M. Yusop, N.M. Daud, H. Nur, M.R.A. Kadir, H. Hermawan, Controlling the degradation kinetics of porous iron by poly (lactic-co-glycolic acid) infiltration for use as temporary medical implants, *Scientific reports* 5 (2015) 11194.
- [26] W. Wang, G. Jia, Q. Wang, H. Huang, X. Li, H. Zeng, W. Ding, F. Witte, C. Zhang, W. Jia, The in vitro and in vivo biological effects and osteogenic activity of novel biodegradable porous Mg alloy scaffolds, *Materials & Design* 189 (2020) 108514.
- [27] J. Osorio-Hernández, M. Suarez, R. Goodall, G. Lara-Rodriguez, I. Alfonso, I. Figueroa, Manufacturing of open-cell Mg foams by replication process and mechanical properties, *Materials & Design* 64 (2014) 136-141.
- [28] R. Hedayati, S. Ahmadi, K. Lietaert, N. Tümer, Y. Li, S. Amin Yavari, A.A. Zadpoor, Fatigue and quasi-static mechanical behavior of bio-degradable porous biomaterials based on magnesium alloys, *Journal of Biomedical Materials Research Part A* 106(7) (2018) 1798-1811.
- [29] Y. Li, J. Zhou, P. Pavanram, M. Leeflang, L. Fockaert, B. Pouran, N. Tümer, K.-U. Schröder, J. Mol, H. Weinans, A.A. Zadpoor, Additively manufactured biodegradable porous magnesium, *Acta biomaterialia* 67 (2018) 378-392.
- [30] M. Yazdimamaghani, M. Razavi, D. Vashaei, K. Moharamzadeh, A.R. Boccaccini, L. Tayebi, Porous magnesium-based scaffolds for tissue engineering, *Mater Sci Eng C Mater Biol Appl* 71 (2017) 1253-1266.
- [31] A.P.M. Saad, N. Jasmawati, M.N. Harun, M.R.A. Kadir, H. Nur, H. Hermawan, A. Syahrom, Dynamic degradation of porous magnesium under a simulated environment of human cancellous bone, *Corrosion Science* 112 (2016) 495-506.
- [32] M.Q. Cheng, T. Wahafu, G.F. Jiang, W. Liu, Y.Q. Qiao, X.C. Peng, T. Cheng, X.L. Zhang, G. He, X.Y. Liu, A novel open-porous magnesium scaffold with controllable microstructures and properties for bone regeneration, *Scientific Reports* 6 (2016).

- [33] Y. Li, P. Pavanram, J. Zhou, K. Lietaert, P. Taheri, W. Li, H. San, M. Leeflang, J. Mol, H. Jahr, A.A. Zadpoor, Additively manufactured biodegradable porous zinc, *Acta Biomaterialia* 101 (2020) 609-623.
- [34] J. Capek, E. Jablonska, J. Lipov, T.F. Kubatik, D. Vojtech, Preparation and characterization of porous zinc prepared by spark plasma sintering as a material for biodegradable scaffolds, *Materials Chemistry and Physics* 203 (2018) 249-258.
- [35] I. Cockerill, Y. Su, S. Sinha, Y.-X. Qin, Y. Zheng, M.L. Young, D. Zhu, Porous zinc scaffolds for bone tissue engineering applications: A novel additive manufacturing and casting approach, *Materials Science and Engineering: C* 110 (2020) 110738.
- [36] Y. Hou, G. Jia, R. Yue, C. Chen, J. Pei, H. Zhang, H. Huang, M. Xiong, G. Yuan, Synthesis of biodegradable Zn-based scaffolds using NaCl templates: relationship between porosity, compressive properties and degradation behavior, *Materials Characterization* 137 (2018) 162-169.
- [37] L. Zhao, X. Wang, T. Wang, Y. Xia, C. Cui, Mechanical properties and biodegradation of porous Zn-1Al alloy scaffolds, *Materials Letters* 247 (2019) 75-78.
- [38] H. Hermawan, Updates on the research and development of absorbable metals for biomedical applications, *Progress in biomaterials* (2018) 1-18.
- [39] Y.F. Zheng, X.N. Gu, F. Witte, Biodegradable metals, *Materials Science and Engineering: R: Reports* 77 (2014) 1-34.
- [40] D. Vojtěch, J. Kubásek, J. Čapek, I. Pospíšilová, Comparative mechanical and corrosion studies on magnesium, zinc and iron alloys as biodegradable metals, *Materiali in tehnologije* 49(6) (2015) 877-882.
- [41] D. Noviana, D. Paramitha, M.F. Ulum, H. Hermawan, The effect of hydrogen gas evolution of magnesium implant on the postimplantation mortality of rats, *Journal of Orthopaedic Translation* 5 (2016) 9-15.
- [42] K. Oh, E. Lee, J.S. Bae, M. Jang, R. Poss, B. Kieback, G. Walther, B. Kloeden, Large scale production and applications of alloy metal foam, 2012.
- [43] L.J. Gibson, THE MECHANICAL-BEHAVIOR OF CANCELLOUS BONE, *Journal of Biomechanics* 18(5) (1985) 317-&.
- [44] G. Gąsior, J. Szczepański, A. Radtke, Biodegradable Iron-Based Materials—What Was Done and What More Can Be Done?, *Materials* 14(12) (2021) 3381.
- [45] T. Kraus, F. Moszner, S. Fischerauer, M. Fiedler, E. Martinelli, J. Eichler, F. Witte, E. Willbold, M. Schinhammer, M. Meischel, Biodegradable Fe-based alloys for use in osteosynthesis: Outcome of an in vivo study after 52 weeks, *Acta biomaterialia* 10(7) (2014) 3346-3353.
- [46] S. Agarwal, J. Curtin, B. Duffy, S. Jaiswal, Biodegradable magnesium alloys for orthopaedic applications: A review on corrosion, biocompatibility and surface modifications, *Materials Science and Engineering: C* 68 (2016) 948-963.
- [47] A.A. Zadpoor, R. Hedayati, Analytical relationships for prediction of the mechanical properties of additively manufactured porous biomaterials, *Journal of Biomedical Materials Research Part A* 104(12) (2016) 3164-3174.
- [48] J. Shi, A. Akbarzadeh, Architected cellular piezoelectric metamaterials: Thermo-electro-mechanical properties, *Acta Materialia* 163 (2019) 91-121.
- [49] H. Basri, A.T. Prakoso, M.A. Sulong, A.P. Md Saad, M.H. Ramlee, D. Agustin Wahjuningrum, S. Sipaun, A. Öchsner, A. Syahrom, Mechanical degradation model of porous magnesium scaffolds

under dynamic immersion, *Proceedings of the Institution of Mechanical Engineers, Part L: Journal of Materials: Design and Applications* 234(1) (2020) 175-185.

[50] X. Lu, C. Lai, L. Chan, Novel design of a coral-like open-cell porous degradable magnesium implant for orthopaedic application, *Materials & Design* 188 (2020) 108474.

[51] J.A. Grogan, B.J. O'Brien, S.B. Leen, P.E. McHugh, A corrosion model for bioabsorbable metallic stents, *Acta Biomater* 7(9) (2011) 3523-33.

[52] E.L. Boland, J.A. Grogan, P.E. McHugh, Computational Modeling of the Mechanical Performance of a Magnesium Stent Undergoing Uniform and Pitting Corrosion in a Remodeling Artery, *Journal of Medical Devices* 11(2) (2017) 021013.

[53] M. Sulong, I. Belova, A. Boccaccini, G. Murch, T. Fiedler, A model of the mechanical degradation of foam replicated scaffolds, *Journal of materials science* 51(8) (2016) 3824-3835.

[54] A.P.M. Saad, A.T. Prakoso, M. Sulong, H. Basri, D.A. Wahjuningrum, A. Syahrom, Impacts of dynamic degradation on the morphological and mechanical characterisation of porous magnesium scaffold, *Biomechanics and modeling in mechanobiology* 18(3) (2019) 797-811.

[55] Z. Nie, Y. Lin, Q. Tong, Modeling structures of open cell foams, *Computational Materials Science* 131 (2017) 160-169.

[56] W. Warren, A. Kraynik, Linear elastic behavior of a low-density Kelvin foam with open cells, (1997).

[57] A. Weizbauer, C. Modrejewski, S. Behrens, H. Klein, P. Helmecke, J.-M. Seitz, H. Windhagen, K. Moehwald, J. Reifenrath, H. Waizy, Comparative invitro study and biomechanical testing of two different magnesium alloys, *Journal of Biomaterials Applications* 28(8) (2014) 1264-1273.

[58] I. Adekanmbi, C.Z. Mosher, H.H. Lu, M. Riehle, H. Kubba, K.E. Tanner, Mechanical behaviour of biodegradable AZ31 magnesium alloy after long term in vitro degradation, *Materials Science & Engineering C-Materials for Biological Applications* 77 (2017) 1135-1144.

[59] Z. Li, S.Z. Sun, M.F. Chen, B.D. Fahlman, D.B. Liu, H.W. Bi, In vitro and in vivo corrosion, mechanical properties and biocompatibility evaluation of MgF₂-coated Mg-Zn-Zr alloy as cancellous screws, *Materials Science & Engineering C-Materials for Biological Applications* 75 (2017) 1268-1280.

[60] M. Sikora-Jasinska, P. Chevallier, S. Turgeon, C. Paternoster, E. Mostaed, M. Vedani, D. Mantovani, Long-term in vitro degradation behaviour of Fe and Fe/Mg 2 Si composites for biodegradable implant applications, *RSC advances* 8(18) (2018) 9627-9639.

[61] K. Bekele Gebresellasie, *Mechanical Integrity of Biodegradable Metals During Degradation*, Computational Science & Engineering, North Carolina A&T State University, Greensboro, North Carolina, 2017.

[62] P. Zartner, R. Cesnjevar, H. Singer, M. Weyand, First successful implantation of a biodegradable metal stent into the left pulmonary artery of a preterm baby, *Catheterization and Cardiovascular Interventions* 66(4) (2005) 590-594.

[63] B.H. Chew, D. Lange, R.F. Paterson, K. Hendlin, M. Monga, K.W. Clinkscales, S.W. Shalaby, B.A. Hadaschik, Next Generation Biodegradable Ureteral Stent in a Yucatan Pig Model, *Journal of Urology* 183(2) (2010) 765-771.

[64] J. Davidson, A. Mishra, P. Kovacs, R. Poggie, New surface-hardened, low-modulus, corrosion-resistant Ti-13Nb-13Zr alloy for total hip arthroplasty, *Bio-medical materials and engineering* 4(3) (1994) 231-243.

- [65] H. Hermawan, *Biodegradable Metals: State of the Art, Biodegradable Metals: From Concept to Applications*, Springer Berlin Heidelberg, Berlin, Heidelberg, 2012, pp. 13-22.
- [66] T. Sercombe, L.-C. Zhang, S. Li, Y. Hao, Additive manufacturing of cp-Ti, Ti-6Al-4V and Ti2448, *Titanium in Medical and Dental Applications*, Elsevier2018, pp. 303-324.
- [67] K. Alvarez, H. Nakajima, *Metallic Scaffolds for Bone Regeneration*, *Materials* 2(3) (2009) 790-832.
- [68] D. Hong, D.-T. Chou, O.I. Velikokhatnyi, A. Roy, B. Lee, I. Swink, I. Issaev, H.A. Kuhn, P.N. Kumta, Binder-jetting 3D printing and alloy development of new biodegradable Fe-Mn-Ca/Mg alloys, *Acta biomaterialia* 45 (2016) 375-386.
- [69] H. Li, Y. Zheng, L. Qin, Progress of biodegradable metals, *Progress in Natural Science: Materials International* 24(5) (2014) 414-422.
- [70] J.M. Seitz, M. Durisin, J. Goldman, J.W. Drelich, Recent Advances in Biodegradable Metals for Medical Sutures: A Critical Review, *Advanced Healthcare Materials* 4(13) (2015) 1915-1936.
- [71] Y.Q. Chen, W.T. Zhang, M.F. Maitz, M.Y. Chen, H. Zhang, J.L. Mao, Y.C. Zhao, N. Huang, G.J. Wan, Comparative corrosion behavior of Zn with Fe and Mg in the course of immersion degradation in phosphate buffered saline, *Corrosion Science* 111 (2016) 541-555.
- [72] S. Zhang, X. Zhang, C. Zhao, J. Li, Y. Song, C. Xie, H. Tao, Y. Zhang, Y. He, Y. Jiang, Research on an Mg-Zn alloy as a degradable biomaterial, *Acta biomaterialia* 6(2) (2010) 626-640.
- [73] X. Gu, X. Xie, N. Li, Y. Zheng, L. Qin, In vitro and in vivo studies on a Mg-Sr binary alloy system developed as a new kind of biodegradable metal, *Acta biomaterialia* 8(6) (2012) 2360-2374.
- [74] F. Rosalbino, S. De Negri, A. Saccone, E. Angelini, S. Delfino, Bio-corrosion characterization of Mg-Zn-X (X= Ca, Mn, Si) alloys for biomedical applications, *Journal of Materials Science: Materials in Medicine* 21(4) (2010) 1091-1098.
- [75] J. Liu, D. Bian, Y. Zheng, X. Chu, Y. Lin, M. Wang, Z. Lin, M. Li, Y. Zhang, S. Guan, Comparative In Vitro study on binary Mg-RE (Sc, Y, La, Ce, Pr, Nd, Sm, Eu, Gd, Tb, Dy, Ho, Er, Tm, Yb and Lu) alloy systems, *Acta Biomaterialia* 102 (2020) 508-528.
- [76] H.R. Bakhsheshi-Rad, M. Abdollahi, E. Hamzah, A.F. Ismail, M. Bahmanpour, Modelling corrosion rate of biodegradable magnesium-based alloys: The case study of Mg-Zn-RE-xCa (x= 0, 0.5, 1.5, 3 and 6 wt%) alloys, *Journal of Alloys and Compounds* 687 (2016) 630-642.
- [77] H. Hermawan, D. Dubé, D. Mantovani, Degradable metallic biomaterials: design and development of Fe-Mn alloys for stents, *Journal of Biomedical Materials Research Part A: An Official Journal of The Society for Biomaterials, The Japanese Society for Biomaterials, and The Australian Society for Biomaterials and the Korean Society for Biomaterials* 93(1) (2010) 1-11.
- [78] M. Schinhammer, P. Steiger, F. Moszner, J.F. Löffler, P.J. Uggowitzer, Degradation performance of biodegradable FeMnC (Pd) alloys, *Materials Science and Engineering: C* 33(4) (2013) 1882-1893.
- [79] H. Wang, Y. Zheng, J. Liu, C. Jiang, Y. Li, In vitro corrosion properties and cytocompatibility of Fe-Ga alloys as potential biodegradable metallic materials, *Materials Science and Engineering: C* 71 (2017) 60-66.
- [80] D. Carluccio, M. Bermingham, D. Kent, A.G. Demir, B. Previtali, M.S. Dargusch, Comparative study of pure iron manufactured by selective laser melting, laser metal deposition, and casting processes, *Advanced Engineering Materials* 21(7) (2019) 1900049.

- [81] M. Moravej, F. Prima, M. Fiset, D. Mantovani, Electroformed iron as new biomaterial for degradable stents: Development process and structure–properties relationship, *Acta biomaterialia* 6(5) (2010) 1726-1735.
- [82] D. Carluccio, C. Xu, J. Venezuela, Y. Cao, D. Kent, M. Bermingham, A.G. Demir, B. Previtali, Q. Ye, M. Dargusch, Additively manufactured iron-manganese for biodegradable porous load-bearing bone scaffold applications, *Acta Biomaterialia* 103 (2020) 346-360.
- [83] J. Capek, D. Vojtech, A. Oborna, Microstructural and mechanical properties of biodegradable iron foam prepared by powder metallurgy, *Materials & Design* 83 (2015) 468-482.
- [84] G. Li, H. Yang, Y. Zheng, X.-H. Chen, J.-A. Yang, D. Zhu, L. Ruan, K. Takashima, Challenges in the use of zinc and its alloys as biodegradable metals: Perspective from biomechanical compatibility, *Acta biomaterialia* 97 (2019) 23-45.
- [85] W.-J. Lin, D.-Y. Zhang, G. Zhang, H.-T. Sun, H.-P. Qi, L.-P. Chen, Z.-Q. Liu, R.-L. Gao, W. Zheng, Design and characterization of a novel biocorrosible iron-based drug-eluting coronary scaffold, *Materials & Design* 91 (2016) 72-79.
- [86] H. Li, Z. Shi, L. Wang, Opportunities and challenges of biodegradable Zn-based alloys, *Journal of Materials Science & Technology* 46 (2020) 136-138.
- [87] R.W. Revie, H.H. Uhlig, *Corrosion and Corrosion Control, An Introduction to Corrosion Science and Engineering*, 4 ed., A JOHN WILEY & SONS, INC.2008.
- [88] M. Peuster, P. Wohlsein, M. Brugmann, M. Ehlerding, K. Seidler, C. Fink, H. Brauer, A. Fischer, G. Hausdorf, A novel approach to temporary stenting: degradable cardiovascular stents produced from corrodible metal - results 6-18 months after implantation into New Zealand white rabbits, *Heart* 86(5) (2001) 563-569.
- [89] M. Schinhammer, A.C. Hanzi, J.F. Löffler, P.J. Uggowitzer, Design strategy for biodegradable Fe-based alloys for medical applications, *Acta Biomaterialia* 6(5) (2010) 1705-1713.
- [90] M. Heiden, E. Walker, E. Nauman, L. Stanciu, Evolution of novel bioresorbable iron-manganese implant surfaces and their degradation behaviors in vitro, *Journal of Biomedical Materials Research Part A* 103(1) (2015) 185-193.
- [91] J. Cheng, T. Huang, Y.F. Zheng, Relatively uniform and accelerated degradation of pure iron coated with micro-patterned Au disc arrays, *Materials Science & Engineering C-Materials for Biological Applications* 48 (2015) 679-687.
- [92] B. Liu, Y.F. Zheng, Effects of alloying elements (Mn, Co, Al, W, Sn, B, C and S) on biodegradability and in vitro biocompatibility of pure iron, *Acta Biomaterialia* 7(3) (2011) 1407-1420.
- [93] H. Hermawan, A. Purnama, D. Dube, J. Couet, D. Mantovani, Fe-Mn alloys for metallic biodegradable stents: Degradation and cell viability studies, *Acta Biomaterialia* 6(5) (2010) 1852-1860.
- [94] J. Capek, K. Stehlikova, A. Michalcova, S. Msallamova, D. Vojtech, Microstructure, mechanical and corrosion properties of biodegradable powder metallurgical Fe-2 wt% X (X = Pd, Ag and C) alloys, *Materials Chemistry and Physics* 181 (2016) 501-511.
- [95] M. Moravej, A. Purnama, M. Fiset, J. Couet, D. Mantovani, Electroformed pure iron as a new biomaterial for degradable stents: In vitro degradation and preliminary cell viability studies, *Acta Biomaterialia* 6(5) (2010) 1843-1851.
- [96] F. Garcia-Moreno, *Commercial Applications of Metal Foams: Their Properties and Production*, *Materials (Basel)* 9(2) (2016).

- [97] H.P. Degischer, B. Kriszt, Handbook of cellular metals: production, processing, applications, Wiley-vch2002.
- [98] M.F. Ashby, A. Evans, N.A. Fleck, L.J. Gibson, J.W. Hutchinson, H.N. Wadley, Metal foams: a design guide-Butterworth-Heinemann, Oxford, UK, ISBN 0-7506-7219-6, Published 2000, Hardback, 251 pp., \$75.00, Materials and Design 1(23) (2002) 119.
- [99] L.J. Gibson, M.F. Ashby, Cellular Solids: Structure and Properties, 2 ed.1997.
- [100] R. Gorejová, L. Haverová, R. Oriňaková, A. Oriňak, M. Oriňak, Recent advancements in Fe-based biodegradable materials for bone repair, Journal of Materials Science 54(3) (2019) 1913-1947.
- [101] B. Arifvianto, J. Zhou, Fabrication of Metallic Biomedical Scaffolds with the Space Holder Method: A Review, Materials 7(5) (2014) 3588-3622.
- [102] C.E. Wen, M. Mabuchi, Y. Yamada, K. Shimojima, Y. Chino, T. Asahina, Processing of biocompatible porous Ti and Mg, Scripta Materialia 45(10) (2001) 1147-1153.
- [103] P. Quadbeck, K. Kümmel, R. Hauser, G. Standke, J. Adler, G. Stephani, Open cell metal foams-application-oriented structure and material selection, Proceedings of the CELLMAT (2010).
- [104] J. Li, S. Li, C. Van Blitterswijk, K. De Groot, A novel porous Ti6Al4V: characterization and cell attachment, Journal of Biomedical Materials Research Part A: An Official Journal of The Society for Biomaterials, The Japanese Society for Biomaterials, and The Australian Society for Biomaterials and the Korean Society for Biomaterials 73(2) (2005) 223-233.
- [105] E. Dayaghi, H. Bakhsheshi-Rad, E. Hamzah, A. Akhavan-Farid, A. Ismail, M. Aziz, E. Abdolahi, Magnesium-zinc scaffold loaded with tetracycline for tissue engineering application: In vitro cell biology and antibacterial activity assessment, Materials Science and Engineering: C 102 (2019) 53-65.
- [106] J. Rúa, A. Zuleta, J. Ramírez, P. Fernández-Morales, Micro-arc oxidation coating on porous magnesium foam and its potential biomedical applications, Surface and Coatings Technology 360 (2019) 213-221.
- [107] L. Zhao, Z. Zhang, Y. Song, S. Liu, Y. Qi, X. Wang, Q. Wang, C. Cui, Mechanical properties and in vitro biodegradation of newly developed porous Zn scaffolds for biomedical applications, Materials & Design 108 (2016) 136-144.
- [108] R. Gorejová, R. Oriňaková, Z. Orságová Králová, M. Baláž, M. Kupková, M. Hrubovčáková, L. Haverová, M. Džupon, A. Oriňak, F. Kaľavský, In vitro corrosion behavior of biodegradable iron foams with polymeric coating, Materials 13(1) (2020) 184.
- [109] R. Oriňaková, R. Gorejová, Z.O. Králová, L. Haverová, A. Oriňak, I. Maskaľová, M. Kupková, M. Džupon, M. Baláž, M. Hrubovčáková, Evaluation of mechanical properties and hemocompatibility of open cell iron foams with polyethylene glycol coating, Applied Surface Science 505 (2020) 144634.
- [110] P. Liu, D. Zhang, Y. Dai, J. Lin, Y. Li, C. Wen, Microstructure, mechanical properties, degradation behavior, and biocompatibility of porous Fe-Mn alloys fabricated by sponge impregnation and sintering techniques, Acta Biomaterialia 114 (2020) 485-496.
- [111] P. Sharma, K.G. Jain, P.M. Pandey, S. Mohanty, In vitro degradation behaviour, cytocompatibility and hemocompatibility of topologically ordered porous iron scaffold prepared using 3D printing and pressureless microwave sintering, Materials Science and Engineering: C 106 (2020) 110247.
- [112] P. Sharma, P.M. Pandey, A novel manufacturing route for the fabrication of topologically-ordered open-cell porous iron scaffold, Materials Letters 222 (2018) 160-163.

- [113] V. Bhavar, P. Kattire, V. Patil, S. Khot, K. Gujar, R. Singh, A review on powder bed fusion technology of metal additive manufacturing, 4th International conference and exhibition on Additive Manufacturing Technologies-AM-2014, 2014, pp. 1-2.
- [114] Y. Qin, P. Wen, M. Voshage, Y. Chen, P.G. Schückler, L. Jauer, D. Xia, H. Guo, Y. Zheng, J.H. Schleifenbaum, Additive manufacturing of biodegradable Zn-xWE43 porous scaffolds: Formation quality, microstructure and mechanical properties, *Materials & Design* 181 (2019) 107937.
- [115] A. Kopp, T. Derra, M. Müther, L. Jauer, J.H. Schleifenbaum, M. Voshage, O. Jung, R. Smeets, N. Kröger, Influence of design and postprocessing parameters on the degradation behavior and mechanical properties of additively manufactured magnesium scaffolds, *Acta biomaterialia* 98 (2019) 23-35.
- [116] J. Dong, Y. Li, P. Lin, M. Leeflang, S. van Asperen, K. Yu, N. Tümer, B. Norder, A. Zadpoor, J. Zhou, Solvent-cast 3D printing of magnesium scaffolds, *Acta Biomaterialia* 114 (2020) 497-514.
- [117] D.-T. Chou, D. Wells, D. Hong, B. Lee, H. Kuhn, P.N. Kumta, Novel processing of iron–manganese alloy-based biomaterials by inkjet 3-D printing, *Acta biomaterialia* 9(10) (2013) 8593-8603.
- [118] T. Kokubo, H. Takadama, How useful is SBF in predicting in vivo bone bioactivity?, *Biomaterials* 27(15) (2006) 2907-2915.
- [119] S. Arabnejad Khanoki, D. Pasini, Multiscale design and multiobjective optimization of orthopedic hip implants with functionally graded cellular material, *Journal of biomechanical engineering* 134(3) (2012).
- [120] J. Kuiper, R. Huiskes, Mathematical optimization of elastic properties: application to cementless hip stem design, (1997).
- [121] C. Betts, Benefits of metal foams and developments in modelling techniques to assess their materials behaviour: a review, *Materials Science and Technology* 28(2) (2012) 129-143.
- [122] L.J. Gibson, Mechanical behavior of metallic foams, *Annual Review of Materials Science* 30 (2000) 191-227.
- [123] H. Hagiwara, D.J. Green, Elastic Behavior of Open-Cell Alumina, *Journal of the American Ceramic Society* 70(11) (1987) 811-815.
- [124] E. Amsterdam, J.T.M. De Hosson, P. Onck, On the plastic collapse stress of open-cell aluminum foam, *Scripta Materialia* 59(6) (2008) 653-656.
- [125] T. Daxner, Finite Element Modeling of Foams, in: H. Altenbach, A. Öchsner (Eds.), *Cellular and porous materials in structures and processes*, Springer Science & Business Media 2011, pp. 47-106.
- [126] M.W.D. VanderBurg, V. Shulmeister, E. VanderGeissen, R. Marissen, On the linear elastic properties of regular and random open-cell foam models, *Journal of Cellular Plastics* 33(1) (1997) 31-&.
- [127] Y. Sun, Q. Li, T. Lowe, S. McDonald, P. Withers, Investigation of strain-rate effect on the compressive behaviour of closed-cell aluminium foam by 3D image-based modelling, *Materials & Design* 89 (2016) 215-224.
- [128] A. Roberts, E.J. Garboczi, Elastic properties of model random three-dimensional open-cell solids, *Journal of the Mechanics and Physics of Solids* 50(1) (2002) 33-55.
- [129] P. Siegkas, V. Tagarielli, N. Petrinic, Modelling stochastic foam geometries for FE simulations using 3D Voronoi cells, *Procedia Materials Science* 4 (2014) 221-226.

- [130] S. Iio, K. Hasegawa, S. Fushimi, A. Yonezu, X. Chen, On compressive deformation behavior of hollow-strut cellular materials, *Materials & Design* 105 (2016) 1-8.
- [131] W.-Y. Jang, A.M. Kraynik, S. Kyriakides, On the microstructure of open-cell foams and its effect on elastic properties, *International Journal of Solids and Structures* 45(7-8) (2008) 1845-1875.
- [132] W.-Y. Jang, S. Kyriakides, On the crushing of aluminum open-cell foams: Part II analysis, *International Journal of Solids and Structures* 46(3-4) (2009) 635-650.
- [133] Y. Sun, R. Burgueño, W. Wang, I. Lee, Modeling and simulation of the quasi-static compressive behavior of Al/Cu hybrid open-cell foams, *International Journal of Solids and Structures* 54 (2015) 135-146.
- [134] P. Fanelli, A. Evangelisti, P. Salvini, F. Vivio, Modelling and characterization of structural behaviour of Al open-cell foams, *Materials & Design* 114 (2017) 167-175.
- [135] S. Gómez, M.D. Vlad, J. López, M. Navarro, E. Fernández, Characterization and three-dimensional reconstruction of synthetic bone model foams, *Materials Science and Engineering: C* 33(6) (2013) 3329-3335.
- [136] Y. Chen, R. Das, M. Battley, Finite element analysis of the compressive and shear responses of structural foams using computed tomography, *Composite Structures* 159 (2017) 784-799.
- [137] E.L. Boland, R. Shine, N. Kelly, C.A. Sweeney, P.E. McHugh, A review of material degradation modelling for the analysis and design of bioabsorbable stents, *Annals of biomedical engineering* 44(2) (2016) 341-356.
- [138] D. Gastaldi, V. Sassi, L. Petrini, M. Vedani, S. Trasatti, F. Migliavacca, Continuum damage model for bioresorbable magnesium alloy devices—Application to coronary stents, *Journal of the mechanical behavior of biomedical materials* 4(3) (2011) 352-365.
- [139] I.O.f. Standardization, ISO 13314:2011 (E), Mechanical testing of metals _ Ductility testing _ Compression test for porous and cellular metals, Switzerland, 2011.
- [140] F.P. Beer, E.R.J. Johnston, J.T. DeWolf, D.F. Mazurek, *Mechanics of Materials*, 6 ed., McGraw-Hill 2012.
- [141] A. Paul, U. Ramamurty, Strain rate sensitivity of a closed-cell aluminum foam, *Materials Science and Engineering a-Structural Materials Properties Microstructure and Processing* 281(1-2) (2000) 1-7.
- [142] OriginLab, Nonparametric Tests. https://www.originlab.com/index.aspx?go=Products/Origin/Statistics#Nonparametric_Tests_PRO.
- [143] P. Schuler, S.F. Fischer, A. Buhrig-Polaczek, C. Fleck, Deformation and failure behaviour of open cell Al foams under quasistatic and impact loading, *Materials Science and Engineering a-Structural Materials Properties Microstructure and Processing* 587 (2013) 250-261.
- [144] A.C. Kaya, C. Fleck, Deformation behavior of open-cell stainless steel foams, *Materials Science and Engineering a-Structural Materials Properties Microstructure and Processing* 615 (2014) 447-456.
- [145] E. Amsterdam, J.H.B. de Vries, J.T.M. De Hosson, P.R. Onck, The influence of strain-induced damage on the mechanical response of open-cell aluminum foam, *Acta Materialia* 56(3) (2008) 609-618.
- [146] T.G. Nieh, K. Higashi, J. Wadsworth, Effect of cell morphology on the compressive properties of open-cell aluminum foams, *Materials Science and Engineering a-Structural Materials Properties Microstructure and Processing* 283(1-2) (2000) 105-110.

- [147] L.J. Xiao, W.D. Song, C. Wang, H.P. Liu, H.P. Tang, J.Z. Wang, Mechanical behavior of open-cell rhombic dodecahedron Ti-6Al-4V lattice structure, *Materials Science and Engineering a-Structural Materials Properties Microstructure and Processing* 640 (2015) 375-384.
- [148] Y.T. Jian, Y. Yang, T. Tian, C. Stanford, X.P. Zhang, K. Zhao, Effect of Pore Size and Porosity on the Biomechanical Properties and Cytocompatibility of Porous NiTi Alloys, *Plos One* 10(6) (2015) 10.
- [149] B. Jiang, Z.J. Wang, N.Q. Zhao, Effect of pore size and relative density on the mechanical properties of open cell aluminum foams, *Scripta Materialia* 56(2) (2007) 169-172.
- [150] J.L. Xu, L.Z. Bao, A.H. Liu, X.F. Jin, J.M. Luo, Z.C. Zhong, Y.F. Zheng, Effect of pore sizes on the microstructure and properties of the biomedical porous NiTi alloys prepared by microwave sintering, *Journal of Alloys and Compounds* 645 (2015) 137-142.
- [151] B.V. Krishna, S. Bose, A. Bandyopadhyay, Strength of open-cell 6101 aluminum foams under free and constrained compression, *Materials Science and Engineering a-Structural Materials Properties Microstructure and Processing* 452 (2007) 178-188.
- [152] H. Fan, D. Fang, Enhancement of mechanical properties of hollow-strut foams: analysis, *Materials & Design* 30(5) (2009) 1659-1666.
- [153] E. Andrews, Open-cell foams with hollow struts: mechanical property enhancements, *Materials Letters* 60(5) (2006) 618-620.
- [154] T. Daxner, Deformation Mechanisms and Yielding in Cellular Metals, in: H. Altenbach, A. Ochsner (Eds.), *Plasticity of Pressure-Sensitive Materials*, Springer-Verlag Berlin Heidelberg 2014, pp. 165-166.
- [155] A. Mirabolghasemi, A. Akbarzadeh, D. Rodrigue, D. Therriault, Thermal conductivity of architected cellular metamaterials, *Acta Materialia* 174 (2019) 61-80.
- [156] M. Eynbeygui, J. Arghavani, A. Akbarzadeh, R. Naghdabadi, Anisotropic elastic-plastic behavior of architected pyramidal lattice materials, *Acta Materialia* 183 (2020) 118-136.
- [157] M.D. Abràmoff, P.J. Magalhães, S.J. Ram, Image processing with ImageJ, *Biophotonics international* 11(7) (2004) 36-42.
- [158] M. Doube, M.M. Kłosowski, I. Arganda-Carreras, F.P. Cordelières, R.P. Dougherty, J.S. Jackson, B. Schmid, J.R. Hutchinson, S.J. Shefelbine, BoneJ: free and extensible bone image analysis in ImageJ, *Bone* 47(6) (2010) 1076-1079.
- [159] T. Ridler, S. Calvard, Picture thresholding using an iterative selection method, *IEEE transactions on Systems, Man and Cybernetics* 8(8) (1978) 630-632.
- [160] R. Dougherty, K.-H. Kunzelmann, Computing local thickness of 3D structures with ImageJ, *Microscopy and Microanalysis* 13(S02) (2007) 1678-1679.
- [161] W.-Y. Jang, S. Kyriakides, A.M. Kraynik, On the compressive strength of open-cell metal foams with Kelvin and random cell structures, *International Journal of Solids and Structures* 47(21) (2010) 2872-2883.
- [162] S.A. Kaoua, S. Boutaleb, D. Dahmoun, M. Azzaz, Numerical modelling of open-cell metal foam with Kelvin cell, *Computational and Applied Mathematics* 35(3) (2016) 977-985.
- [163] H.E. Cleaves, J. Hiegel, Properties of high-purity iron, *J. Res. Natl. Bur. Standards* 28(643) (1942) 1471.
- [164] M. Sulong, M. Taherishargh, I. Belova, G. Murch, T. Fiedler, On the mechanical anisotropy of the compressive properties of aluminium perlite syntactic foam, *Computational Materials Science* 109 (2015) 258-265.

- [165] Y. Woo, S.-H. Kim, Sensitivity analysis of plating conditions on mechanical properties of thin film for MEMS applications, *Journal of mechanical science and technology* 25(4) (2011) 1017.
- [166] C. San Marchi, A. Mortensen, Deformation of open-cell aluminum foam, *Acta Materialia* 49(19) (2001) 3959-3969.
- [167] A. Groysman, *Corrosion for everybody*, Springer Science & Business Media 2009.